SINTEF

OC2018 F-073-WP1 - Restricted

Report

LFCS
Large Floating Coastal Structures

LFCS Review report - Environmental conditions

Wind, wave and current in coastal areas

Author(s)
Dag Fergestad, Ole Økland (introduction/geography/standards)
Christos Stefanakos, Carl Trygve Stansberg (waves)
Eloïse Croonenborghs, Lene Eliassen (wind)
Grim Eidnes (currents)

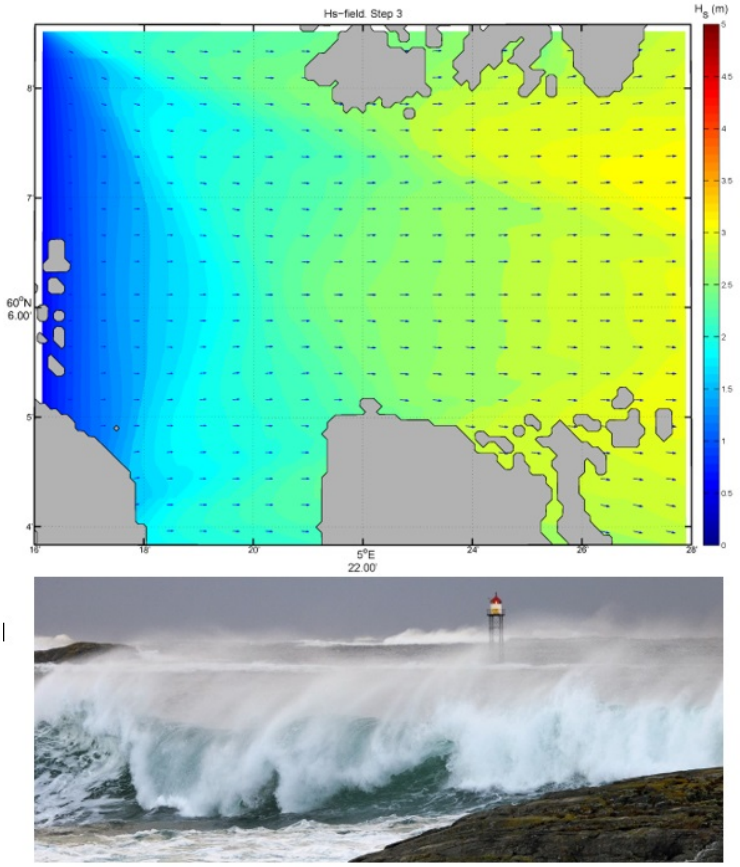

SINTEF Ocean
New resources and marine modelling
14th November 2018

SINTEF Ocean
SINTEF Ocean

Address:
Postboks 4762 Torgard
7465 Trondheim
NORWAY

www.sintef.no

KEYWORDS:
Environmental conditions
Coastal
Wind
Wave
Current

Report

LFCS Review report - Environmental conditions

Wind, wave and current in coastal areas

VERSION	DATE
1.0	14th November 2018

AUTHOR(S)
Dag Fergestad, Ole Økland (introduction/geography/standards)
Christos Stefanakos, Carl Trygve Stansberg (waves)
Eloïse Croonenborghs, Lene Eliassen (wind)
Grim Eidnes (currents)

CLIENT(S)	CLIENT'S REFERENCE
KPN-project LFCS Industry partners and Norwegian Research Council (NRC)	

PROJECT	NUMBER OF PAGES AND ATTACHMENTS
302001772	114

ABSTRACT
A review is performed on the description of environmental conditions in Norwegian coastal areas in relation to Large Floating Coastal Structures and the planning of long floating bridges across fjords. First, an outline of some geographic location of possible crossing sites in various fjords is documented along with some existing structures where work is ongoing for obtaining additional information. Then, a survey about the methods for studying wave, wind and current conditions in such environments is given. Finally, some gaps in existing methodologies are identified and recommendations are given.

The work is performed as a part of the NRC and Industry-sponsored KPN-project "Design and Verification of Large Floating Coastal Structures – LFCS".

PREPARED BY	SIGNATURE
Dag Fergestad	

CHECKED BY	SIGNATURE
Halvor Lie	

APPROVED BY	SIGNATURE
Vegard Aksnes	

REPORT NUMBER	ISBN
OC2018 F-073-WP1	

CLASSIFICATION	CLASSIFICATION THIS PAGE
Restricted	Restricted

Document History

VERSION	DATE	VERSION DESCRIPTION
1.0	14th November 2018	Final version of WP1 report, after having taken into account all the comments of the clients

SINTEF

Contents

1 Introduction and Summary

1.1 General

The KPN project ”Design and verification of Large Floating Coastal Structures” (LFCS) started with a kick-of Nov.30, 2017, with a planned duration to summer of 2021. The project was established by SINTEF Ocean and NTNU with the support of the Norwegian Research Council, the Norwegian Public Road Administration, Hydro ASA, Multiconsult AS, SWECO AS, and LMG Marin AS

Compared with well-established methods in ocean engineering, the following critical issues are initially identified for the analysis of large floating coastal structures,

- varying bathymetry and inhomogeneous environmental conditions over the extension of the structure
- inhomogeneous environmental loads over the structure,
- hydroelasticity of large floating coastal structures under inhomogeneous conditions,
- mooring and station-keeping of large flexible floating structures,
- modelling of hydroelastic effects in combinations with articulated/elastic interconnections between structural parts.

One objective of the present project is to improve the understanding of each of these separate topics, and then to provide input to a consistent procedure for design and verification of large floating coastal structures. The project is then organized in work packages according to the identified topics above:

- WP1 - Environmental description
- WP2 - Environmental loads
- WP3 - Structural response
- WP4 - Mooring and positioning
- WP5 - Model testing

In addition, the LFCS administrative tasks have been organized in a work package WP0.

Review phase:

The first phase of the project is devoted to a review of work already performed for relevant existing structures, for conceptual studies performed for potential crossings as well as additional work on measurements, modelling, simulations related to coastal areas which in all comprises the state of the art. This also included a 2-day workshop on March 7-8 with emphasis on environmental description, modelling and loads, and structural response based on presentations from the LFCS industry partners and specially invited external presenters.

This document describes and summarizes the review work performed for Work Package 1 (WP1) -– Environmental description, identifying gaps and uncertainties recommended for further study.

1.2 Main objectives of the WP1 -– Environmental description

- Review methods for rational description of inhomogeneous environmental conditions for coastal areas: Computer codes (functionality and limitations) and data/measurements for relevant locations.
- Establish input for case studies and model tests on large floating coastal structures, such as floating bridges.
- Assess available methods and information: Important paramenters for selected concepts or case studies and quantify uncertainty
- Give recommendations regarding modelling of environmental conditions for concepts studied.

1.3 Summary of gaps and recommendations

1.3.1 Wave description

It is not possible to give a specific range of values for metocean conditions, since each fjord is situated in a different location with a different exposure to the open ocean conditions, coastline and bathymetry of different complexity etc. However, what is common practice in all situations is the procedure that should be followed.

First, long-term offshore wind and wave conditions near the fjord should be analysed from a reliable source of data (e.g., model or measured data). Then, a detailed bathymetry of the area should be derived and be combined with the offshore conditions to transfer them from offshore to nearshore using a neasrshore wave model such SWAN or MIKE21-SW.

The quality of input (both offshore conditions and coastline/bathymetry) is very important and determines to a large extent the quality of the output. Another important factor is the definition of the appropriate computational domain, as well as the nesting scheme to be applied as we approach the target points.

In this way, one can obtain long-term time series of directional wave spectra at various locations in the area of interest (e.g., along a bridge crossing). This kind of data is of fundamental importance for the study of the nearshore wave climate. It can be served to obtain a number of useful statistics including (but not limited to) extreme values, joint probability densities, directional fields of mean values, seasonal variation of main parameters, wind and wave roses, probability densities of spectra etc.

In addition, typical (or most frequently occurred) forms of numerical spectra can be directly used as input to response analysis models without the need of assuming *a priori* a specific analytic form for them.

There is an increasing literature concerning the coupling of wave models with current modelling to improve predictions in both of them; see, e.g., (Chen et al., 2018, and references cited therein). However, all cases examined in the literature concern very shallow water ($<$50 m), where other phenomena are present and which is certainly not the case in the Norwegian fjords.

Further, one can identify some gaps in the existing methodologies used:

1. There are no validations of results obtained by numerical models (SWAN, MIKE21-SW, STWAVE etc) with extensive *in situ* measurements and systematic runs of CFD codes for the topography of the Norwegian fjords
2. Phase averaged (by default) models do not give any information about the phase
3. Inhomogeneous wave conditions can partially studied by the obtained spectra at various locations. Additional runs of CFD codes may further validate this

1.3.2 Wind description

The traditional way of describing the wind field for structural engineering purposes is limited by the flow assumptions of stationarity and homogeneity.

Long term statistics Long term statistics, which are used for obtaining wind roses and identifying extreme winds corresponding to different return periods for each wind sector, can't be obtained from measurements which are only performed for short periods of time since it is not possible to assess whether the observed conditions represent e.g. 10, 100 or 10 000-years conditions. Engineering projects does not have time to wait for records over a sufficiently long period, and have to rely on simulations. In flat terrain (offshore or onshore), hindcast analysis such as NORA10 can be used to obtain long-term statistics. However, the spatial resolution used in the NORA10 analysis does not provide accurate flow description in complex terrain such as coastal Norway. It is therefore recommended to perform a downscaling of a mesoscale hindcast to a microscale level for each region of interest.

(Johansen, 2016) - A related, but different riddle concerns what will be the normal and extreme weather 100 years ahead. This reflects not only stochastic uncertainty due to natural variations, but also epistemic uncertainty due lack of knowledge related to climate change. [...] This makes robustness and flexibility critical for the maturity of the concepts in a 100-year life cycle perspective.

Non-homogeneity The models presented in Section 5.2 for short-term statistical description of the wind field have been developed under the assumptions of stationarity and homogeneous flow. In Norwegian fjords, due to the steep topography and abrupt roughness changes, the flow cannot be considered as homogeneous and those models might no longer be appropriate. Due to the strong influence of the local topography unique to each site of interest, it is challenging to derive a generalized model to describe wind turbulence. As pointed out by (Wang et al., 2017a), it is therefore required to find an alternative way to describe the wind field in the region of interest. As a generalized approach to characterizing the wind flow, it is suggested perform the following analyze for each wind sector and for each wind speed:

- Extract the mean wind velocity distribution from a corresponding event in the hindcast analysis
- Extract the short term statistics of wind from the wind measurements at an occurrence of a wind event as close as possible to the target wind condition. These short term statistics should be extracted at as many locations as possible, at the height of interest for engineering purposes. If another height must be used, the local mean wind velocity profile predicted in the hindcast should be used for extrapolation at the height of interest.

Due to the non-homogeneity of the surrounding terrain, it can't be assumed that the wind description will be identical from one wind sector to another and the wind characterization process must be performed for each wind sector and all relevant mean wind speeds (Cheynet et al., 2016a).

Low frequency content in wind spectra Since the recording of a wind event must be stationary in order to extract its short term statistics without introducing error, samples of a duration of 2 to 3 hours are required to evaluate the spectrum in the low frequency range. However, since the atmosphere is permanently evolving, it is rare to observe so long stationary periods. According to (DNV, 2007), since it cannot always be relied upon that the stochastic wind speed process remains stationary over time intervals of the order of 2 to 3 hours, the wind spectrum approach cannot necessarily be utilized for wind loads on structures, whose natural frequencies are near the limiting frequency of 1/2400 Hz of the wind spectrum.

Wind spectra for storm conditions Empirical spectra are generally based on measurements performed in non-storm conditions due limited amount of data available above certain wind speeds. (Andersen and Løvseth, 2006; Toriumi et al., 2000) have shown the variability of the wind spectrum to wind speed. It might therefore not be appropriate to use model spectra for wind speeds above the ones on which they are based.

Wave effect on wind field It is well known that waves results from wind, but little is still known about the impact that waves have on wind turbulence. Waves behave as dynamic roughness. They can have different shapes and travel in various directions relative to the wind. The relations between wave parameters and wind turbulence have been only studied by a few and it is still unclear up to which heights are the wave effects perceived in the wind field. It is recommended to deepen the literature study in this direction and to perform additional studies to document the wave effect on the wind field.

(ApS, 2018)

Turbulence generators

Non-homogeneity In their current implementation, non-uniform wind statistics (horizontal wind shear, non-uniform turbulence intensity, vertical dependence of the wind spectra) cannot be given as input in turbulence generators. It is recommended to implement a turbulence generator that can take as input non-uniform wind statistics as an interpolated function between control points.

Grid In their current implementation, the grids used in turbulence generators are composed of points that are uniformly distributed in space in an orthogonal fashion. The time dimension of the box is also proportional to the natural frequency of the structure. When studying large structures with long natural period, the resulting grid becomes very large resulting in heavy computational needs. It is recommended to implement an option for non-uniform grids in turbulence generators in order to reduce the amount of points in locations where they are not relevant as well as a possibility to map the points to the structure, allowing then to have points that follow the curvature of the structure of interest.

1.3.3 Current description

Current measurements There has been a considerable progress when it comes to ocean current measurements over the last decades. When the acoustic current profiling technique was introduced in the 1980s, a new era of current data acquisition arose. Instead of counting the number of revolutions of a rotor and recording the position of a vane, the field oceanographer had to decide on various setup codes as

- burst mode vs. spread mode
- number of pings
- depth cell size
- number of cells
- blanking distance

and other tracking and system configurations. This has in turn lead to some challenges when it comes to the convention of how to measure ocean currents: as a vectorial average over 10 minutes. It may be difficulty comparing one current velocity with another if they are measured differently.

It is hardly desirable and probably neither necessary nor possible to set up standards for a recommended configuration, the applications and variations are probably too large. But the desire for the highest possible accuracy and quality should be guiding the choices to be made. It is therefore recommended that simple and common guidelines should be established to ensure a common basis for best practice of how ocean current measurements should be performed.

Extreme value analyses Tidal currents are periodic processes where extreme values have an upper limit depending on the earth's position relative to the moon and the sun. When the amplitude and phase of the individual tidal components are determined (by harmonic analysis), the tidal current (both speed and direction) can be determined for any time. The tidal current is deterministic. To analyse tidal currents from statistical distribution and extrapolation is methodically incorrect.

When the tidal current distribution is removed from the time series, the residual current remains. To calculate extreme values of currents, statistical extrapolation of the residual current data is used. This is done by fitting a given distribution (as Weibull, Gumbel or others) to the measured data, and then extrapolating this distribution to find expected extreme values for return periods as 10, 50 and 100 years. The data used should be independent and (ideally) represent one event with a given duration. An often-used method is to select the highest value over a given period - typical one, two or three days - and define these maxima as the new data basis. The duration of the event is then uniquely decided, and there are good reasons to believe that the data are independent.

The accuracy of an extreme value analyses highly depends on how good the chosen distribution fits the data. In those cases where the fit to data is not good (in particular for the highest speed values), a truncated distribution should be applied to try to improve the fit. The truncation cut-off value should be determined individually for each data set.

When the extreme residual currents are determined, the result must be combined with the tidal current values. So, what is the combined probability that an extreme residual current created by strong winds and low pressure occurs at the same time as a spring tide current, creating a storm surge? To be on the safe side, the two extreme values are often summed up. However, since the values are independent, this gives a strongly conservative estimate. It can be shown that the combined probability, P, for exceeding a particular z-value, $z = a$, is given by

$$P(a) \approx \sum_{X_{\min}}^{X_{\max}} \left[1 - H(a - x)\right] \, g(x) \, \Delta x, \tag{1}$$

where H describes the residual current distribution (e.g. the Weibull-distribution), and g is the probability distribution for the tidal current given by the probability of exceeding a particular tidal current speed.

It is recommended that some guidelines are established along these lines to ensure a common basis for best practice of how extreme ocean current value analyses are to be performed.

2 Overview of the fjords topography

This section provides some background information on some existing crossings in coastal Norway and some selected crossings along the E39 coastal route, all representative for the Norwegian coastal climate, see Figure 1. The information pertains to localization, topography, crossing details and structure, as well as environmental measurement campaigns (if available).

The following crossings are located along the E39 and subject to study for the ferry-free E39:

- Bjørnafjord
- Sognefjord

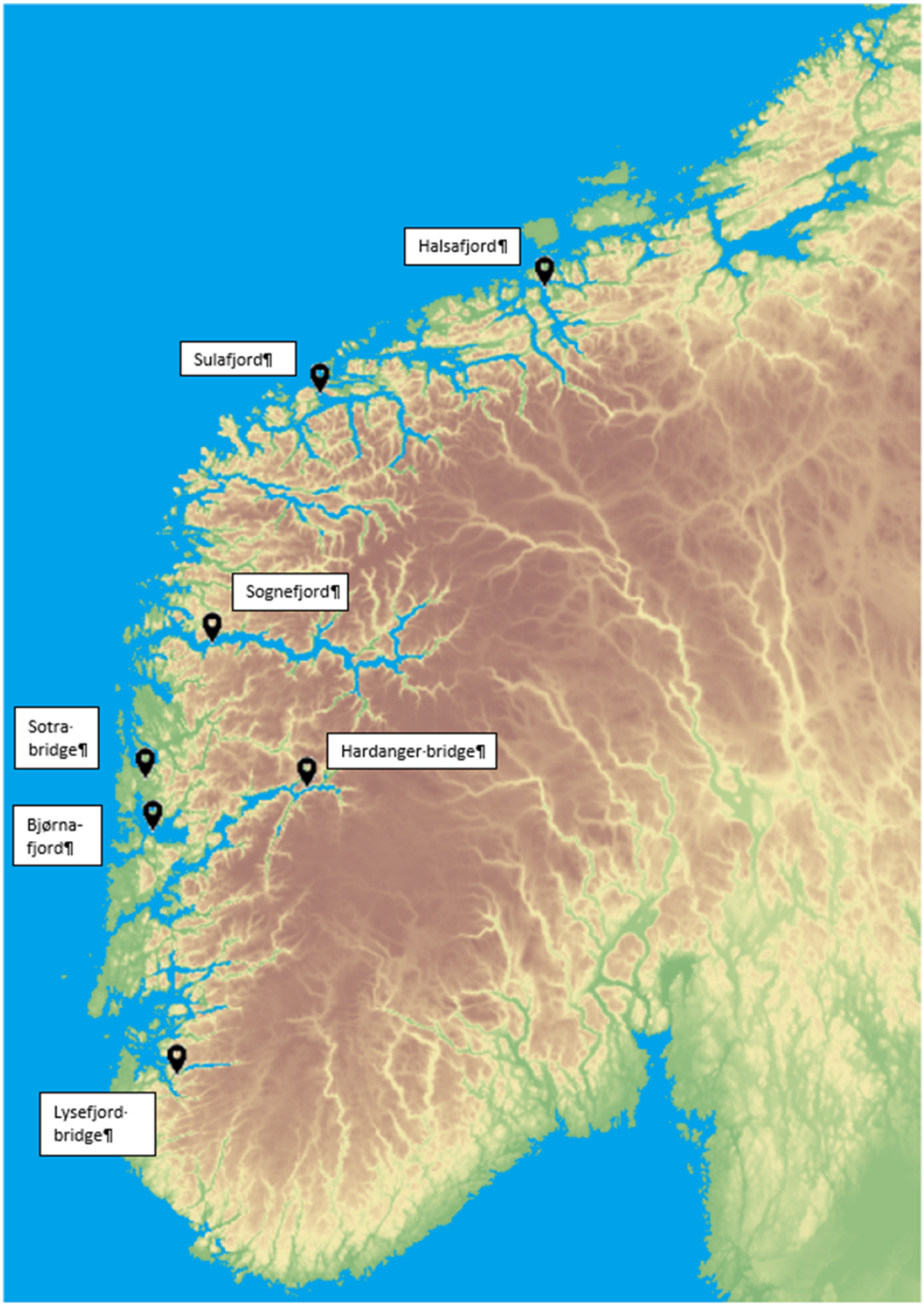

Figure 1: Topography of Southern Norway and relevant fjord locations in this report

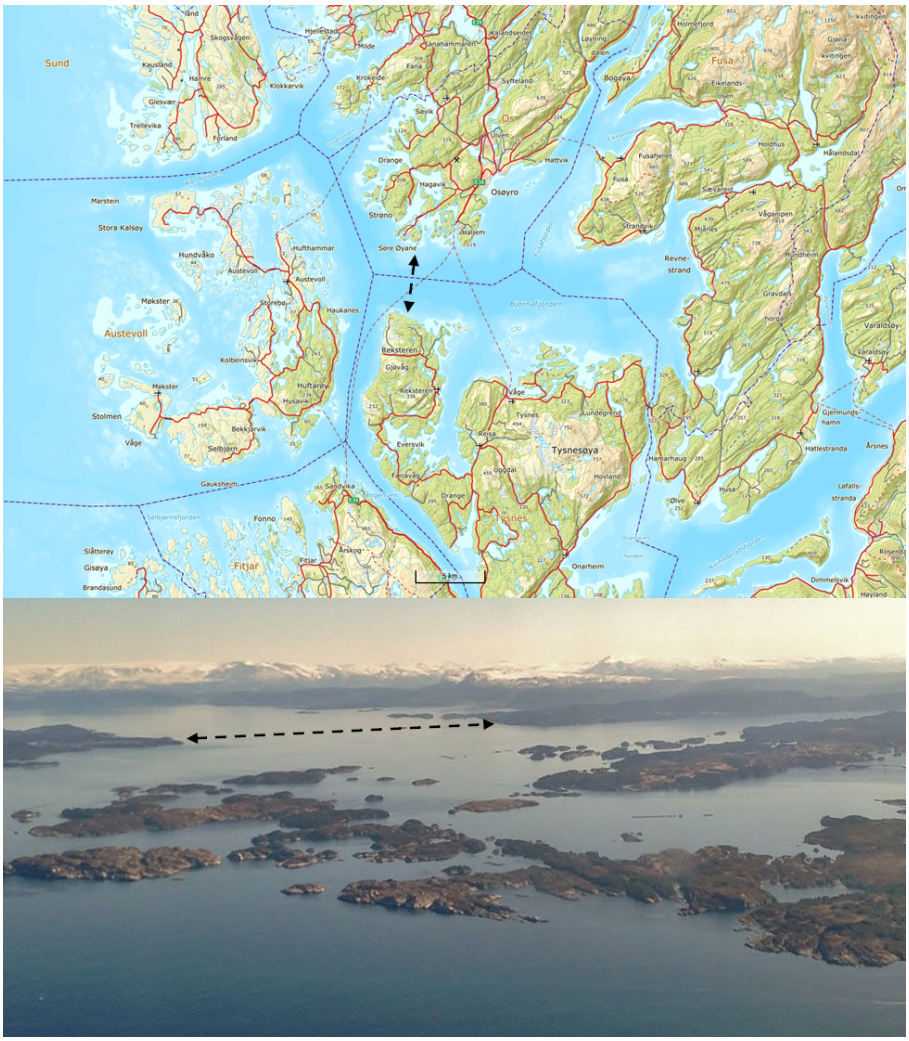

Figure 2: An overview of the Bjørnafjord crossing

- Sulafjord
- Halsafjord

The following crossings are all existing suspension bridges and are not located along the E39:

- Lysefjord bridge
- Hardangerfjord bridge
- Sotra bridge

The latter represents structures and locations where significant wind studies and measurements have been performed, some still ongoing.

2.1 Bjørnafjord

Bjørnafjord is a wide fjord located about 30 km South of Bergen. At the location of the planned fjord crossing, the fjord is 5 km wide and 550 m deep. The West side of the Bjørnafjord is relatively flat and scattered with small islands, see Figure 2.

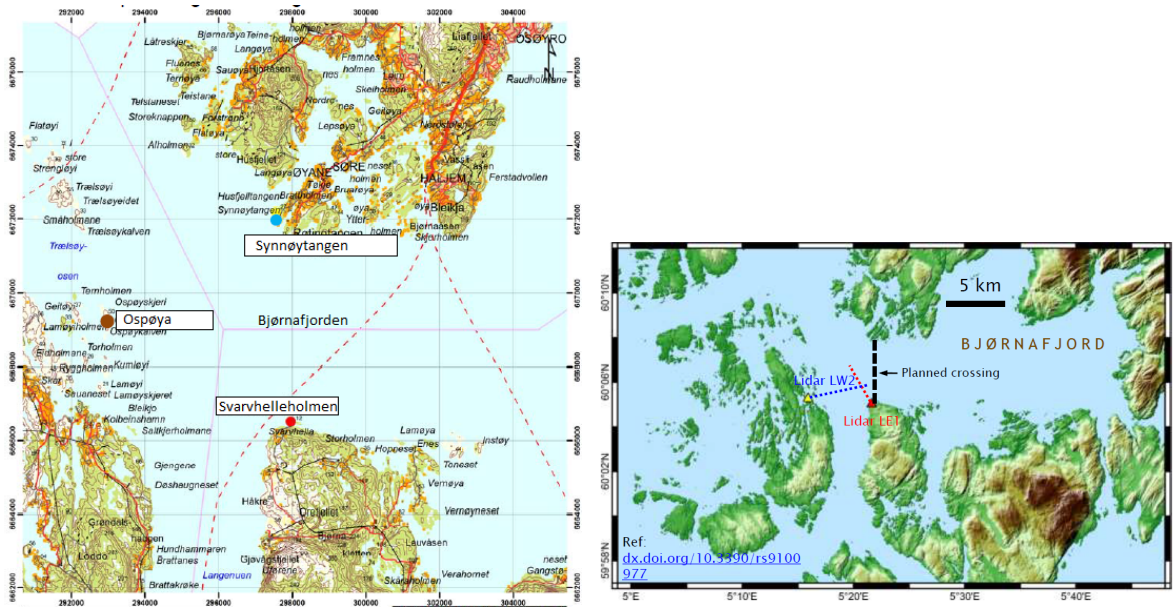

(a) Met masts locations (Harstveit and Ágústsson, 2017) (b) Lidars locations and orientations (Cheynet et al., 2017b)

Figure 3: An overview of the wind measurements devices in Bjørnafjorden

The long-term wind monitoring system includes several met masts located at 3(a). Two of the met masts are located 260 m apart at Ospøya. Each mast is 50 m high and is equipped with up to 3 anemometers. The measurements were performed by Kjeller Vindteknikk, starting in December 2015 at Ospøya and in February/March 2015 for the other locations, and ended 28.02.2017.

- Synnøytangen(26m a.s.l.)
- Svarvhelleholmen (5m a.s.l)
- Landrøypynten(21m a.s.l)
- Nesøya (12m a.s.l.)
- Ospøya1 (23m a.s.l)
- Ospøya2 (34m a.s.l.)

In May and June 2016, three long-range Doppler wind lidars were deployed in the Bjørnafjord area. Because of the low availability of data on one of the lidars, only data measured using LW2 and LE were further analyzed in (Cheynet et al., 2017b). The lidar LW2 is located on the west side of the fjord. The lidar LE is installed some kilometres to the South-East of LW2. The scanning head of the lidars LW2 is oriented toward the East, whereas the scanning head of LE is oriented toward the North-West (Figure 3(b)). The intersection of the laser beams is located 25 m above sea level.

2.2 Lysefjord

Lysefjord is a 40 km long fjord, which is 2 km wide at the most and 600 m narrow at the bridge location. At its inlet, Lysefjord connects to Høgsfjord, a wider fjord orientated from North-West to South-East.

The Lysefjord suspension bridge has a main span of 446 m with an elevation of 55 m above the sea level at mid-span. It is oriented from North-West to South-East and is surrounded by steep hills with slopes ranging from 30^o to 45^o and a maximum altitude of 350 m to the North and 600 m to the South.

The long-term wind monitoring system includes seven ultrasonic anemometers mounted on the west side of Lysefjord Bridge. The anemometers located on hangers 10, 16, 18, 20 and 24 were installed on November 2013

Figure 4: Map of Lysefjord area (top) and photo of Lysefjord bridge (bottom)

(a) Wave buoys and Hindcast (Wang et al., 2018b)

(b) Wave buoys and met masts (MET workshop)

Figure 5: An overview of the wind measurements devices in Sulafjord (top) and photo of Sulafjord (bottom)

at 6 m above the bridge deck. Two additional anemometers were installed in June 2014 on hanger 8 at 6 m and 10 m above the bridge deck. The seven anemometers are distributed over a distance of 192 m.

2.3 Sulafjorden

The Sulafjord is located between the islands of Hareidlandet and Sula in Møre and Romsdal County. There are mountains on both sides of the fjord, with altitudes up to 700 m. At the northwest side of the fjord, the Godøya island, with an altitude of 400 m, is sheltering the fjord to some extent from the open ocean. To the southeast, there is a mountainous area with altitudes above 1000 m.

Four wave buoys equipped with anemometers were deployed in October 2016 at the locations indicated in Figure 5. Buoy D is at the inlet of the fjord, and buoy A further in the fjord. Buoys B and C are close to the intended locations of two floating towers. Data from Buoy C is not available. The wind data consist of mean wind direction and mean wind velocity at 4.1 m above the sea level.

Two tall met-masts with sonic wind measurements in three heights, around 100m, 70m and 50m (red) are deployed on the coast of Hareilandet. Data are available on `http://thredds.met.no/thredds/obs.html`.

Figure 6: An overview of the Halsafjord crossing

2.4 Halsafjorden

Halsafjord is located between the municipalities of Halsa and Tingvoll in Møre and Romsdal county, on the east side of the city of Kristiansund The fjord branches south off the Vinjefjorden and stretches about 15 kilometres until it becomes the Trongfjorden.

The European route E39 highway crosses the fjord by a car ferry from Kanestraum in Tingvoll to Halsanaustan in Halsa. Possible bridge sites are located north of the ferry crossing where the fjord narrows to about 2-3 km, with a depth of about 500m. A crossing at Halsaneset on the west side (Tingvoll) to Orneset (Åkvika, Halsa) on the east side of the fjord is a likely site.

Several bridge options are discussed for this crossing; one span suspension bridge, two span suspension bridge with a floating tower, floating bridge and submerged floating bridge. Measurements (ground measurements, wind, current and waves) are ongoing.

2.5 Sognefjorden

Sognefjorden is Norway's longest fjord, about 200km of length and west to east oriented. The E39 ferry crossing of the Sognefjord is located between the communities of Lavik (Høyanger municipality, north side) and Oppedal (Gulen municipality, south side), about 1/5 into the fjord from its entrance to the ocean.

At the likely bridge site, the fjord is almost 4km wide (about 3700m) and about 1300m deep. There are limited environmental data available. Several bridge concepts have been proposed in feasibility studies, and all point out the challenges with this crossing.

Figure 7: Location of the Sognefjord crossing relative to the inlet from the ocean

Figure 8: An overview of the Sognefjord crossing

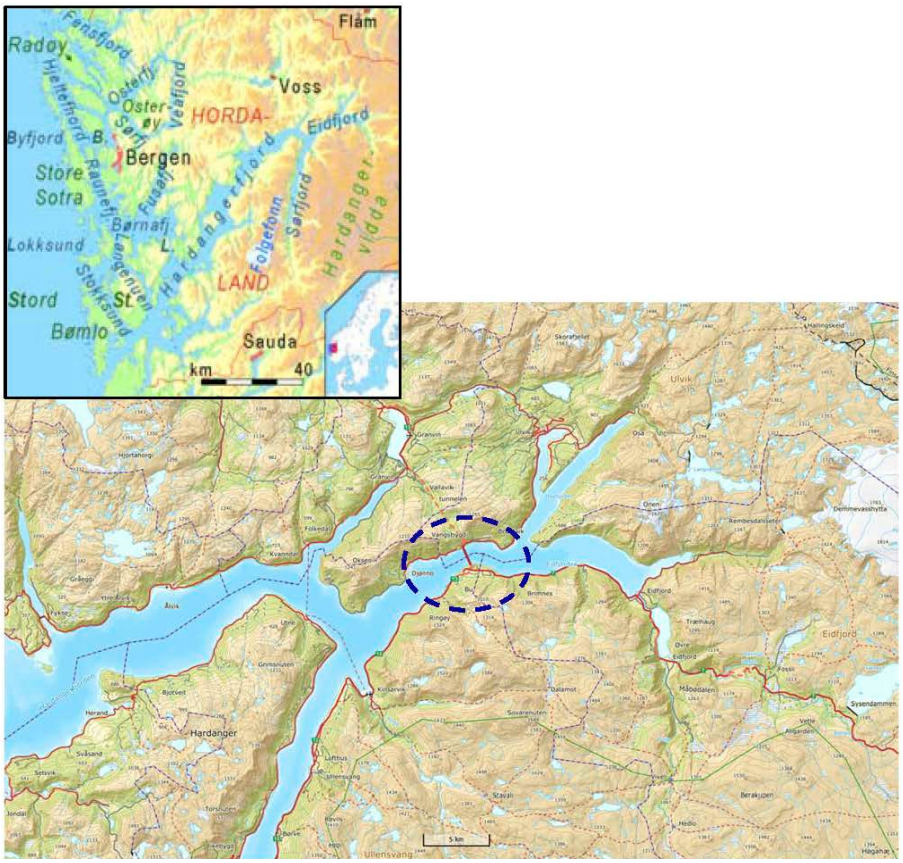

Figure 9: Location of the Hardangerfjord crossing

2.6 Hardangerfjorden

The Hardangerfjorden bridge site is in the innermost area of the Hardangerfjord (the Eidfjord branch), the second longest fjord in Norway, about 180km from the Atlantic Ocean. At the bridge site the fjord has a predominantly west to east direction. A suspension bridge was built between the municipalities of Ullensvang (south side) and Ulvik (north side) replacing the ferry connections between Bruravik and Brimnes. The bridge was opened in 2013 with a main span of 1310m, a deck height of 55m and a width of 20m (2 lanes and a pedestrian lane).

Wind measurements were performed on land at the bridge ends during the planning phases as well as on/along the bridge after construction. Studies have been made on the environmental wind loading and the bridge response.

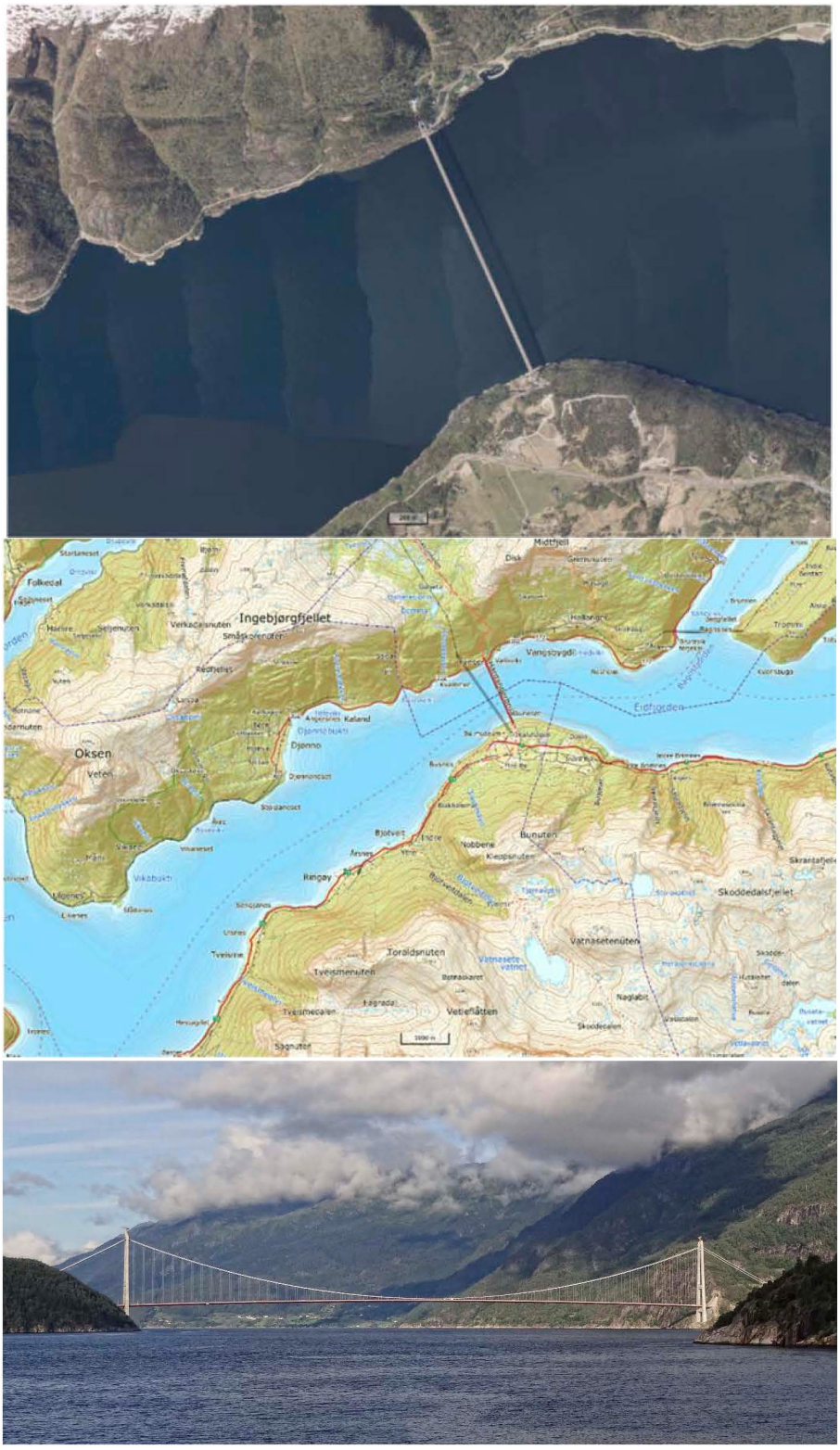

Figure 10: An overview of the Hardangerfjord crossing

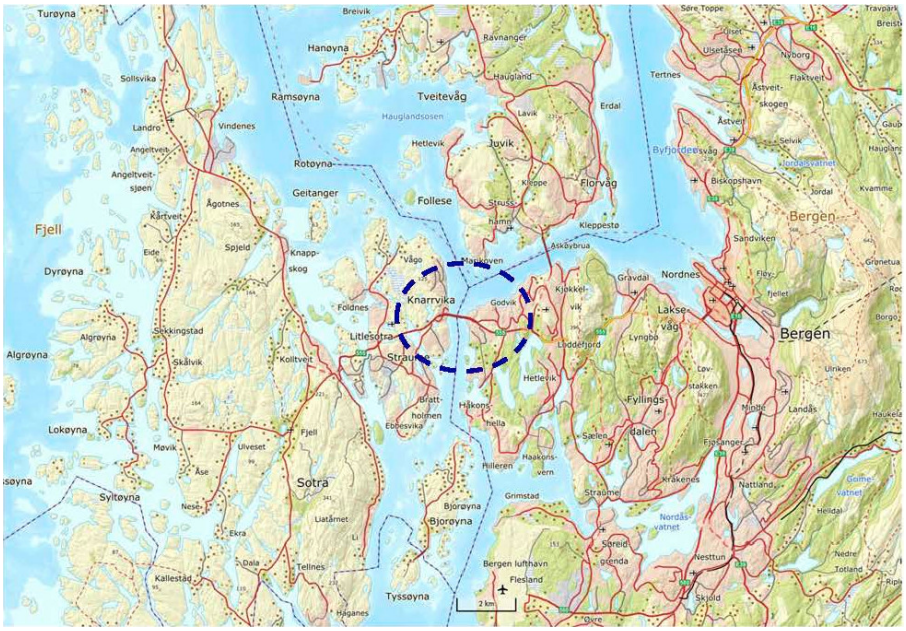

Figure 11: Location of the Sotra bridge

2.7 Sotra bridge

The Sotra bridge is a suspension bridge west of the city of Bergen, crossing Knarrviksundet. The bridge has a main span of 468m, a clearance of 50m and carries two road lanes and two narrow pedestrian paths. The bridge was opened in 1971 and is not a part of the E39.

The interest for the bridge for this report is the coastal location and the wind studies performed for this bridge prior to and after the construction.

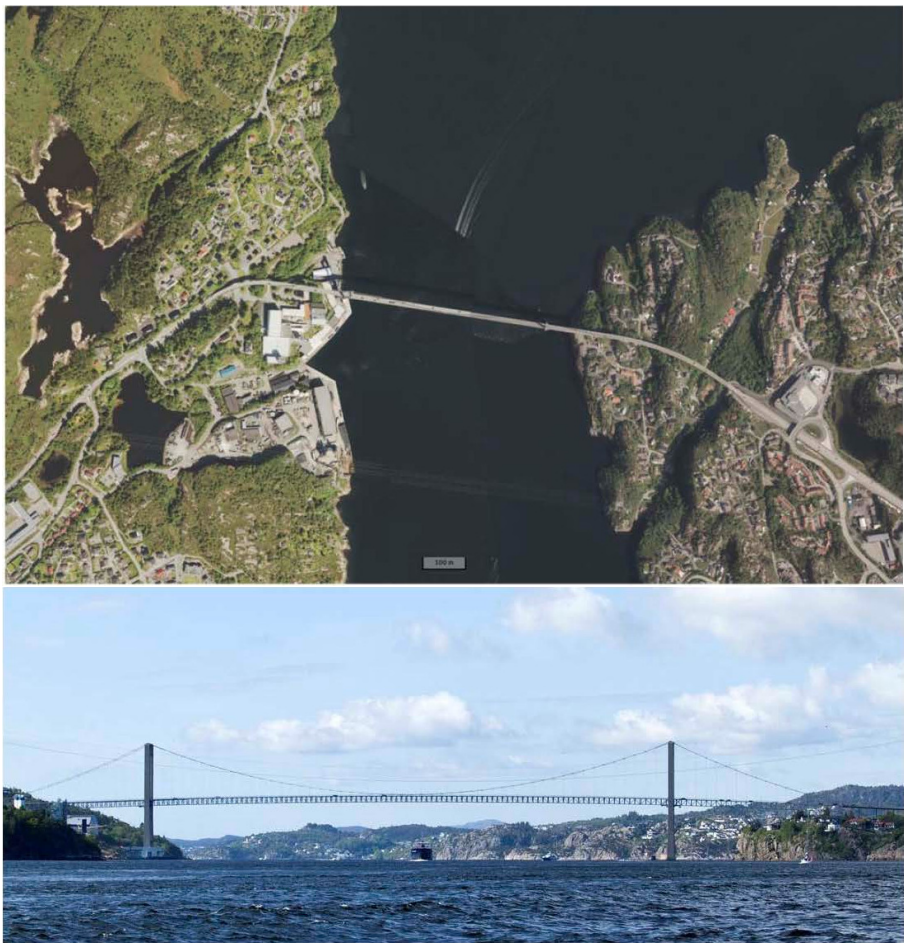

Figure 12: An overview of the Sotra bridge crossing

3 Standards

The EN Eurocodes are a series of 10 European Standards, EN1990 - EN1999, providing a common approach for the design of buildings and other civil engineering works and construction products. In EN1991, which describes actions on structures, Part 1-4 in entirely dedicated to wind actions. The EN Eurocodes are to be used in combination with the corresponding National Annex which lists country specific data and alternative methods to be used.

Håndbok N400 Bruprosjektering from Statensvegvesen sets requirements for the construction of bridges, ferries and other load-bearing structures in the public road network. It presupposes the use of Standard Norway's safety, load and material standards, ie the NS-EN series, also called Eurocodes.

The NORSOK standards are targeted to the Petroleum industry. Norwegian safety framework and climate conditions may require own standards, or additions and supplements to International Standards and European Standards. They have been developed to fulfill these needs. The NORSOK-N-003 document is dedicated to actions and action effects. It is applicable to all types of offshore structures used in the petroleum activities, including bottom-founded structures as well as floating structures, including substructures, topside structures, vessel hulls, foundations, mooring systems, risers and subsea facilities.

ISO 19901-1 gives general requirements for the determination and use of meteorological and oceanographic (metocean) conditions for the design, construction and operation of offshore structures of all types used in the petroleum and natural gas industries.

IEC 61400 is an International Standard published by the International Electrotechnical Commission regarding wind turbines. Part 1 of IEC 61400 outlines minimum design requirements for wind turbines and is not intended for use as a complete design specification or instruction manual. The standard is not intended to give requirements for wind turbines installed offshore, in particular for the support structure.

DNV Offshore Codes consist of a three level hierarchy of documents: Offshore Service Specifications, Offshore Standards, and Recommended Practices. Recommended Practices provide proven technology and sound engineering practice as well as guidance for the higher level Offshore Service Specifications and Offshore Standards. DNV-RP-C205 Environmental Conditions and Environmental Loads gives guidance for modelling, analysis and prediction of environmental conditions as well guidance for calculating environmental loads acting on structures. The loads are limited to those due to wind, wave and current.

NORSOK - For situations where the low-frequency excitation is of importance, the following one sided energy density spectrum of the longitudinal velocity fluctuations at a particular point in space is recommended, see Andersen and Løvseth (1992). The Harris wind spectrum may be considered when action effects in structures such as flare towers, which are sensitive to the high frequency excitation are to be calculated. Wind gusts have three-dimensional spatial scales related to their duration, e.g. 3 s gusts are coherent over shorter distances and therefore affect smaller structural elements than 15 s gust. Wind actions on different substructures are normally specified by a given averaging time for the wind speed and assuming full coherence over the entire substructure. Specific information about averaging time is given in 6.3.3 for static and in 6.3.4 for dynamic analysis.

4 Wave modelling in coastal area

Metocean data are of essential importance for hydrodynamic and structural response analysis of various coastal floating structures, such as the bridges to be built in the framework of the Norwegian “E39-ferry free” project. In this Chapter, relevant wave data sets will be investigated, and their applicability with respect to such kind of structures will be discussed.

Wave modelling methods and procedures have for many decades been developed for the ”established” maritime and offshore engineering activities in deep or almost deep water, and comprehensive and well documented recommendations and standards are available (DNV RP C-205; NORSOK, and similar sources). Some of these methods and standards can in principle also be adopted to the coastal applications, while there are clearly important issues that need separate treatment because of local (topography, bathymetry, wind, current) variations which makes this topic even more complex than that for offshore, although the waves themselves are certainly usually smaller. As such, and in parallel, wave modelling in coastal areas has also developed into a mature and quite advanced technology field, while so far mainly for fixed structures (civil engineering). So the task in the present WP1 will be to highlight and combine the available relevant technology for the present applications, identify and discuss possible gaps, and recommend actions

To accomplish this, it is also important to have in mind what are in fact the essential and critical needs for the actual hydrodynamic loads and structural response design of such long and flexible structures, in terms of wave parameters as well as types, details and amounts of data (re: WP2 and WP3). For example, the description of the spatial wave field then becomes more important. Very often, the available data can be limited in comparison to the desired data, and procedures and methods must take this into account. In particular, measured data in actual areas can be scarce, and data from numerical models are usually applied. Still, measurements are needed for validation and calibration.

In the following, an attempt will be made to present prevailing mechanisms of ocean waves nearshore and/or in enclosed areas such as the fjord formations in the Norwegian coasts. Then, a discussion will be given on the various relevant wave parameters and their availability from the various sources (models, measurements etc) both in time- and frequency-domain. Special emphasis will be put on the spatial and temporal coverage as well as the time needed to obtain them (as, e.g., the computational time).

4.1 Relevant physical wave phenomena in coastal area

The evolution of waves in deep water is dominated by wind and by propagation along straight lines (or great circles on the globe). When waves approach the coast, they are affected by the bottom, currents and, very close to shore, also by obstacles, such as headlands, breakwaters, etc., the effects of which usually dominate — surpassing the effects of the local wind — and the resulting wave propagation is no longer along straight lines. There is a wide range of literature on these topics; the textbook by Holthuijsen (Holthuijsen, 2007) gives a good insight into the main phenomena and on their numerical modelling. A brief summary of the physical processes is given in the following.

Figure 13 illustrates in a simple manner waves that propagate from the deep-water ocean to coastal areas, with the corresponding scales that are defined for the numerical modelling (see Section 4.2). When approaching the continental shelf from the ocean the initial effects of the bottom on the waves are not dramatic. In fact, they will hardly be noticeable until the waves reach a depth of less than about 100 m (or rather, when the depth is about one-quarter of the wave-length). The first effect is that the forward speed of the waves is reduced. This generally leads to a slight turning of the wave direction (refraction) and to a shortening of the wavelength (shoaling) which in turn may lead to a slight increase or decrease in wave height. Wind generation may be enhanced somewhat as the ratio of wind speed over wave speed increases when the waves slow down. However, this is generally masked by energy loss due to bottom friction. These effects will be relatively mild in the intermediate depths

of around 100 m but they will accumulate so that, if nothing else happens, they will become noticeable as the distances increase.

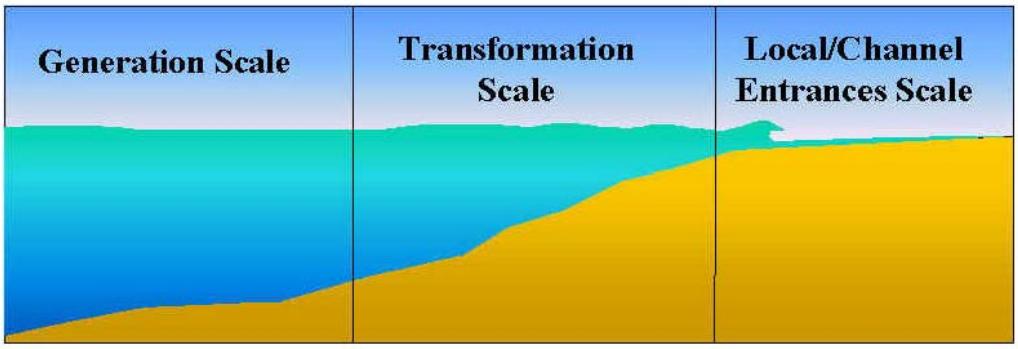

Figure 13: Wave propagation from ocean to coastal waters, with scales of wave processes indicated (Massey et al., 2011).

When the waves approach the coast from intermediate water depth and enter shallow water of 25 m or less, bottom effects are generally so strong (refraction and dissipation) that they dominate any wind generation. The above effects of refraction and shoaling will intensify and energy loss due to bottom friction will increase. All this suggests that the wave height tends to decrease but propagation effects may focus energy in certain regions, resulting in higher rather than lower waves. However, the same propagation effects may also defocus wave energy, resulting in lower waves. In short, the waves may vary considerably as they approach the coast.

In the near-shore zone, obstacles in the shape of headlands, small islands, rocks and reefs and break- waters are fairly common. These obviously interrupt the propagation of waves and sheltered areas are thus created. The sheltering is not perfect. Waves will penetrate such areas from the sides. This is due to the short-crestedness of the waves and also due to refraction which is generally strong in near-shore regions. When the sheltering is very effective (e.g. behind breakwaters) waves will also turn into these sheltered regions by radiation from the areas with higher waves (diffraction). When finally the waves reach the coast, all shallow water effects intensify further with the waves ending up in the surf zone or crashing against rocks or reefs.

Very often near the coast the currents become appreciable (more than 1 m/s, say). These currents may be generated by tides or by the discharge from rivers entering the sea. In these cases the currents may affect waves in roughly the same sense as the bottom (i.e. shoaling, refraction, diffraction, wave breaking). Indeed, waves themselves may generate currents and sea-level changes. This is due to the fact that the loss of energy from the waves creates a force on the ambient water mass, particularly in the breaker zone near a beach where long-shore currents and rip-currents may thus be generated.

As a natural result of all the above-mentioned processes (i.e. refraction from bathymetry and from currents, reflection from coastline, diffraction from obstacles, dissipation and other spectral changes), local spatial variations must be expected in the wave field across a fjord. However, these will certainly vary significantly from one fjord to another and must be addressed specific for each case.

4.2 Wave modelling / simulations

The most reliable source of information for the local wave conditions should be long-term *in situ* measurements of wave parameters. However, measurement campaigns are expensive, time consuming (since they are performed in real-time), and refer to some specific points. There is no possibility to cover large areas with buoy instruments. On the other hand, numerical models can provide us with equally good datasets of wave parameters with some extra advantages: good spatial coverage, reduced cost (in comparison with the measurements), easy way to update datasets (e.g., via reanalysis) etc

Wind-wave processes can be separated into three scales: generation, transformation, and local. Wave generation typically occurs in relatively deep water and across the continental shelf. The dominant processes for wave generation are atmospheric (wind) input, nonlinear wave-wave interactions, and dissipation (whitecapping). In intermediate to shallow water depths, wave transformation processes become dominant. These processes include wave shoaling, refraction, and breaking. In shallow depths and near coastal structures, local-scale process of diffraction, reflection, and wave nonlinearities govern. Although there is overlap in the wave processes between scales, numerical modeling approaches naturally fit into these three scales; see also Fig. 13.

Generation Scale Modeling: Wave generation occurs over tens, hundreds, and thousands of km, as momentum is transferred into the wave field by the winds. Wave heights and periods increase with wind speed, fetch (distance over which the wind blows), and time, up to fully developed conditions. Modeling of wave generation and propagation requires accurate wind field estimation and specification of the basin geometry. For coastal applications, wave generation modeling is performed at multiple scales, nesting toward the shore. The higher resolution close to the coast provides better definition of the land-mass sheltering, and bathymetry. Generation models are based on a statistical representation of waves using two-dimensional (frequency-direction) wave spectra. Spectral wave models, also known as phase-averaged models, do not save information about the relative phase of the spectral wave components because the phases are random. Generation-scale modeling has evolved from empirical relationships (based on dimensional analysis) to solutions of the action or energy balance equation. Komen *et* al (Komen et al., 1994) describes the evolution of spectral wave generation models. The WAM (The WAMDI Group, 1988) and WaveWatch III models (Tolman, 1991) are well established and run operationally for the greater meteorological centres in the world, such as ECMWF or NOAA.

Transformation Scale Modeling: The wave transformation processes of refraction, shoaling, breaking, and wind input dominate in intermediate water depths (depth less than approximately 15 to 60 m), which is within a few to tens of km from the coast. Wave heights may increase or decrease in shallower depths due to wave refraction and shoaling and wave directions refract to become more shore normal (wave crests parallel to shore). In very shallow depths, waves break where the wave height is of the same order as the water depth. To represent the bathymetry features that cause refraction, shoaling, and breaking, transformation-scale grid resolution is of the order of 30 to 300 m. Accurate nearshore bathymetry is required. The input to calculate wave transformation is the output from a wave generation model (e.g., WAM hindcast) or field wave measurements. Well known models for nearshore wave transformation applications are SWAN (Booij et al., 1999), MIKE21-SW (Sørensen et al., 2004) and STWAVE (Massey et al., 2011).

Local Scale Modeling: In areas where wave properties change on a subwavelength scale, a high-resolution local-scale model is required. These processes include reflection from breakwaters and jetties, diffraction around coastal structures, and phase-dependent wave nonlinearities (generation of harmonics and subharmonics), as well as refraction, shoaling, and breaking. Grid domains on the local scale are generally small (on the order of a few km or less) because the models are computationally intensive and the processes are localized. Numerical model grids must contain 8-10 grid cells per wavelength (resolution of 3 m). Input to calculate local-scale waves is typically output from a wave transformation model or field wave measurements. Accurate bathymetry and structure configuration is also required. These models are called phase-resolving and are based on Boussinesq-type equations, expressed through the conservation equations of mass and momentum (Madsen et al., 1991; Nwogu, 1993). Since these models describe the main physical processes in the coastal area at the intra-wave

scale, they require fine resolution in space and time and, therefore, their applications are often only suitable for small coastal areas and short-term simulations. See also the discussion in Sec. 4.4.2.

SWAN, MIKE21-SW, and STWAVE are third-generation spectral wave models based on the evolution of the wave action density spectrum N in time, geographical, and spectral spaces, given by the action balance equation (Holthuijsen, 2007):

$$\frac{DN}{Dt} = \frac{S_{\text{tot}}}{\sigma}, \tag{2}$$

where S_{tot} represents the source terms and σ the relative angular frequency.

In coastal applications, Cartesian coordinates are usually used in SWAN and MIKE21-SW. For these two models, the action balance equation can then be written as:

$$\frac{\partial N}{\partial t} + \frac{\partial c_x N}{\partial x} + \frac{\partial c_y N}{\partial y} + \frac{\partial c_\sigma N}{\partial \sigma} + \frac{\partial c_\theta N}{\partial \theta} = \frac{S_{\text{tot}}}{\sigma}, \tag{3}$$

where c_x, c_y are the propagation velocities of wave energy in spatial $x-$, $y-$space, c_σ and c_θ are the propagation velocities in spectral space $\sigma-$, $\theta-$space. The first term of the equation represents the rate of change of action density in time, the second and third terms represent the propagation of action density in the geographic space, the fourth term represents shifting of the relative frequency due to variations in depth and currents, and the fifth term represents depth-induced and current-induced refraction.

In the STWAVE model, the governing equation for steady-state conservation of spectral wave action is determined along the wave ray and is given by:

$$(C_g)_i \Big(C C_g \cos(\mu - a) \Big) N = \frac{S_{\text{tot}}}{\sigma}, \tag{4}$$

where μ stands for the wave ray direction, a is the wave direction (normal to the wave crest), C represents the absolute phase velocity, and C_g the absolute group velocity.

In the right hand side of both equations, S_{tot} represents several physical processes which generate, dissipate, or redistribute wave energ. It can be described by:

$$S_{\text{tot}} = S_{\text{in}} + S_{\text{nl}} + S_{\text{ds,w}} + S_{\text{ds,b}} + S_{\text{ds,br}}, \tag{5}$$

where S_{in} represents the generation of energy by wind, S_{nl} is the energy transfer due to non-linear wave-wave interaction, $S_{\text{ds,w}}$ is the dissipation of wave energy due to whitecapping (deep-water breaking), $S_{\text{ds,b}}$ is the dissipation due to bottom friction, and $S_{\text{ds,br}}$ is the dissipation of wave energy due to depth-induced breaking.

Various parametrizations for the source terms corresponding to each physical process are alternatively available in SWAN and MIKE21-SW. Generally, they are both flexible models, allowing the user to choose many of the parameters of the formulations for the source terms. STWAVE, on the other hand, only allows for the inclusion of some of the physical phenomena. Another difference among the models is the boundary forcings. Both SWAN and MIKE21-SW allow for the forcings to be applied to all open boundaries. STWAVE only allows for the forcings to be applied to one boundary (the one parallel to the coast and perpendicular to the wave propagation). MIKE21-SW and SWAN can perform simulations in both stationary and nonstationary modes and STWAVE only performs simulations in stationary mode.

Some comparative studies have been published with these models. Smith (Smith, 2006) has performed simulations of nearshore waves in coastal Louisiana for hurricane Katrina. To assess the impacts of the storm, a modeling study was conducted that included among others nearshore wave modeling. STWAVE was applied on four grids for the southern Louisiana area. For Hurricane Katrina, the winds are time varying and the grid domains are relatively large, so SWAN which is time-dependent model was used to evaluate the importance of time variation.

Strauss *et al* (Strauss et al., 2007) presented approximate results between SWAN and MIKE21-SW for the Gold Coast in Australia. SWAN showed greater sensitivity to the wind input, though it did not improve either model.

Fonseca *et al* (Fonseca et al., 2017) evaluated the performance of MIKE21-SW under different forcing conditions and target areas and compared it with both SWAN and STWAVE. These two last models were previously evaluated in studies targeting areas in the Portuguese continental coast; namely Obidos Bay (Rusu et al., 2011) Leixões Harbor, and Figueira da Foz (Gonçalves et al., 2015). Overall, similar results have been obtained by the two models in these studies.

Hoque *et al* (Hoque et al., 2017) compared the performance of SWAN and MIKE21-SW in simulations of storm-generated waves in the Mackenzie Delta region of the southern Beaufort Sea. In the case of nearshore shallow water observations, SWAN and MIKE21 simulations are close with SWAN to provide better simulation of H_S, whereas MIKE21 tends to be slightly better in estimating T_p. Comparisons of spectra suggest that MIKE21 tends to overestimate the spectral peak whereas SWAN tends to underestimate it. Comparison with deep water observations suggest that both models are better able to simulate H_S than T_p with their overall accuracy to be close. In addition, SWAN model gives a larger bias than MIKE21 in the case of the 1987 storm simulation at MEDS265, whereas SWAN model results give higher correlation with the measured values.

All the above mentioned works include comparison of the model results with *in situ* measurements from the examined area. A similar work for the Norwegian fjords, which consist a very special test case (narrow coastline, deep bathymetry, well away from the ocean etc), is missing from the literature and it would contribute significantly to the understanding of the various ongoing processes.

The basic scientific philosophy of SWAN is identical to that of WAM cycle 3. SWAN is a third-generation wave model and it uses the same formulations for the source terms. Whereas the WAM model considers problems on oceanic scales, with SWAN wave propagation is calculated from deep water to the surf zone. Since, WAM makes use of explicit propagation schemes in geographical and spectral spaces, it requires very small grid sizes in shallow water and is thus unsuitable for applications to coastal regions. For that reason, SWAN employs implicit schemes, which are more robust and economic in shallow water than the explicit ones. Note that SWAN may be less efficient on oceanic scales than WAM.

There have been extensive studies in the case of Bjørnafjord crossing from various Norwegian researchers by using different numerical models; see, e.g., (Eidnes et al., 2014; Stefanakos et al., 2015; Lothe, 2016; Koziel, 2017). Especially, in (Stefanakos et al., 2015), the Offshore-to-Nearshore transformation from the offshore point until the bridge points is performed in three steps, as shown in Fig. 14. The grid sizes vary from (75×115 km) (the outer grid), (21×19 km) and (14×30 km) (the intermediate grids), to (11×9 km) (the final grid in the fjord). At each step, the output is used as input for the next step.

As input for the offshore position (Location: 60N, 4.5E), time series of wind and wave parameters covering a period of ten years (01.08.2003–31.07.2013) have been used. Data are coming from WAM model as produced by the European Centre for Medium-range Weather Forecasts (ECMWF) calibrated using satellite altimeter data (Topex and Jason). The only global source of high quality and independent wave and wind data for direct validation of the wave model data for the entire period 1997 to 2006 are the Topex (1997 to September 2002) and Jason (September 2002 to 2006) altimeter data, although limited to significant wave height and wind speed. These data had been shown to have a particularly high quality for significant wave height, Hm0, in fact close to the accuracy of buoy data. This gives us the confidence to use the Topex and, similarly, Jason data globally as a reliable reference as if we had had buoy datasets worldwide.

In Figs. 15, an example of the spatial distribution of mean significant wave height and associated direction is depicted for the various grids used.

Furthermore, SWAN has also been implemented in studying wave conditions for Sulafjord and Halsafjord by the Norwegian Meteorological Institute (Furevik et al., 2018). Concerning the nesting of computational grids, similar approach has also been followed; see Fig. 16. The outer grid is (1×1 km), and the nested ones for the

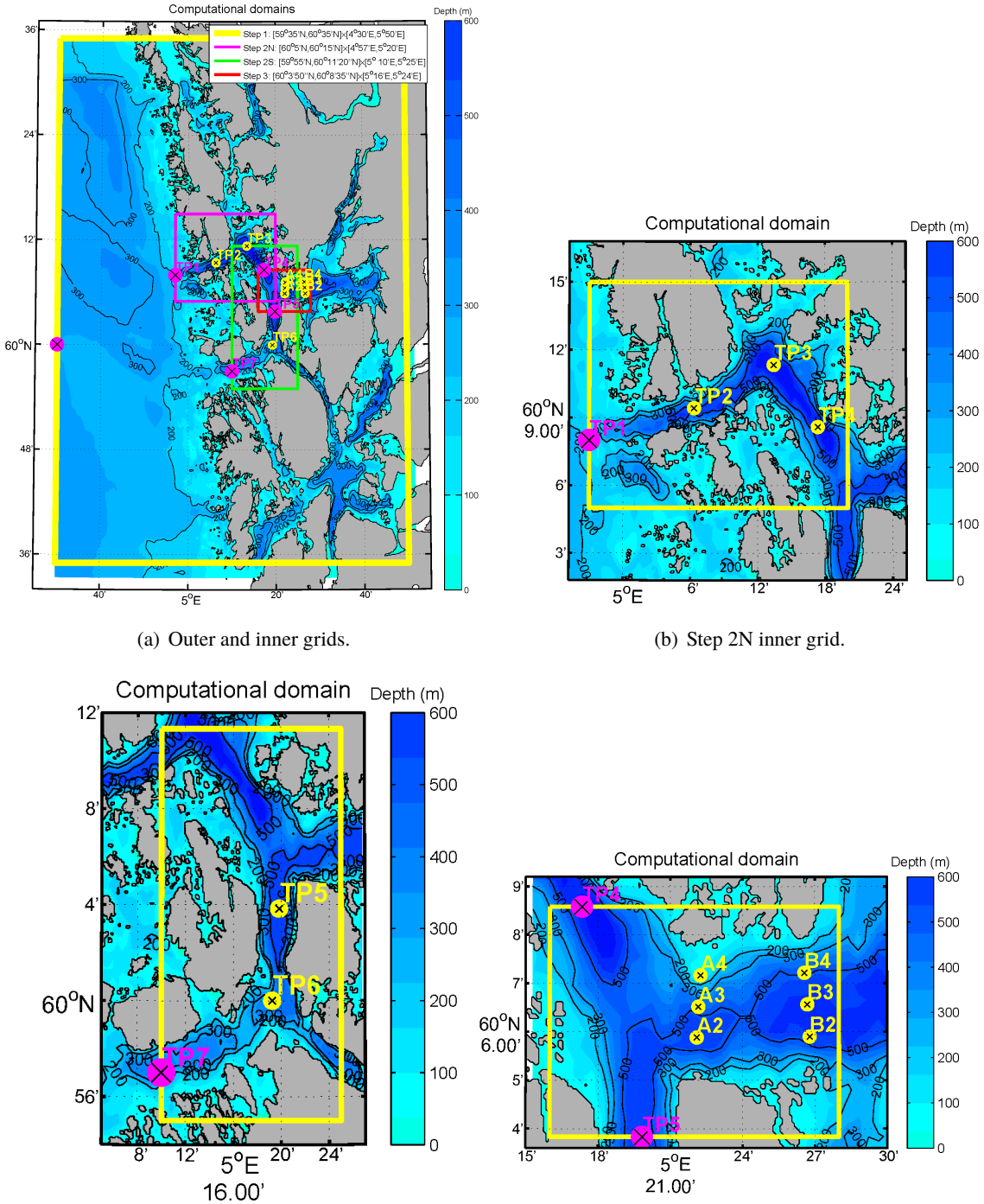

(a) Outer and inner grids.

(b) Step 2N inner grid.

(c) Step 2N inner grid.

(d) Step 3 inner grid.

Figure 14: Successive offshore-to-nearshore wave transformations in Bjørnafjord (Stefanakos et al., 2015).

two fjords (250×250 m). As forcing in the open boundaries, wave results from WAM model have been used as this is specially implemented for the Norwegian waters (NORA10). The simulation period was January 2007 - June 2017 and hourly integrated wave parameters and directional spectra have been derived.

In Fig. 17, an example of the spatial distribution of H_S is shown from Sulafjord.

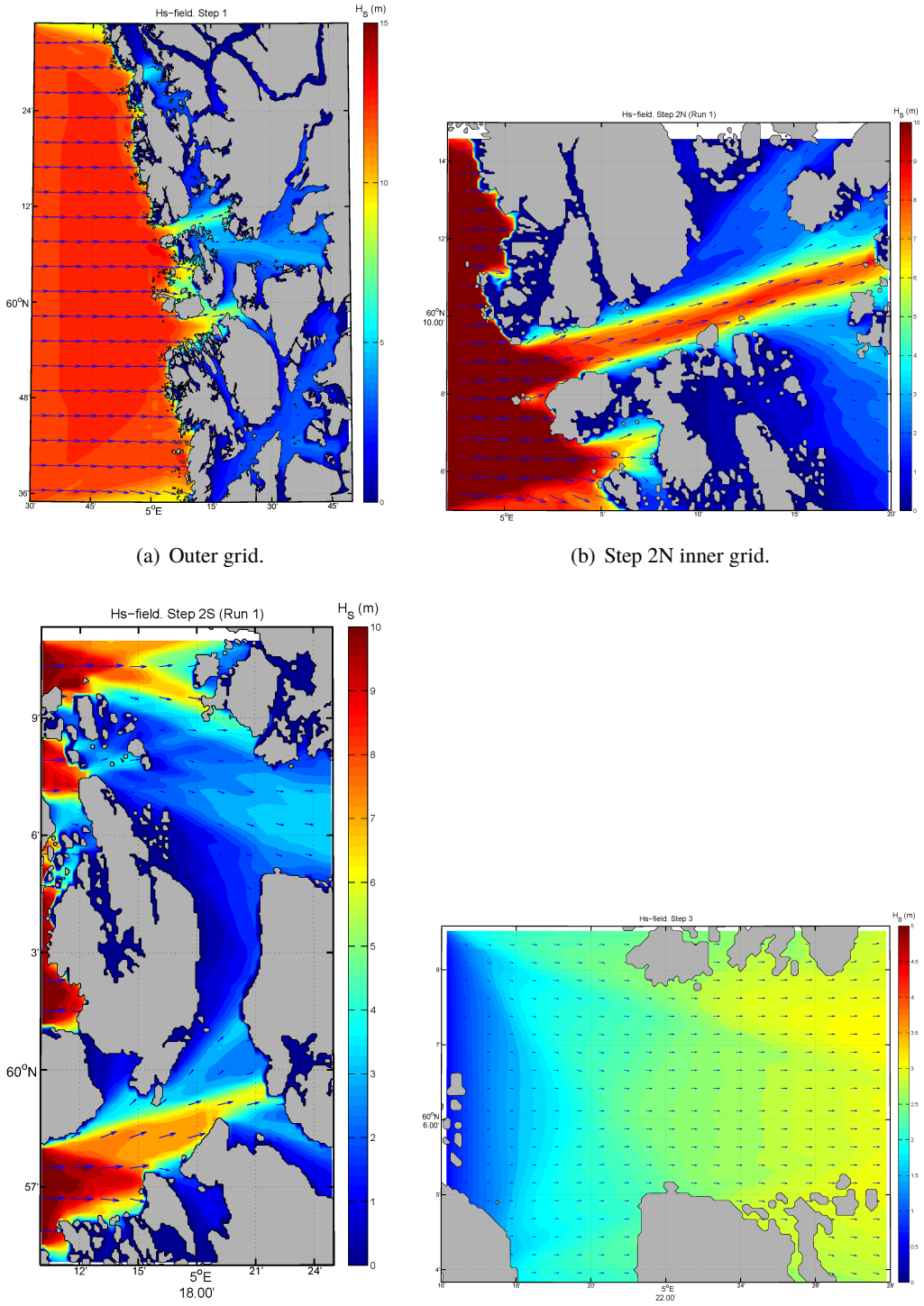

(a) Outer grid.

(b) Step 2N inner grid.

(c) Step 2N inner grid.

(d) Step 3 inner grid.

Figure 15: Examples of H_S-wave fields from Bjørnafjord (Stefanakos et al., 2015).

4.2.1 Modelling of local inhomogeneities in a fjord

In the above mentioned SINTEF report (Eidnes et al., 2014), a preliminary analysis of the wave climate in Bjørnafjord area was carried out by transferring offshore wave conditions to the nearshore (OtN) area of interest by applying wave model SWAN (Simulating WAves Nearshore), where only the northern passage had been taken

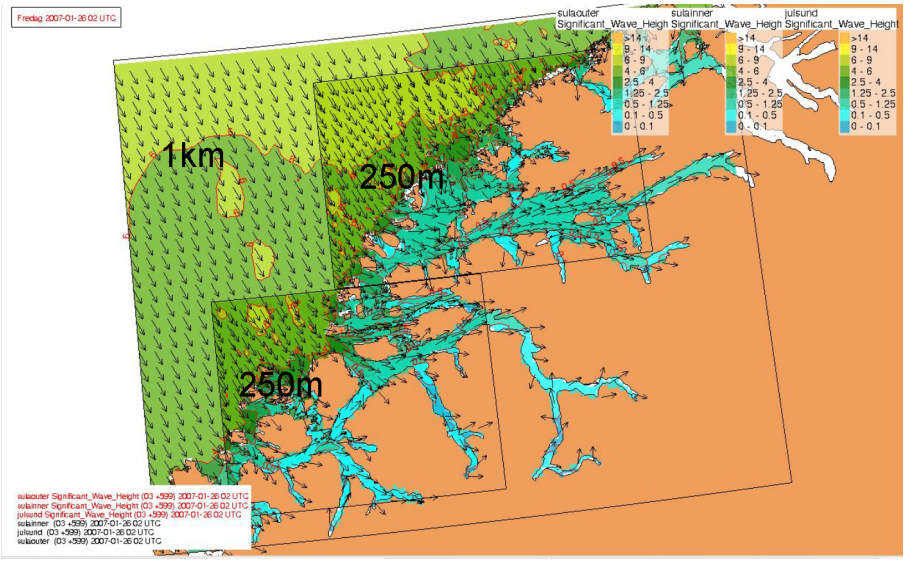

Figure 16: Nested offshore-to-nearshore wave transformations in Sula- and Halsafjord (Furevik et al., 2018).

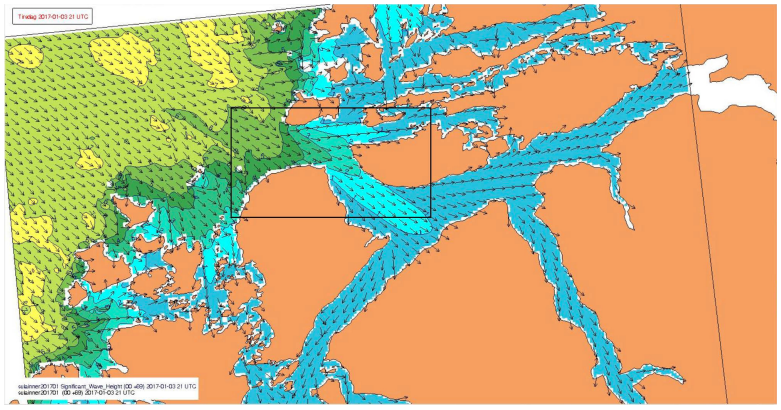

Figure 17: Example of wave field from Sulafjord (Furevik et al., 2018).

into account. This OtN transformation has been performed by using as input a very detailed bathymetry of the area and ten-year long time series of wave parameters from WAM model calibrated using satellite altimeter data. The OtN transformation was done in three consecutive runs, where the output of each one has been used as input for the next one. In this way, time series of directional wave spectra have been obtained for several locations along the bridge (5 locations $\times$ 2 alternative crossings); see Fig. 18. Of course, if a finer computational grid will be defined in the future, a denser (along the bridge crossing) set of time series of spectra can be generated. The obtained spectra are numerical, calculated for 25 frequencies and 12 directions, and one can post-process them in multiple ways to extract various useful information.

In the aforementioned report, based on the spectral information, the following results were given :

- Annual univariate pdfs of H_S, T_p, θ_{wave}, wave slope β_{wave}
- Annual bivariate pdfs of (H_S, T_p), $(H_S, \beta_{\text{wave}})$,
- Seasonal variation of monthly values of H_S, T_p, θ_{wave}, β_{wave}
- Directional Extremes of H_S (10, 20, 30, 40, 50, 60, 70, 80, 90, 100 years) in directional sectors (uniformly distributed)

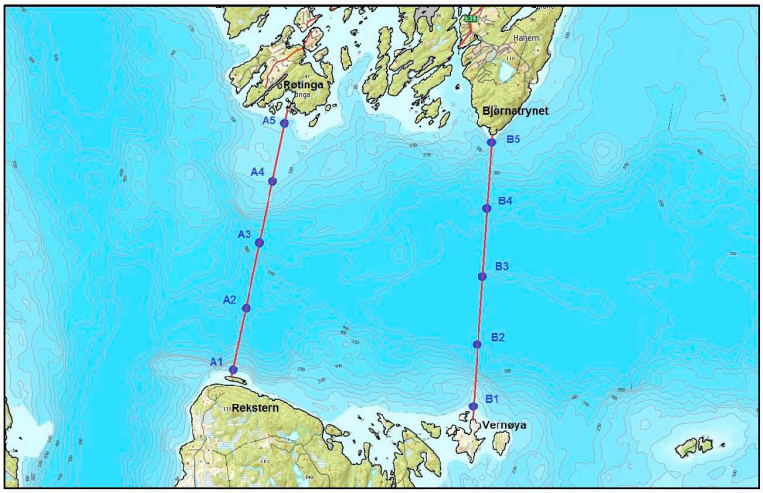

Figure 18: The ten points along the two alternative crossings in Bjørnafjord, for which model results have been extracted.

- Typical Spectra for the 50% and the 70% of the cases encountered in the time series.

Although the results were considered preliminary, and further analysis followed in (Stefanakos et al., 2015), they are in a reasonable agreement with the results given in the Design Basis report.

For example, one can compare the 100-year design wave height for the five points of one crossing scenario given in Table 1 with and the results given in the Design basis report shown in Table 2.

Table 1: Directional 100-year design wave heights for five points in the crossing of Bjørnafjord (Eidnes et al., 2014).

	Directions (deg)											
Point	15	45	75	105	135	165	195	225	255	285	315	345
A1	1.08	1.09	0.93	1.12	0.95	0.41	0.52	0.36	0.27	0.95	1.79	1.99
A2	0.93	1.02	1.04	1.03	0.78	0.52	0.69	0.71	0.63	1.39	2.14	1.83
A3	0.80	0.86	0.90	1.53	1.44	0.74	0.88	0.82	0.68	1.70	1.98	1.33
A4	0.64	0.55	0.62	1.56	2.14	0.95	1.02	0.88	1.05	1.85	1.47	0.74
A5	0.50	0.55	0.72	1.50	2.37	1.19	2.29	1.74	1.67	0.26	0.21	0.32

Table 2: Directional 100-year design wave heights in Bjørnafjord from the Design Basis (SVV, 2017).

Directions (deg)						
345-75	75-105	105-165	165-225	225-315	315-335	335-345
1.5	2.8	1.6	1.9	2.4	2.5	2.0

Another example of the usability of the time series of the numerical directional spectra is the following: one can calculate the bivariate probability spectral density (PSD). Then, one can for example obtain typical spectral forms for a number of cases (say, 50% or 70% of the cases encountered). In Figs. 19, such kind of typical spectra for the 70% of the cases is depicted. One can observe the variation of the spectra along the bridge crossing (as we are going from south to north: point A1 to point A5), as well as the variation in the spectral width and the orientation of the main spectral mass. These kinds of forms of the raw spectrum can be used in the sequel as

input to the response analysis models, avoiding the standardized forms (e.g., Jonswap), and at the same time introducing measures for the level of uncertainty of the input and subsequently of the output.

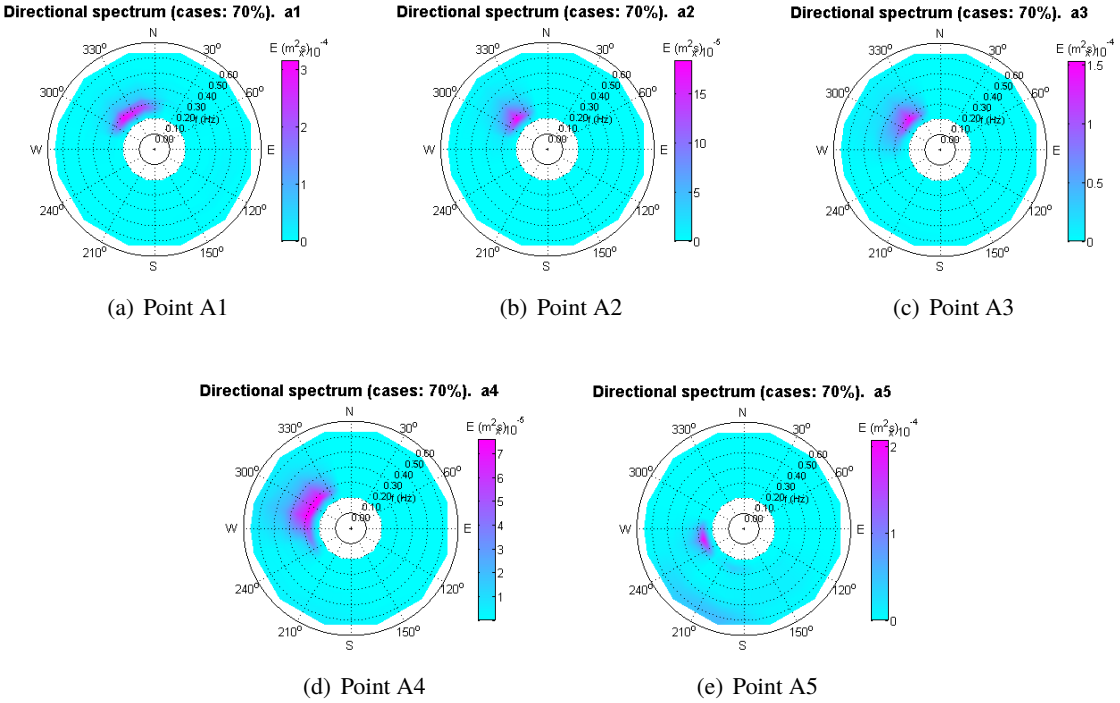

(a) Point A1 (b) Point A2 (c) Point A3

(d) Point A4 (e) Point A5

Figure 19: Typical directional wave spectra (70% of the cases) along the Bjørnafjord crossing (Eidnes et al., 2014).

Similar spectral information for nearshore locations should have been available during the runs in Sulafjord, although they haven't been reported during the workshop (Furevik et al., 2018).

Further, and in order to study the correlation of the design wave conditions along a crossing, multivariate environmental contours can be derived based on the time series obtained by the runs of the numerical model.

4.3 Available wave measurements in Norwegian fjords

Recently, the first measurements from Bjørnafjord have been analysed by NTNU (Cheng et al., 2018b; Cheng et al., 2018a). The data come from three datapoints along the bridge; see also Fig. 20. They cover a short period of 1-1.5 years as follows:

- DWR1 (2016.02-2016.10; 2017.01-2017.10)
- DWR3 (2016.02-2017.10)
- DWR4 (2016.02-2017.10) (out of work during 2016.12.10 –2016.12.30)

Figure 20: Locations of wave buoys in Bjørnafjord (Cheng et al., 2018b).

The data include:

- Significant wave height H_S
- Peak period T_p
- Averaging zero up-crossing period T_Z
- Mean direction
- Dominant direction
- …

It was identified that measurements contain a part related to ship waves produced by the sailing ships in the area, and this part has first to be filtered out before an analysis of the data take place.

To the authros' knowledge, there is no work published on the validation of the model results presented in the Design basis report (SVV, 2017) with the measurements from Bjørnafjord.

Norwegian Public Roads Administration announced that the measurements for Halsafjorden, Sulafjorden og Vartdalsfjorden through deployed wave gauges and wind turbines are now available. Measurements have been

made by Fugro Oceanor and Kjeller Vindteknikk, and the Meteorological Institute is responsible for data management. All measurements are stored at the Meteorological Institute on an open data format. The official data base of the Norwegian Public Roads Administration is freely available to the public for use.

In addition, a measurement campaign is under way for Sulafjord and Halsafjord. The buoys are deployed at the locations shown in Fig. 21, and their metadata are given in Table 3.

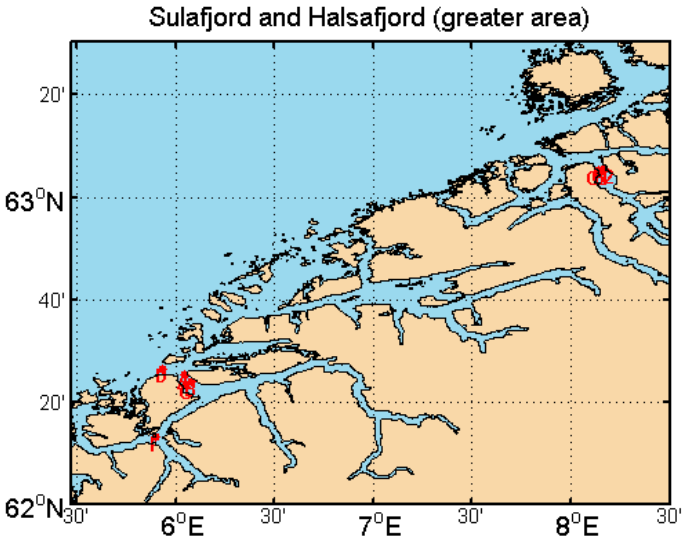

(a) Greater area of Sula- and Halsafjord

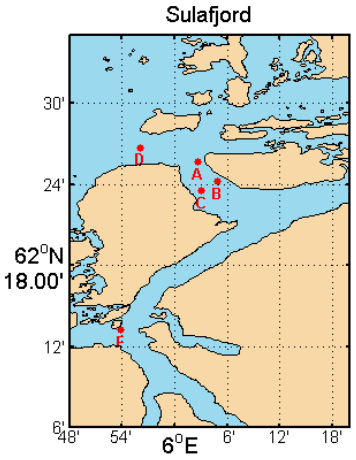

(b) Sulafjord

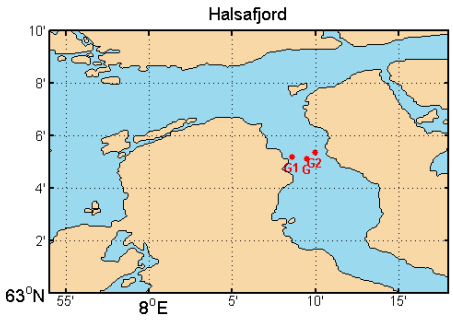

(c) Halsafjord

Figure 21: Locations of wave buoys in Sulafjord and Halsafjord.

First results of the analysis of the buoys are given in (Wang et al., 2018a), where 15 months of measurement data from four wave buoys A,B,C,D were analyzed and compared with results from the nearest hindcast point of the NORA10 grid at (62.67N, 4.42E). Although measured data are available at 10-min intervals, samples averaged over 1-h intervals are used for the analysis. Datasets include the following wind and wave parameters:

- Mean wind direction θ_{wi}
- Mean wind velocity U
- Mean wave direction θ_{wa}

Table 3: Wave measurements for E39 in Møre.

Station	Location	Position		Depth	Measurement	
		Latitude	Longitude	(m)	started	stopped
A	Sulafjorden	62° 25,62’	06° 02,60’	375	2017.10.02	2018.03.31
B	Sulafjorden	62° 24,23’	06° 04,84’	325	2017.10.02	2018.03.31
C	Sulafjorden	62° 23,53’	06° 03,05’	445	2017.10.02	2018.03.31
D	Breisundet	62° 26,71’	05° 56,02’	315	2017.10.06	2018.03.31
F	Vartdalsfjorden	62° 13,26’	05° 53,87’	217	2017.11.29	2018.03.31
G	Halsafjorden	63° 05,14’	08° 09,45’	495	2017.10.02	2018.03.31
G1	Halsafjorden	63° 05,21’	08° 08,56’	133	2017.10.02	2018.03.31
G2	Halsafjorden	63° 05,37’	08° 09,96’	146	2017.10.02	2018.03.31

- Significant wave height H_S
- Spectral peak wave period T_p

Their findings are summarized in Section 4.4.2.

4.4 Identified and/or applied wave parameters / characteristics / standards

4.4.1 Bjørnafjorden

As per June 2018 the MetOcean design basis of the National Public Roads Administration (SVV, 2017) for waves assumes constant wave conditions along the bridge crossing, because it is believed that there are no adequate data to give reliable estimates of the wave energy along the bridge crossing. The following statistical information is given there:

- Design wave conditions (H_S, T_p) for locally generated wind waves (1, 10, 100, 10 000 years) in directional sectors (non-uniformly distributed)
- Design wave conditions (H_S, T_p) for locally generated wind waves (1, 10, 100 years) for the summer season (May to August)
- Design wave conditions (H_S, T_p) for swell (1, 10, 100, 10 000 years)
- Design wave conditions (H_S, T_p) for swell (1, 10, 100 years) for the summer season (May to August)
- Annual and monthly frequency tables of occurrence of (H_S, T_p) [Wind sea, 6 years of simulated data]
- Annual and monthly frequency tables of occurrence of (H_S, T_p) [Swell, 37 years of simulated data]
- Fit of JONSWAP spectra with average spectral width ($\sigma_a = 0.07$ and $\sigma_b = 0.09$) and gamma parameter in the range $\gamma = 1.8 - 2.3$.
- Recommendations for directional spreading of cos-type with exponent $n = 4 - 6$ (wind waves) and $n = 10 - 20$ (swell)
- Probability density functions (pdfs) of the difference $\theta_{\text{wave}} - \theta_{\text{wind}}$ in directional sectors (non-uniformly distributed) for the middle of the bridge crossing

Estimates are based on simulations from (Lothe, 2016) and (Svangstu, 2016). Procedure for combining results from analysis and validation of analysis results can be found in (Svangstu, 2016).

Design wave conditions for locally generated wind waves are given in Table 4, while wave conditions for the summer season (May to August) are given in Table 5.

Table 4: Wind generated waves, All year (SVV, 2017). 1) Direction 0° is waves coming from north, 90° is east, 180° is south and 270° is west 2) Wave conditions are constant within each sector 3) The upper limit of the Tp includes an added margin of 0.5s for 1, 10 and 100 year return periods 4) Lower peak periods shall also be assessed, if a Hs/Tp combination exceeds wave breaking criteria, then the wave height shall be reduced to fit the limiting wave breaking criteria

Return period /	1 year		10 year		100 year		10 000 year	
Sectors	Hs [m]	Tp [s]	Hs [m]	Tp [s]	Hs [m]	Tp [s]	Hs [m]	Tp [s]
345°–75°	0.8	4.0	1.1	4.5	1.5	5.0	2.3	5.4
75°–105°	1.6	5.3	2.2	5.9	2.8	6.6	3.9	7.1
105°–165°	1.1	4.4	1.3	4.8	1.6	5.3	2.3	5.6
165°–225°	1.2	4.4	1.5	4.9	1.9	5.3	2.7	5.6
225°–315°	1.3	4.6	1.8	5.3	2.4	5.9	3.3	6.3
315°–335°	1.5	5.1	1.9	5.6	2.5	6.2	3.5	6.7
335°–345°	1.2	4.3	1.6	5.0	2.0	5.6	2.9	6.0

Table 5: Wind generated waves, Summer (May-August) (SVV, 2017)

Return period /	1 year		10 year		100 year	
Sectors	Hs [m]	Tp [s]	Hs [m]	Tp [s]	Hs [m]	Tp [s]
345°–75°	0.5	3.3	0.6	3.5	0.9	4.0
75°–105°	0.9	4.2	1.3	4.8	1.8	5.4
105°–165°	0.6	3.6	0.8	3.9	1.0	4.4
165°–225°	0.7	3.5	0.9	4.0	1.2	4.4
225°–315°	0.8	3.8	1.1	4.4	1.5	4.8
315°–335°	0.9	4.2	1.2	4.5	1.6	5.1
335°–345°	0.7	3.4	1.0	4.0	1.2	4.5

From the numerical modelling in (Eidnes et al., 2014), local spatial variations in Bjørnafjorden are observed, both in power spectra but also in directional spectra; see also discussion in Sec. 4.2.1.

Waves from passing vessels During the measurement campaign in Bjørnafjorden, there has been observed a significant number of cases that are presently believed to be waves induced by passing vessels. Many of these cases give waves with periods around 6 seconds. The periods of vessel generated waves are dependent on the vessel speed; 20 knots gives waves with periods around 6 seconds, which is a case that matches fairly well with the ferries crossing Bjørnafjorden.

When a bridge is built in the future, there will most likely be traffic control of the ship traffic in the area, and in that context a speed limit around 12 knots have been suggested. With a speed limit of 12 knots, the wave periods of vessel generated waves will be so short that the wave energy of such events will be negligible compared to the wave energy from wind driven seas.

But even if speed restrictions are enforced in Bjørnafjorden when the bridge is completed, the concepts need to be robust enough to withstand the loading from waves generated by rogue vessels that do not follow these speed restrictions.

The following cases with vessel generated waves shall be considered for the concepts as Accidental Limit State (ALS) cases, as shown in Fig. 22. The time series are established with a time step of 0.1s. For more information on how these time series are established, the reader is referred to (Svangstu, 2016).

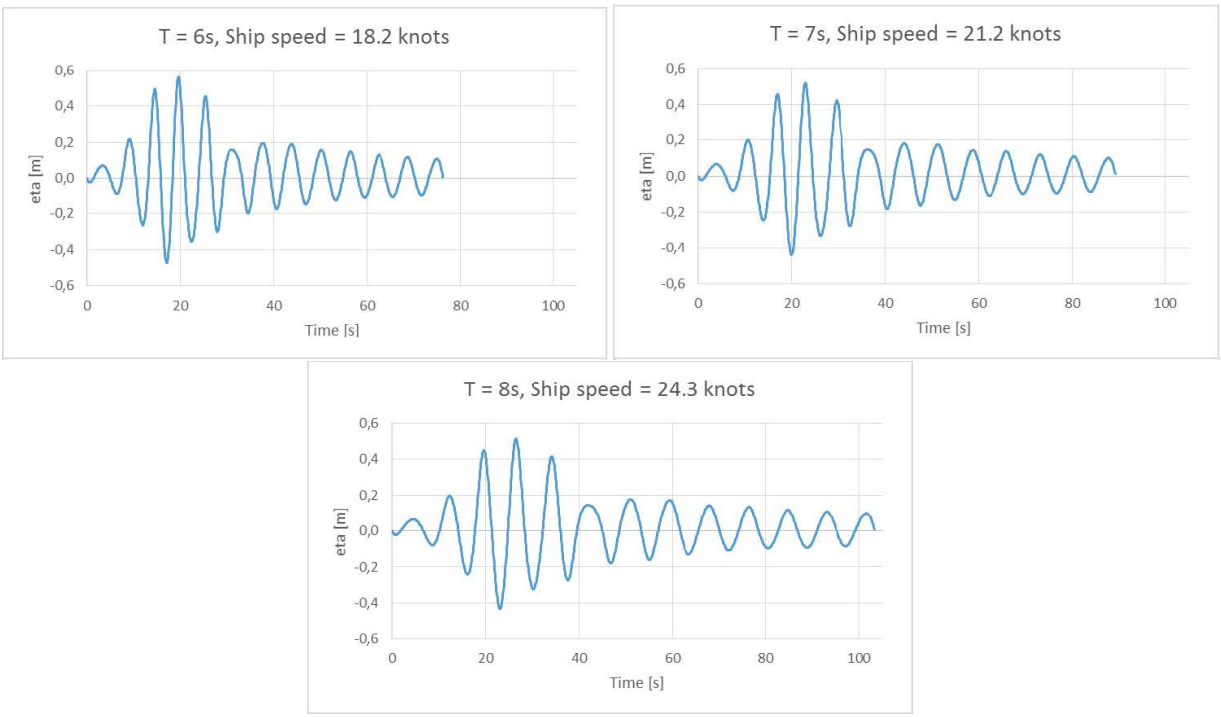

Figure 22: Vessel induced waves in Bjørnafjord crossing (SVV, 2017).

4.4.2 Sulafjorden and Halsafjorden

The Design basis has not yet released, as per June 2018. However, there are some first works for the metocean conditions in Sula- and Halsafjord.

In (Lie et al., 2016), in studying two bridge scenaria, the authors assumed the environmental conditions given in Table 6 for the area along the bridge.

In addition, Meteorological Institute (Furevik et al., 2018) presented first results from the analysis using SWAN model, in a Workshop held early March 2018 in SINTEF premises. Among other analyses, they presented

Table 6: Environmental Parameters along the bridge in Sulafjord (Lie et al., 2016)

	Extreme swell		Extreme wind waves		
Sections (from West to East)	H_S (m)	T_p(s)	H_S (m)	T_p(s)	Current (m/s)
Section A (0 – 1 km)	0.7	16-18	2	5-6	1
Section B (1 – 2 km)	1.1	16-18	1.9	5-6	1
Section C (2 – 3 km)	2.3	16-18	2.4	7-8	1
Section D (3 – 4 km)	3.0	16-18	2.8	8-9	1

directional extreme values of significant wave height. In Table 7, H_S-values are given for return period of 100 year for 12 directional sectors in 3 locations for Sulafjorden.

Table 7: 100-yr H_S return values for 12 directional sectors for Sulafjord (Furevik et al., 2018)

Sector	360	30	60	90	120	150	180	210	240	270	300	330	all
Sula Nord	1.0	1.0	0.5	0.3	1.0	1.9	2.2	2.2	2.5	2.8	5.2	1.7	5.2
Sula Midt	1.2	1.2	1.1	1.4	1.6	2.0	1.9	1.7	1.6	1.7	3.1	2.9	3.2
Vartdalsfjorden	0.4	1.0	0.9	0.4	0.4	0.9	1.6	1.9	0.7	0.3	0.3	0.2	1.9

In (Wang et al., 2017b), the authors have performed large scale three dimensional simulations of wave propagations into Sulafjord with the CFD model REEF3D. The spectra wave model SWAN is used to obtain the wave data from offshore data and give inputs for the CFD simulation. The CFD simulations are performed with both regular and irregular waves and give the details of the free surfaces and wave transformations in the fjord, the results of which are also compared with the wave model SWAN; see Table 8.

Table 8: The comparison of the wave properties at probes from the SWAN simulation, the regular wave CFD simulation and the irregular wave CFD simulation in Sulafjord (Wang et al., 2017b)

Buoy	SWAN		Regular wave CFD		Irregular wave CFD	
Locations	H_S	T_m	H_S	T_m	H_S	T_m
D	4.67	9.95	5.33	16.86	6.91	8.38
A	2.57	9.71	7.31	16.92	5.11	7.53
B	2.28	9.37	7.41	16.97	5.12	8.68

In (Wang et al., 2018a), the authors analyzed comparatively the first 15 months of measurements from four wave buoys in the fjord that became available, as well as hindcast data at an offshore site outside of the fjord. The results indicate that the waves in the fjord are coming from a narrow direction ranging from 285^o to 315^o, compared to more scattered offshore waves. The narrow wave distribution in the fjord is caused by the combined effects of 1) the fjord geometry; 2) a deep-water trench to the northwest of the fjord inlet which provides the passage for the offshore waves and 3) the shallow water area and some islands to the west of the fjord inlet which absorbs the incoming offshore wave energy.

Further, they performed a storm events analysis, which suggests a maximum H_S reduction factor and a consistent T_p from offshore to the fjord, with one exceptional storm event that the local wind might have contributed much to the large waves in the fjord as well, which will be investigated when measured directional wave spectra are available. The POT and the ID extreme-value method are adopted to estimate the extreme significant wave height, suggesting the 100-year H_S close to the potential bridge floating tower location to be above 2.8 m. A joint distribution of the wave conditions, with a $H_S - T_p$ contour lines plot, is also established.

4.4.3 Sognefjorden

Sognefjorden is the deepest and largest fjord of Norway. To the authors knowledge, there are no other recent research about metocean conditions, except a preliminary SINTEF report (Lothe and Brørs, 2010) with a feasibility study about waves and currents for the Opedal-Lavik crossing.

According to this report, local swell generated due offshore wave conditions has a 100-year return significant wave height of 0.1 m with a corresponding peak period 13-14 s and mean direction in the sector 210-240 deg.

In addition, mean direction of the local wind waves coincides with the mean wind direction, and extreme values of significant wave height have the same return periods as the wind speed (e.g., 100-year wave height is created by a 100-year wind speed). Especially the directional distribution of the 100-year H_S for the midpoint of the crossing (at a depth >1000 m) is given in Table 9.

Table 9: Extreme values of significant wave height for 100-year return period in the midpoint of the crossing in Sognefjord (Lothe and Brørs, 2010)

Directions (deg)											
0	30	60	90	120	150	180	210	240	270	300	330
0.79	1.47	1.81	1.40	1.07	1.11	1.79	2.24	2.34	1.83	1.39	0.76

4.5 Gaps and recommendations

It is not possible to give a specific range of values for metocean conditions, since each fjord is situated in a different location with a different exposure to the open ocean conditions, coastline and bathymetry of different complexity etc. However, what is common practice in all situations is the procedure that should be followed.

First, long-term offshore wind and wave conditions near the fjord should be analysed from a reliable source of data (e.g., model or measured data). Then, a detailed bathymetry of the area should be derived and be combined with the offshore conditions to transfer them from offshore to nearshore using a neasrshore wave model such SWAN or MIKE21-SW.

The quality of input (both offshore conditions and coastline/bathymetry) is very important and determines to a large extent the quality of the output. Another important factor is the definition of the appropriate computational domain, as well as the nesting scheme to be applied as we approach the target points.

In this way, one can obtain long-term time series of directional wave spectra at various locations in the area of interest (e.g., along a bridge crossing). This kind of data is of fundamental importance for the study of the nearshore wave climate. It can be served to obtain a number of useful statistics including (but not limited to) extreme values, joint probability densities, directional fields of mean values, seasonal variation of main parameters, wind and wave roses, probability densities of spectra etc.

In addition, typical (or most frequently occurred) forms of numerical spectra can be directly used as input to response analysis models without the need of assuming *a priori* a specific analytic form for them.

There is an increasing literature concerning the coupling of wave models with current modelling to improve predictions in both of them; see, e.g., (Chen et al., 2018, and references cited therein). However, all cases examined in the literature concern very shallow water ($<$50 m), where other phenomena are present and which is certainly not the case in the Norwegian fjords.

Further, one can identify some gaps in the existing methodologies used:

1. There are no validations of results obtained by numerical models (SWAN, MIKE21-SW, STWAVE etc) with extensive *in situ* measurements and systematic runs of CFD codes for the topography of the Norwegian fjords
2. Phase averaged (by default) models do not give any information about the phase
3. Inhomogeneous wave conditions can partially studied by the obtained spectra at various locations. Additional runs of CFD codes may further validate this

5 Wind

Constructions and buildings must take into account in their design the environmental loads, such as the wind loads. Wind loading on structures is a multidisciplinary subject. It involves probability and statistics, meteorology, the fluid mechanics of bluff bodies, and structural dynamics. This Chapter will focus on the meteorological and statistical aspects of wind before looking into more details at the specific case of wind in Norwegian fjords.

Meteorology Meteorology is the study of the atmosphere that focuses on weather processes and forecasting. Weather processes take place at various scales:

- **Synoptic scale** has a horizontal length scale of the order of 1000 kilometres or more. This corresponds to a typical mid-latitude depressions. Most high and low-pressure areas seen on weather maps are synoptic-scale systems.
- **Mesoscale** comprises weather systems from about 5 kilometers to several hundred kilometers. Examples of mesoscale weather systems are sea breezes, squall lines, and thunderstorms. Vertical velocity often equals or exceeds horizontal velocities in mesoscale meteorological systems.
- **Microscale** corresponds to atmospheric phenomena about 1 km or less. Important topics in microscale meteorology include heat transfer and gas exchange between soil, vegetation, and/or surface water and the atmosphere caused by near-ground turbulence.

Microscale events are strongly dependent on mesoscale events, which are in turn dependent on the synoptic scale events. In order to understand the local effects occurring on the Norwegian coastline, it is therefore important to take a step back and study larger scale features of the atmosphere. In Section 5.1, the main drivers of the synoptic wind will be briefly explained before describing a range of mesoscale and microscale wind effects. Atmospheric models, used for Numerical Weather Prediction (NWP) as well as for hindcasting (reanalysis), are also listed in this Section, together with a description of their main features. Finally, different measurement techniques that can be used to characterize the wind field are presented.

Statistics When analyzing the wind at a location of interest, it is commonly assumed that the wind is homogeneous and stationary, and to describe it based on short and long term statistics (Strømmen, 2010). Short term statistics are time domain representatives for the conditions within a certain weather situation. Long term statistics are ensemble representatives extracted from a large set of short term conditions. Section 5.2 first defines the different long-term and short-term wind statistics of interest in structural engineering. Existing models for short-term statistics are listed together with the assumptions under which they are valid. Reference is also made to the Standards and their recommendations are summed up. Numerical tools which can be used in structural engineering to reconstruct a uniform wind field based on given short-term statistics are then presented.

Norwegian coast In Norwegian coastal areas, large variations are observed in the wind field related to the transition from sea to land and the sharp topographic features of the coastline. Section 5.3 looks first at the conditions of occurrence of local effects. Atmospheric models used by the Norwegian Meteorological Institute are then listed. Finally recommendations of how to combine the different tools available to characterize the wind in a Norwegian fjord are then given.

Main findings from measurements performed in Bjørnafjord, Lysefjord and Sulafjord are also reported in Section 5.4.

Gaps The complex nature of the wind field in Norwegian fjords creates a need for a better understanding of the wind in fjords and a more accurate definition of the wind field. In particular when the wind direction is from land, there are large variations in the coastal wind field related to fjords and other topographic features. The

topographic effects can be traced in the wind field several hundred kilometers offshore. Section 5.5 closes this report with a list of identified gaps.

5.1 Atmospheric wind

5.1.1 Physics

Wind is due to large-scale pressure differences in the atmosphere, that are produced by differential solar heating of different parts of the earth's surface (Holmes, 2015). The air tends to flow from high pressure to low pressure zones to recover a pressure balance, creating wind. As described in Section 6.1.7, the Coriolis effect deflects the wind trajectory towards the right in the Northern hemisphere and towards the left in the Southern hemisphere. The wind resulting from the balance between the pressure gradient and the Coriolis force is called geostrophic wind and is directed parallel to the isobars, thus moving perpendicular to the pressure gradient (Figure 23).

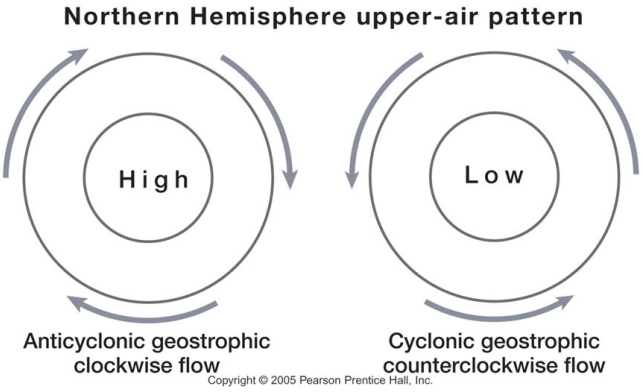

Figure 23: Geostrophic wind around a high and a low pressure in the Northern hemisphere.

Close to the ground, true wind rarely corresponds to geostrophic wind. In the lower layer of the atmosphere, the wind is affected by friction from the ground, vertical thermal stability of the atmosphere and major topographical features. Those effects are creating eddies or vortices within the air flow, also known as turbulence or gustiness.

As the earth's surface is approached, frictional forces slow down the flow by acting in a direction opposite to the flow direction and the wind vector gradually turns towards the low pressure center. The wind direction can vary up to 30 degrees between the geostrophic and the surface wind due to ground friction alone. This is known as the Eckman Spiral. The influence of ground friction depends on the roughness of the surface. Rougher surfaces (such as hills, trees, and tall buildings over land) result in more drag and thus lesser winds and large cross isobar angles, while over smoother surfaces (such as the ocean or bodies of water) the winds are more nearly geostrophic. The ground friction effect is illustrated by measurement of surface wind over the inland waters of Washington in Figure 24.

Vertical stability affects vertical mixing of the flow. Unstable situations (cold air above warm air or warm water) triggers vertical mixing with fresh, unslowed air from above to allow the surface winds to be more geostrophic. In stable situations, the lack of vertical mixing results in the surface friction effects being concentrated in a shallow layer near the surface causing far more slowing of the air near the surface.

Large topographic features (such as mountain ranges) greatly alter the geostrophic wind by deflecting the wind which has to go either around or above the barriers to flow from high to low pressure zones (depending on the size of the obstacle and the vertical stability), or across gaps in the topographical barrier (such as mountain passes or straits).

More about those topics can be found at `https://atmos.washington.edu/~cliff/Navygap5.html` or `http://web.gccaz.edu/~lnewman/gph111/topic_units/pressure_winds/pressure/pressure2.html`.

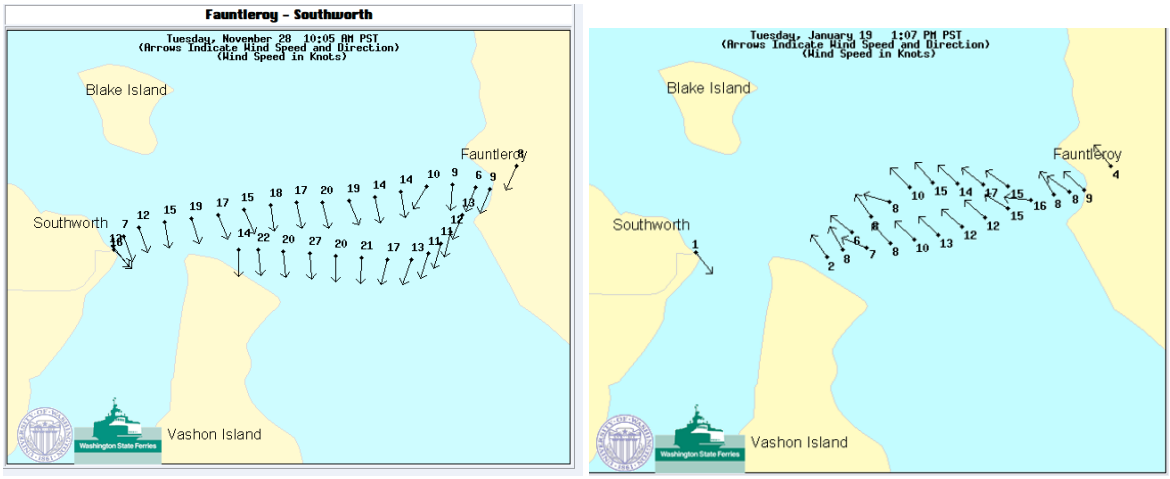

Figure 24: Surface friction effects illustrated `http://i90.atmos.washington.edu/ferry`

5.1.2 Local effects

Gap winds with pressure gradient Gap winds are low-level surface wind that are associated with gaps or low areas in terrain. Those winds are characterized by large changes of wind at their upper and lateral boundaries. For most narrow gaps less than 100-200 km wide, the along-gap winds are not in geostrophic balance and the air flows directly down the gap towards lower pressure. Gap winds are generally strongest when there is a large difference of pressure across a gap. The flow accelerates down the pressure gradient from high to low pressure, resulting in strongest winds over the exit region of the gap (not at the narrowest section or constriction). Therefore, gap winds are not only important within the gaps, but well downstream as well. There can be some Venturi acceleration in narrow regions, but that tends to be secondary.

The pressure gradient along the gap has two origins: the synoptic pressure and the temperature gradient between both ends of the gap. In coastal areas, the inland air is generally relatively cold and dense compared to the temperate marine air on the coast. As inland air approaches a gap, the depth of the approaching cold air generally increases due to the blocking effects of the surrounding terrain resulting in higher pressure near and upwind of the center of the gap, which tends to decelerate the gap flow as it approaches the gap (Figure 25). As the air moves through the gap exit region, the rapid widening of the gap causes the gap flow to spread out horizontally. This horizontal divergence of the gap flow causes the height of the dense low-level air to collapse, resulting in lowered pressure and a pressure gradient that accelerates the winds over the exit region.

Often air in a gap does not simply move horizontally from the upstream source region to the exit, but rather air can flow into the gaps from several directions and from several levels along the length of the gap, resulting in complex three dimensional air flows in the gaps.

The wind velocity in gaps can be roughly estimated with a modified form of the Bernoulli equation, which includes added terms for friction (Equation 6). Two types of drag must be considered in gaps: the surface friction due to the roughness of the topography, and the drag due to mixing at the upper boundary of the gap.

$$u(x)^2 = \left[u_0^2 - \frac{\Delta p}{k\rho}\right] e^{2kx} + \frac{\Delta p}{k\rho} \tag{6}$$

where x is the distance from the gap entrance, u_0 is the initial wind speed, Δp is the pressure gradient at x, k is a friction coefficient, and ρ is the air density.

Gap winds without pressure gradient In the case of a chain of narrow mountainous islands with substantial gaps between the islands, weak winds are generally observed in the wake of each island while the wind remains

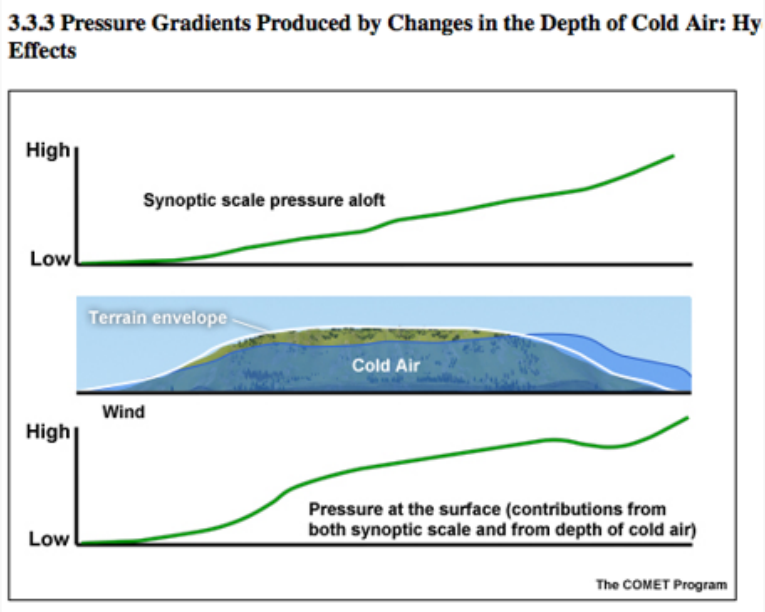

Figure 25: Pressure gradients produced by changes in the depth of cold air.

nearly unchanged in the gap regions.

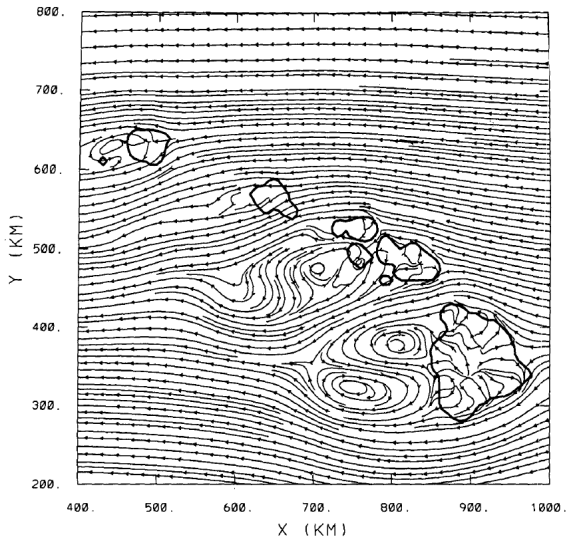

Figure 26: Lee vorticies in the wake of Hawaiian islands. Thick solid lines are island boundaries. Thin solid arrowed lines are streamlines. (Reisner and Smolarkiewicz, 1994)

Downslope wind Downslope winds are initiated by cool air from behind or above a slope falling to the base of the hill, spreading out and dissipating as gusty winds. Gusts at the foothills are often observed to be two to three times stronger than the prevailing wind. Turbulent and reverse flow winds are also observed for some kilometres downstream. They are more common in summer than winter and are strongest overnight and into the early morning as a result of mountain breeze.

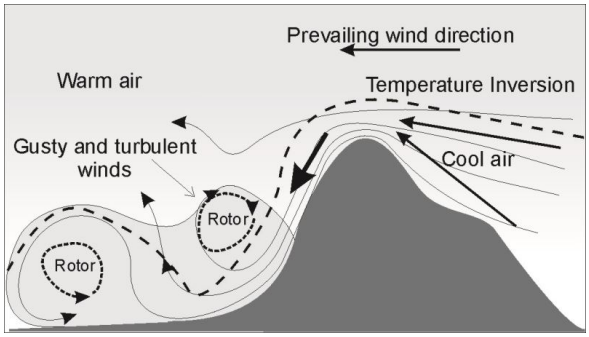

Figure 27: Gusty and turbulent winds generated by cool air, surging down a mountain slope into a warmer air mass on the lee side.

Mountain breezes Along mountain sides, mountain and valley breezes can develop on clear warm days, when the synoptic wind are light. During the day, the sun heats up the ground in the valley which warms up the air in contact with the ground. The heated, lighter air rises up the mountain sides, known as valley breeze. During the night, the mountain sides cool down quickly which cools down the air in contact with the ground. The denser air flows down the mountain sides, known as mountain breeze.

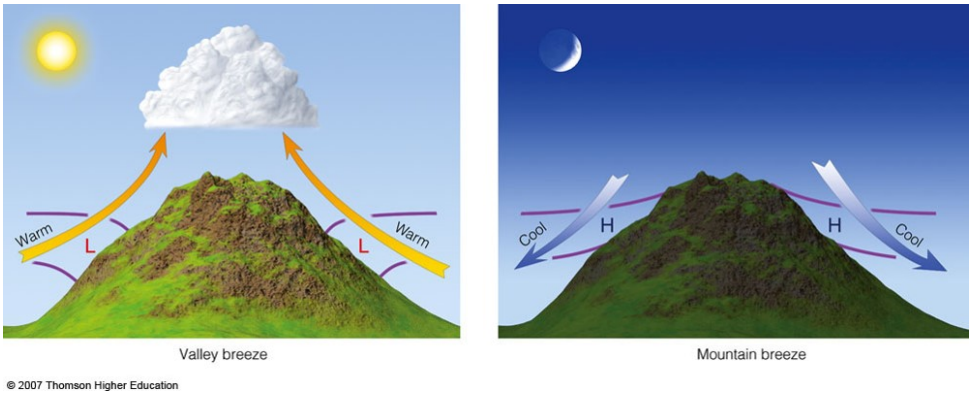

Figure 28: Schematics of mountain and valley breeze (Ahrens, 2011)

Sea breeze Along relatively flat coastal terrain, sea breezes can develop on clear warm days, when the synoptic wind are light. During the day, the sun heats up the ground faster than the sea, which warms up the air in contact with the ground. The heated, lighter air rises up creating local low pressure zone. As a result of this local pressure gradient, air flows from the sea toward the land, known as sea breeze. During the night, the ground cools down faster than the sea, which cools down the air in contact with the ground. The denser air flows downwards creating a local high pressure zone. As a result of this local pressure gradient, air flows from the land toward the sea, known as land breeze.

Roughness change Transitioning from rougher to smoother ground surfaces, it generally takes a few kilometers to reach a new fully developed wind flow.

(Cheynet, 2016) about the strong TI for SSW wind on 22/05/2014: ”As pointed out by Antonia and Luxton (1972), this type of roughness change may increase the turbulence intensity if the flow is recorded close enough to the sea-land discontinuity.” (Antonia and Luxton, 1971; Antonia and Luxton, 1972)

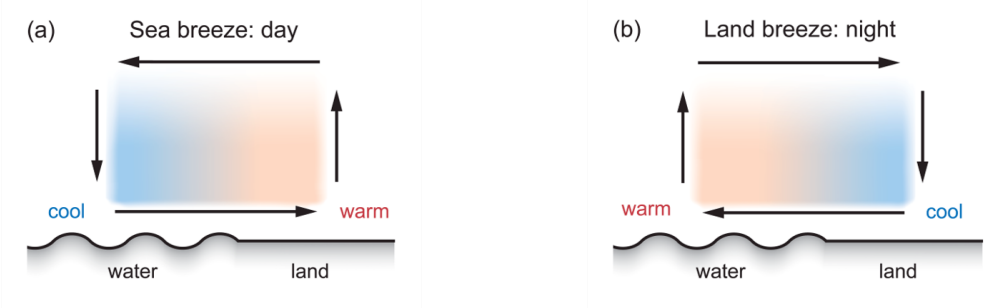

Figure 29: Schematics of sea breeze (Ahrens, 2011)

Thunderstorms Thunderstorms are small disturbances in horizontal extent but they are capable of generating severe winds (Holmes, 2015). The strongest winds resulting from thunderstorms are due to local convective effects and known as downbursts.
(Lombardo et al., 2014)

5.1.3 Atmospheric models

Reliable historical wind data are important in civil engineering. But often there are not sufficient measurements to make good estimates of the probability distribution necessary to make accurate calculations of design loads on the structures. A hindcast archive properly evaluated against reliable measurements represents a powerful proxy for long instrument time series. Furthermore, a hindcast archive is area-covering and as such will yield statistics for whole regions and locations not specifically planned in advance.

"Perhaps some day in the dim future it will be possible to advance the computations faster than the weather advances and at a cost less than the saving to mankind due to the information gained. But that is a dream." (Richardson, 1922)

Atmospheric models are complex mathematical algorithms derived from the fundamental laws of fluid dynamics and thermodynamics that are used for Numerical Weather Prediction (NWP). These equations are translated into computer code and use governing equations, numerical methods, parameterizations of other physical processes and combined with initial and boundary conditions before being run over a domain (geographic area). They produce meteorological information for future times at given locations and altitudes. Most models are designed to serve both atmospheric research and operational forecasting needs. Various models exist for each meteorological scale.

The models can either cover the entire Earth (Global Climate Models - GCM) or a limited area (Regional Climate Models - RCM, or Limited Area Models - LAM). Some of the most commonly used models are listed in Table 10.

The spatial and temporal resolutions used within the models determine how accurate physical processes can be modeled. Coarser global models capture synoptic scale weather systems while higher-resolution regional models capture mesoscale weather systems. The resolution is limited by the availability of super computing resources. However, higher resolution does not always reduce the forecast errors.

Atmospheric models require an estimate of the state of the atmosphere at the initialization time. Data assimilation is used for this purpose: a previous model forecast is compared with weather observations corresponding to the initialization time, and the model state is updated to reflect the observations. Observed weather data consist of surface observations, radiosondes and radar profilers, fixed and drifting buoys, ship and aircraft observations, satellite soundings, cloud and water vapor track winds, radar and satellite imagery. Initial conditions for regional

Table 10: Commonly used atmospheric models.

Model	Developed by
Global Climate Models	
GFS	NCEP
IFS	ECMWF
UM	UK Met Office
Regional Climate Models	
WRF (previously MM5)	NCAR
UM	UK Met Office
HIRLAM	HIRLAM consortium
HARMONIE/AROME (replacing HIRLAM)	HIRLAM consortium

models can be constructed (downscaled) from another analysis of a larger region.

Regional models also rely on data from a global model at their boundaries. This is obtained from a downscaling process. This approach allows using higher resolution only in regions of interest. Nesting is an alternative to downscaling, where the small higher resolution domain is embedded within the larger, lower-resolution domain. The coupling between the two domains can be one-way (information flows only from the large domain to the small domain) or two-ways.

The accuracy of the models is dependent on the quality of the initialization estimate which further depends on the methodology and the data being assimilated. The forecast quality is strongly influenced by the input at the boundaries. The forecast skill generally decreases with time and for longer term forecasts, where only the larger scales retain significant accuracy.

High-resolution regional models, such as the ones listed in Table 10, are capable of predicting gap wind flows if they have sufficient horizontal and vertical resolution and the initial and boundary conditions are being well handled. The number of grid points within the gap must allow the description of the atmospheric features of interest, in both horizontal and vertical directions. High-resolution models also appear to be quite capable in handling downslope windstorms and their interactions with gaps in mountain barriers.

Atmospheric models can be used for forecasting (prediction of future weather), for analysis (analysis of current weather), or for reanalysis (or hindcasting, re-run of the past). A reanalysis includes more observations in the data assimilation procedure than in forecasting, and it is therefore expected to simulate the weather state even more accurate than in a weather forecast. The most commonly used global atmospheric reanalyses are listed in Table 11. Although these global reanalyses represent the best available long-term global statistics, none of these fields can resolve mesoscale phenomena nor can they come close to modelling coastal wind conditions. The aim of downscaling a reanalysis is to resolve the interaction of large-scale flow with regional physiographic details in the high resolution forecast model and thus form realistic mesoscale features.

Table 11: Global atmospheric reanalysis.

Model	Performed by	Resolution	Range
ERA-40	ECMWF	125 km	1957-2002
NRA	NCEP/NCAR	210 km	1948-today
JRA-25	NCAR/UCAR	125 km	1979-2004

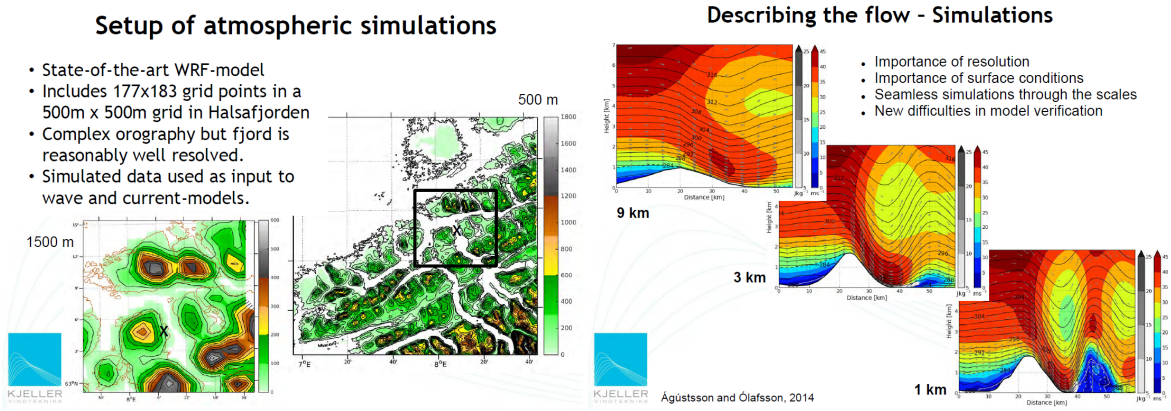

Figure 30: KVT - wind simulations

5.1.4 Wind measurements

Wind measurements can be obtained from two types of instrument: local sensors and remote sensors.

Local sensors, such as anemometers and wind vanes, record time series at their location. They must be mounted on a supportive structure. It is possible to mount local sensors on existing constructions, such as bridges or towers, but it is important that the selected supportive structure does not affect the flow at the measurement points. It is otherwise common to mount sensors on a met-mast. The location of the measurement point is then limited by the possibility to erect a met-mast at the desired location and by the height which can be reached by the met-mast. When well calibrated and mounted, local sensor have high accuracy. Icing of the sensor, which can occur in cold weather and can lead to measurement errors and loss of data, can be avoided by heating the sensors.

(a) Cup anemometer (b) Ultrasonic anemometer (c) Wind vane

Figure 31: Local wind sensors

Remote sensors, typically LiDARs, are placed on the ground and have a light beam which is oriented toward the location of interest (Figure 32). Measurements are limited to the along beam wind velocity in a serie of volumes along the line-of-sight of the LiDAR beam. LiDARs must therefore be placed wisely in order to measure relevant wind components. Pulsed wind lidar measure simultaneously the along beam wind velocity at several radial distances along the beam, while continuous wave lidars monitor the wind field at a single radial distance at a time. Both short-range and long-range LiDARs exist on the market, but the accuracy of the measurements tend to decrease with increasing distance from the LiDAR. LiDARs can easily be relocated or reoriented if required during the measurement period. Different scanning modes are available on LiDARs with rotating head:

- Doppler Beam Swinging mode (DBS) for wind profile monitoring,
- Plan Position Indicator mode (PPI) for scans over an azimuth sector at a fixed elevation,
- Range Height Indicator mode (RHI) for measurements at a fixed azimuth and varying elevation, and
- Sequential Fixed Line of Sight mode (LOS) for measurements along a single line.

Several LiDARs can also be used in combination: the measurements obtained at the crossing of their beams then contain information about several wind components.

Wind masts represent a more reliable and known measurement technology, but fail to capture coherency and local variation along such long bridges (Johansen, 2016).

A measurement system will generally be composed of several met-masts equipped of anemometers and wind vanes at various heights for long-term monitoring as well as one or more LiDARs for monitoring over shorter periods. Since surface winds vary strongly with ground roughness and obstacles, one of the major issue when designing a measurement system is the representativeness of the flow.

(DNV, 2007) - When the wind climate at a location cannot be documented by site-specific measurements, the distribution of U_0 can still, usually, be represented well, for example on the basis of wind speed measurements from adjacent locations. However, the distribution of σ_U will usually be harder to obtain, because it will be very dependent on the particular local roughness conditions, and it can thus not necessarily be inferred from known wind speed conditions at adjacent locations. At a location where wind speed measurements are not available, the

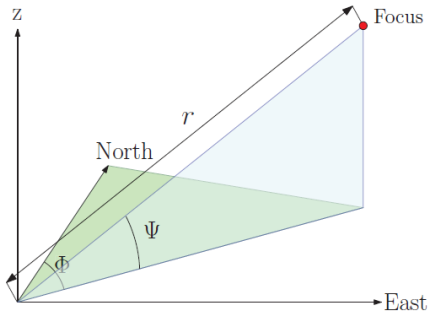

Figure 32: Azimuth angle Φ, elevation angle ψ and radial distance r defined for a scanning wind lidar (image from (Cheynet, 2016)).

determination of the distribution of the standard deviation σ_U of the wind speed is therefore often encumbered with ambiguity. It is common practice to account for this ambiguity by using conservatively high values for σ_U for design purposes.

(Cheynet, 2016) - Because flow properties studied along the bridge deck do not necessarily corresponds to cross-flow separations, the cross-flow turbulence length scales are also presented based on the wind component V_x instead of U.

(Cheynet et al., 2016a) - For the single-point statistics, results are also presented in the wind-based coordinate system, to provide data comparable to those in the literature. This applies to the wind spectra, the integral length scales and the turbulence intensity.

(Cheynet et al., 2017b) - The along-beam wind coherence estimated using a single pulsed lidar is only of limited relevance for estimating wind loading on a long-span bridge, the response of which is governed by the lateral coherence of turbulence. (for both the along wind component and the vertical wind component) The estimation of the lateral coherence of the vertical wind component using synchronized wind lidars is, on the other hand, considerably more challenging because of the need to use relatively large elevation angles to properly observe the vertical wind velocity component.

(Cheynet et al., 2016c) - Wind coherence measurement by a single pulsed Doppler wind lidar (FINO1)

(Cheynet et al., 2017a) - Spectral characteristics of surface-layer turbulence in the North Sea

(Cheynet et al., 2016b) - The WindScanners are observed to slightly overestimate the integral length scales, which could not be explained by the laser beam averaging effect alone. On the other hand, the spatial averaging effect does not seem to have any significant effect on the coherence.

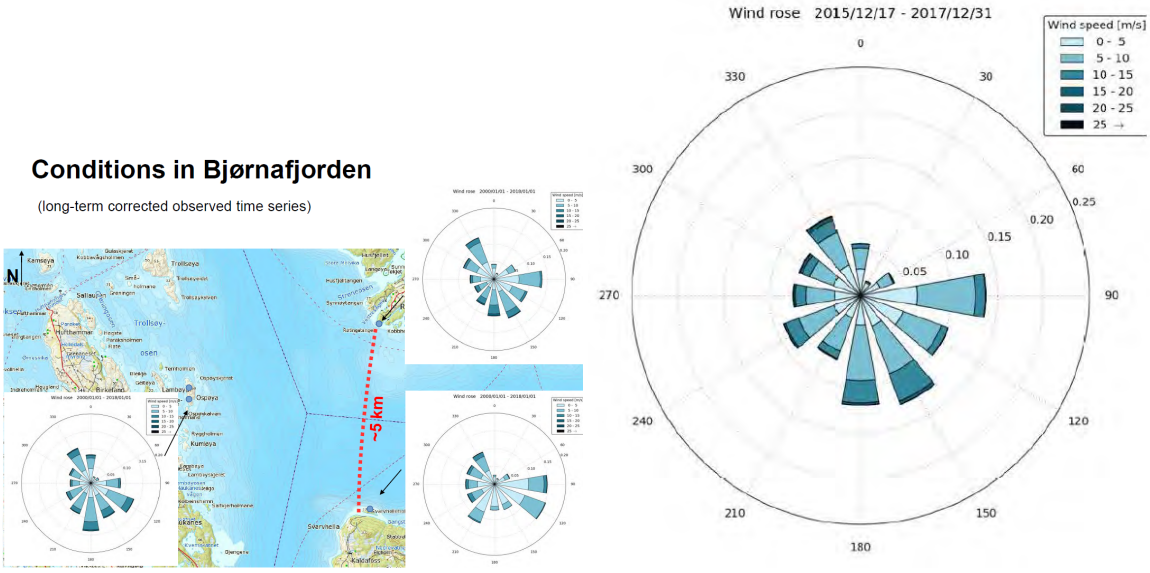

(a) 2000-17 (b) 2016-17

Figure 33: Mean wind speed wind rose recorded at 10 m height at Ospøya met mast (Bjørnafjord) obtained from different recording periods.

5.2 Wind characterisation

5.2.1 Long-term statistics

The long-term wind statistics at the location of the structure shall be established on the basis of previous measurements at the actual location and adjacent locations, hindcast wind data as well as theoretical models and other meteorological information (DNV, 2007). The long-term probability distributions can generally be fitted for the mean wind speed U_0 to a Weibull distribution and for the standard deviation σ_U a lognormal distribution. The return period R_p is defined as the average number of years between rare events. The mean wind speed U_0 with return period R_p is the mean wind speed U_0 whose probability of exceedance in one year is $1/R_p$.

Figure 33 shows the mean wind speed wind roses obtained at a met-mast for a 2 years vs a 17 years period, showing the importance of having longer recording periods.

5.2.2 Short-term statistics

Stationary wind field is achieved under stationary and homogeneous conditions. In addition, we will consider here that the atmospheric stability is neutral. Under those assumptions, defined in Section 5.2.2, several models have been developed for the short-term statistics of the stationary wind. The most commonly used models for short-term statistics are listed and shortly described in Section 5.2.2. Reference is also made to the Standards listed in Section 3. Characterization of the short-term statistics of the wind field at a location of interest is typically done by means of field measurements. The instruments used for this purpose are described in Section 5.1.4. Once characterized, a time series of the stationary wind can be reconstructed using turbulent wind field generators which are described in Section 5.2.3.

Assumptions Stationary and homogeneous conditions are achieved if the selected time-space-window is short and small enough to render sufficiently constant statistical properties.

The stationary condition can be assessed using the reverse arrangement (RA) test from (Bendat and Piersol, 2011). According to (Bendat and Piersol, 2011), the RA test is a "non-parametric and distribution-free procedure where no assumption is made concerning the probability distribution of the data being evaluated" used to detect non-negligible trends in random data set. Although the RA test is recognized as efficient, its performance has not been assessed in details for wind records (Cheynet, 2016). Applying this test on large data set may be limited by the heavy computational cost when a large amount of samples have to be tested.

Homogeneous conditions is generally achieved when terrain conditions are not complex, i.e. the upstream distance with uniform terrain roughness is long enough to stabilize the profile sufficiently. As long as the hypothesis on flow homogeneity is respected, the wind statistics can be representative in the whole area of interest.

In wind engineering, the space window is typically of the size of the structure which is usually small enough to render homogeneous conditions. The time window is typically set to a period of 10 minutes. However, for very large structures, the typical dimensions and the natural frequencies may result in non-stationary and non-homogeneous conditions, making the traditional statistical tools inappropriate to describe wind turbulence since the increase of the sample duration may unfortunately be associated with non-stationary fluctuations. As pointed out by (Chen et al., 2007) and (Wang et al., 2013) a non-stationary flow can for example result in an unusually large turbulence intensity.

Atmospheric stability is related to the vertical temperature gradient in the atmosphere. Despite having strong consequences on mean wind shear and turbulence, the statistical models for stationary wind generally assumes neutral stability, i.e, the temperature decrease with increasing altitude neither aids nor hinders large-scale vertical motion. More about atmospheric stability can be read in Section 5.1.

Definition 5.1: Wind Velocity Vector

The wind velocity vector $\mathbf{U}(\mathbf{t})$ is split in three fluctuating orthogonal components: $U(t)$ in the main flow along-wind direction, and $V(t)$ and $W(t)$ in the across wind horizontal and vertical directions.

$$\mathbf{U}(\mathbf{t}) = \begin{bmatrix} U(t) \\ V(t) \\ W(t) \end{bmatrix} = \begin{bmatrix} \overline{U} \\ 0 \\ 0 \end{bmatrix} + \begin{bmatrix} u(t) \\ v(t) \\ w(t) \end{bmatrix} \tag{7}$$

$\overline{U}$ is the commonly known mean wind velocity, and $u(t)$, $v(t)$ and $w(t)$ are the turbulence components.

Statistical analysis of the turbulence components $u(t)$, $v(t)$ and $w(t)$ will render three individual zero mean Gaussian probability density distributions with variances σ_u^2, σ_v^2 and σ_w^2 that depend among others on the mean wind velocity and the upstream terrain roughness.

The mean wind velocity $\overline{U}$ varies with the height above the ground or sea surface. Theoretical expressions such as the logarithmic profile (Eq. 8), the power law profile (Eq. 9) or the Frøya profile (Eq. 10) are commonly used to describe the vertical profile of the mean wind velocity. The Frøya profile (Andersen and Løvseth, 2006) is a special case of the logarithmic profile. It is the best documented wind speed profile for offshore locations and maritime conditions.

$$\overline{U}(z) = U_0 k_T \ln\left(\frac{z}{z_0}\right) \tag{8}$$

$$\overline{U}(z) = U_0 \left(\frac{z}{z_{ref}}\right)^{\alpha} \tag{9}$$

$$\overline{U}(t,z) = U_0 \left(1 + C \ln\left(\frac{z}{z_{ref}}\right)\right)\left(1 - 0.41 I_u(z) \ln\left(\frac{t}{t_0}\right)\right) \tag{10}$$

where k_T, z_0, z_{min} and α are parameters characteristic to the terrain roughness (Table 12), and U_0 is the mean wind velocity at the reference height, t is the averaging time period. A commonly used reference height is z_{ref} = 10 m, but the height of the structure of interest is a better reference height if wind data are available at that height. When wind speed data for the desired reference height are not available, it can be extrapolated from one of the wind speed profiles.

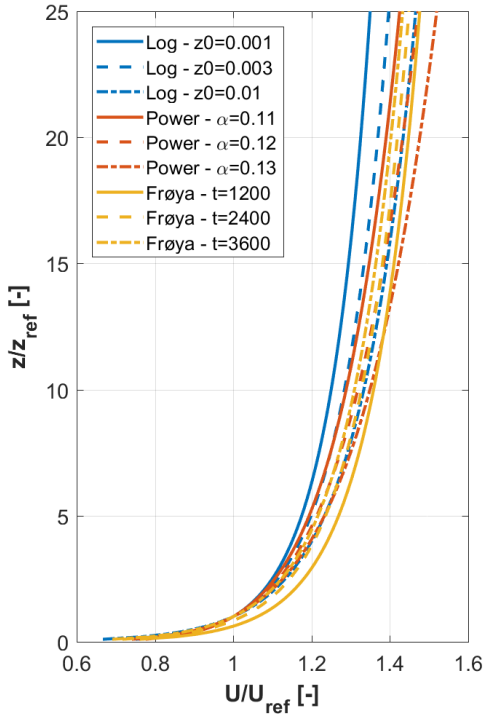

Figure 34: Vertical velocity profile. Comparison of three models with different input parameters

Over water, the wind surface drag yields to deformation of the water surface, thus creating wind-induced waves. This implies that the roughness parameters over bodies of water strongly depend on the reference wind velocity U_0 (Andersen and Løvseth, 2006). The Charnock relation is expressing this dependence (Astrup and Larsen, 1999).

Table 13 summarizes the Standards recommendations for the mean wind velocity profiles. The Eurocode EN1991 recommend using the logarithmic profile combination with a series of site specific factors, including an orography factor $C_o(z)$ which takes into account topographical effects. However, the orography factor is not defined for valleys where gap effects is to be expected, such as fjords surrounded by mountainous areas with steep slopes.

Definition 5.2: Turbulence intensity

The turbulence intensities are defined by

$$I_i(z) = \frac{\sigma_i(z)}{\overline{U}(z)} \tag{11}$$

where i = u, v, w refers to the three turbulence components.

Table 12: Terrain roughness parameters (DNV, 2007)

Table 2-1 Terrain roughness parameter z_0 and power-law exponent α		
Terrain type	Roughness parameter z_0 (m)	Power-law exponent α
Plane ice	0.00001-0.0001	
Open sea without waves	0.0001	
Open sea with waves	0.0001-0.01	0.12
Coastal areas with onshore wind	0.001-0.01	
Snow surface	0.001-0.006	
Open country without significant buildings and vegetation	0.01	
Mown grass	0.01	
Fallow field	0.02-0.03	
Long grass, rocky ground	0.05	
Cultivated land with scattered buildings	0.05	0.16
Pasture land	0.2	
Forests and suburbs	0.3	0.30
City centres	1-10	0.40

Table 2-1 is based on Panofsky and Dutton (1984), Simiu and Scanlan (1978), JCSS (2001) and Dyrbye and Hansen (1997).

Table 13: Mean wind velocity profile - Standards recommendations.

Standard	**Model**
Eurocode EN1991-1-4	Log profile combined with site specific factors
Håndbok N400 Bruprosjektering	Refers to Eurocode EN1991-1-4
NORSOK N003	Frøya profile
IEC 61400-1	Power law profile
DNV-RP-C205	Mentions the three models

Under isotropic conditions, the turbulence intensities are of approximately same magnitude in the three directions $I_u \approx I_v \approx I_w$. However, up to a height of about 200 m in the atmosphere over homogeneous terrain, it is generally assumed that

$$\begin{bmatrix} I_v \\ I_w \end{bmatrix} = \begin{bmatrix} 0.75 \\ 0.5 \end{bmatrix} \cdot I_u \tag{12}$$

Solari and Piccardo (Solari and Piccardo, 2001) reviewed more than 40 studies dealing with the measurement of these ratios. They found out that the ratio I_v/I_u fluctuates between 0.71 and 0.88, whereas I_w/I_u is bounded between 0.45 and 0.6. In a more recent study, (Holmes, 2015) found that the ratio I_v/I_u and I_w/I_u for flat terrains are about 0.88 and 0.55 respectively, which falls within the above mentioned bounds.

For flat and homogeneous terrain and neutral atmospheric stability, turbulence intensity is known to be high at low wind velocities and to decrease when the mean wind speed increases. When the mean wind velocity reaches a threshold value, the turbulence intensity remains more or less constant (Cheynet, 2016).

For complex terrain, the wind speed field will be much more isotropic, and values for I_v and I_w very near the value of I_u can be expected (DNV, 2007).

Definition 5.3: Covariance

The (cross-)covariance $\mathrm{Cov_{ij}}$ is a time domain statistical property that provides information about possible relationships between two zero mean variables obtained from simultaneous two point recordings with an arbitrary separation Δs and a time lag τ that can take any value within the duration of the recording.

$$\mathrm{Cov_{ij}}(\Delta s, \tau) = E\left[i(s,t) \cdot j(s+\Delta s, t+\tau)\right] \tag{13}$$

where i,j = u, v, w refers to the three turbulence components.

The **auto-covariance** function $\mathrm{Cov_i}(\tau)$ corresponds to the study of a single variable recording at a given location ($\Delta s = 0$).

The covariance between two turbulence recordings results in a three by three matrix.

$$\mathbf{Cov}(\Delta s, \tau) = \begin{bmatrix} \mathrm{Cov_{uu}} & \mathrm{Cov_{uv}} & \mathrm{Cov_{uw}} \\ \mathrm{Cov_{vu}} & \mathrm{Cov_{vv}} & \mathrm{Cov_{vw}} \\ \mathrm{Cov_{wu}} & \mathrm{Cov_{wv}} & \mathrm{Cov_{ww}} \end{bmatrix} \tag{14}$$

where all the covariance functions $\mathrm{Cov_{ij}}(\Delta s, \tau)$ may contain separation in an arbitrary direction $s = x, y$ or z.

It is an usual assumption that covariance between two different turbulence component may be neglected and all off-diagonal terms in Eq. 14 then become zero. Covariance properties in the wind field are generally decaying with increasing separation Δs and time lag τ.

Definition 5.4: Integral length scales

The integral length scales of the wind velocity components are calculated based on the integration of the normalized auto-covariance:

$$L_i = \overline{U} \int_0^\infty \frac{\mathrm{Cov_i}(\tau)}{\sigma_i^2} d\tau \tag{15}$$

where i = u, v, w refers to the three turbulence components.

The integral length scales can be interpreted as the average eddy size of turbulence components in the direction of the main flow. Eq. 15 shows a high sensitivity to non-stationary fluctuation of the sample selected for calculation (Cheynet, 2016), which can lead to over-estimations of the integral length scales.

Definition 5.5: Spectral density

The zero mean variable $x(t)$ may be approximated by a sum of harmonic components $X_k(\omega_k, t) = c_k \cdot \cos(\omega_t t + \phi_k)$, where c_k are the amplitudes and ϕ_k the phase angles of the harmonic components.

The **(cross-)spectral density** S_{ij} is a frequency domain property that provides information about the variance density distribution in the frequency domain.

$$\mathrm{S_{ij}}(\pm\omega_k) = \frac{E\left[X_k^* \cdot Y_k\right]}{\Delta\omega} \tag{16}$$

The spectral density is in general a complex quantity and its real part is referred to as the **co-spectral**

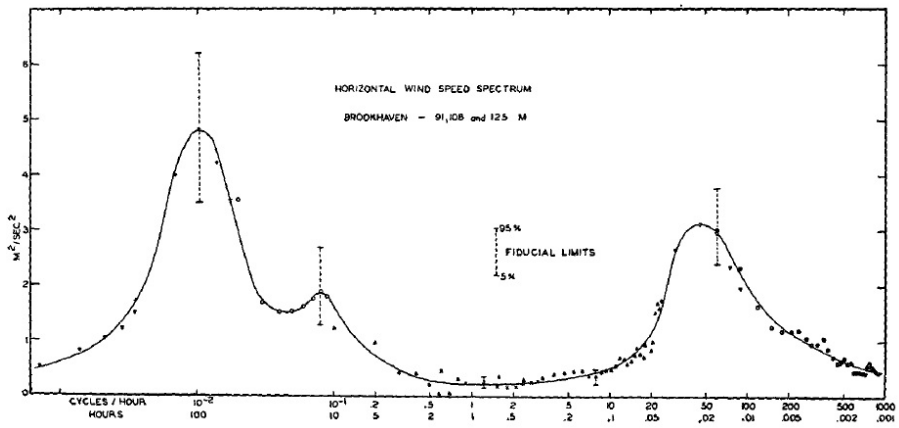

Figure 35: Horizontal wind-speed spectrum at Brookhaven National Laboratory at about 100m height (Van der Hoven, 1957).

density $\mathrm{Co_{ij}}(\Delta s, f)$.

$$\mathrm{Co_{ij}}(\Delta s, f) = Re\left[S_{ij}(\Delta s, f)\right] \tag{17}$$

The **normalized co-spectrum** is obtained from

$$\widehat{\mathrm{Co_{ii}}}(\Delta s, f) = \frac{Re\left[S_{ii}(\Delta s, f)\right]}{S_i(f)} \tag{18}$$

where $S_i(f)$ is the auto-spectral density (Definition 5.6).

The spectral density is a function that describes the correspondence between the local wind velocities at two points separated by a given distance. The larger is the distance, the lower will be the correspondence. Low-frequency wind will have higher correlation than high frequency wind.

Definition 5.6: Auto spectral density

The **auto spectral density** S_x is defined as

$$\mathrm{S_i}(\pm\omega_k) = \frac{E\left[X_k^2\right]}{\Delta\omega} = \frac{\sigma_{i_k}^2}{\Delta\omega} \tag{19}$$

where i = u, v, w refers to the three turbulence components.

The auto spectral density is a function of U_0 and σ_u and expresses how the energy of the wind speed in a specific point in space is distributed between various frequencies (DNV, 2007). In (Van der Hoven, 1957), a power-spectrum analysis of horizontal wind speed was made over a wide range of frequencies. The resulting spectrum, shown in Figure 35, presents two major eddy-energy peaks; one peak occurs at a period of about 4 days, and a second peak occurs at a period of about 1 minute. Between the two peaks, a broad spectral gap is centered at a frequency ranging from 1 to 10 cycles per hour. The spectral gap seems to exist under varying terrain and synoptic conditions.

The frequency range of interest in engineering applications is defined by the natural frequencies of the structure of interest, generally corresponding to scales ranging from seconds to minutes. Several models exist to represent the spectral density of the wind speed in this frequency range. They generally agree in the high frequency range, whereas large differences exist in the low frequency range.

Most available model spectra are calibrated to wind data obtained over homogeneous land. Only a few are calibrated to wind data obtained over water. Among others, (Ochi et al., 1988) has shown that wind spectra measured offshore often contain more energy at low frequencies compared to the wind spectra measured onshore. This is partly due to the fact that, in an offshore environment, the size of eddies is not limited by topographical changes (Cheynet et al., 2017b).

Model spectra are often expressed in terms of 10 minutes mean wind speed U_{10}, integral length scale Lu, standard deviation σ_U, and friction velocity u_* of the wind speed process, which are all highly dependent on the upstream terrain topography and roughness. These quantities, which are vital for the dimensional spectrum which is the quantity of interest for engineering applications, varies somewhat from one calibration study to another. The study of (Wang et al., 2017a) illustrates well this point: the normalized wind spectrum from N400 Handbook and three different terrain categories are used to compute the bridge response in Lysefjord. Results are compared with full scale measurements that show very different trends for winds from NE and SW. The simulation results for three terrain categories generally lay in between the two measured curves. Terrain category 4 matches well one of the wind direction while category 2 matches the opposite wind direction, showing the importance to consider the terrain category of the upstream fetch for each wind direction of interest.

The **von Kármán spectrum** (Von Karman, 1948) was developed based on wind tunnel measurements under the assumption of homogeneous isotropic turbulence. (Morfiadakis et al., 1996) compared wind measurements performed on an island with the von Kármán spectrum. The analysis shows that the von Kármán spectrum is suitable in free stream conditions but that it does not capture effects due to topography such as flow separation.

The **Davenport spectrum** (Davenport, 1961) was developed in the context of determining the response of a simple structure to a turbulent, gusty wind through a statistical approach. It expresses the spectral density near the ground by taking into account its variation with mean wind velocity, roughness of the terrain, and the height above ground level. The Davenport spectrum is originally developed for wind over land.

The **Kaimal wind spectrum** (Kaimal et al., 1972) is an empirical formulation developed based on on land measurements. It is derived for neutral atmospheric conditions.

The **Harris spectrum** (Harris, 1990), originally developed for wind over land, is an alternative to the von Karman spectrum that provides corrections enabling measured data to be fitted. It expresses the spectral density in terms of U_0 irrespective of the elevation. The integral length scale L_i is in the range 60-400 m with a mean value of 180 m.

The **Simiu & Scanlan spectrum** (Simiu and Scanlan, 1996) is developed taking into account the wind energy over a seaway in the low frequency range. The magnitude of the integral length scale L_i typically ranges from 100 to 240 m for winds at 20-60 m above the sea surface. It is one of the recommended spectrum by (DNV, 2007) for design of offshore structures.

The **Ochi & Shin spectrum** (Ochi et al., 1988) is developed from measured spectra over a seaway. It has not been calibrated to measured data for frequencies less than approximately 0.001 Hz but merely been assigned an idealized simple function. It is one of the recommended spectrum by (DNV, 2007) for design of offshore structures.

The **Frøya spectrum** proposed by Andersen and Løvseth ((Andersen and Løvseth, 1995),(Andersen and Løvseth, 2006),(Andersen and Løvseth, 2010)) is originally developed for neutral conditions over water in the Norwegian Sea. The Frøya spectrum is established based on measurements made over the ocean (on Sletringen island (Frøya municipality) at the Norwegian coast) at high latitudes (northwards from, say, 40–451N; North Atlantic, North Sea) during the passage of large-scale low-pressure systems. At lower latitudes important characteristics of the weather phenomena are different. The Frøya spectrum is a generalization of the Harris and Kaimal spectra with attention given to the low-frequency range while keeping the correct high-frequency asymptote. Allowance is made for that the total energy and the characteristic frequency entering the argument may be expressed in powers of U_{ref} and z. A frequency of 1/2400 Hz defines the lower bound for the range of ap-

plication of the Frøya spectrum. It is one of the recommended spectrum by (DNV, 2007) for design of offshore structures, especially in regimes where stability effects are not important and for situations where excitation in the low-frequency range is of importance. It is also the spectrum recommended in the NORSOK Standard.

Whenever it is important to estimate the energy in the low frequency range of the wind spectrum over water, it is recommended to use the Frøya or Ochi & Shin spectra which have more energy content in the low frequency range (f < 0.01 Hz) than the Davenport, Kaimal and Harris spectra which are spectral models traditionally used to represent wind over land. Yet, for frequencies less than approximately 0.001 Hz, the Ochi & Shin spectrum has less energy content than the Frøya spectrum.

Table 14: Wind spectrum - Standards recommendations.

Standard	**Model**
Eurocode EN1991-1-4:2005 Annex B	Kaimal
Håndbok N400 Bruprosjektering	Kaimal
NORSOK N003	low frequencies: Frøya / high frequencies: Harris
IEC 61400-1	Mann / Kaimal
DNV-RP-C205	Mentions several models

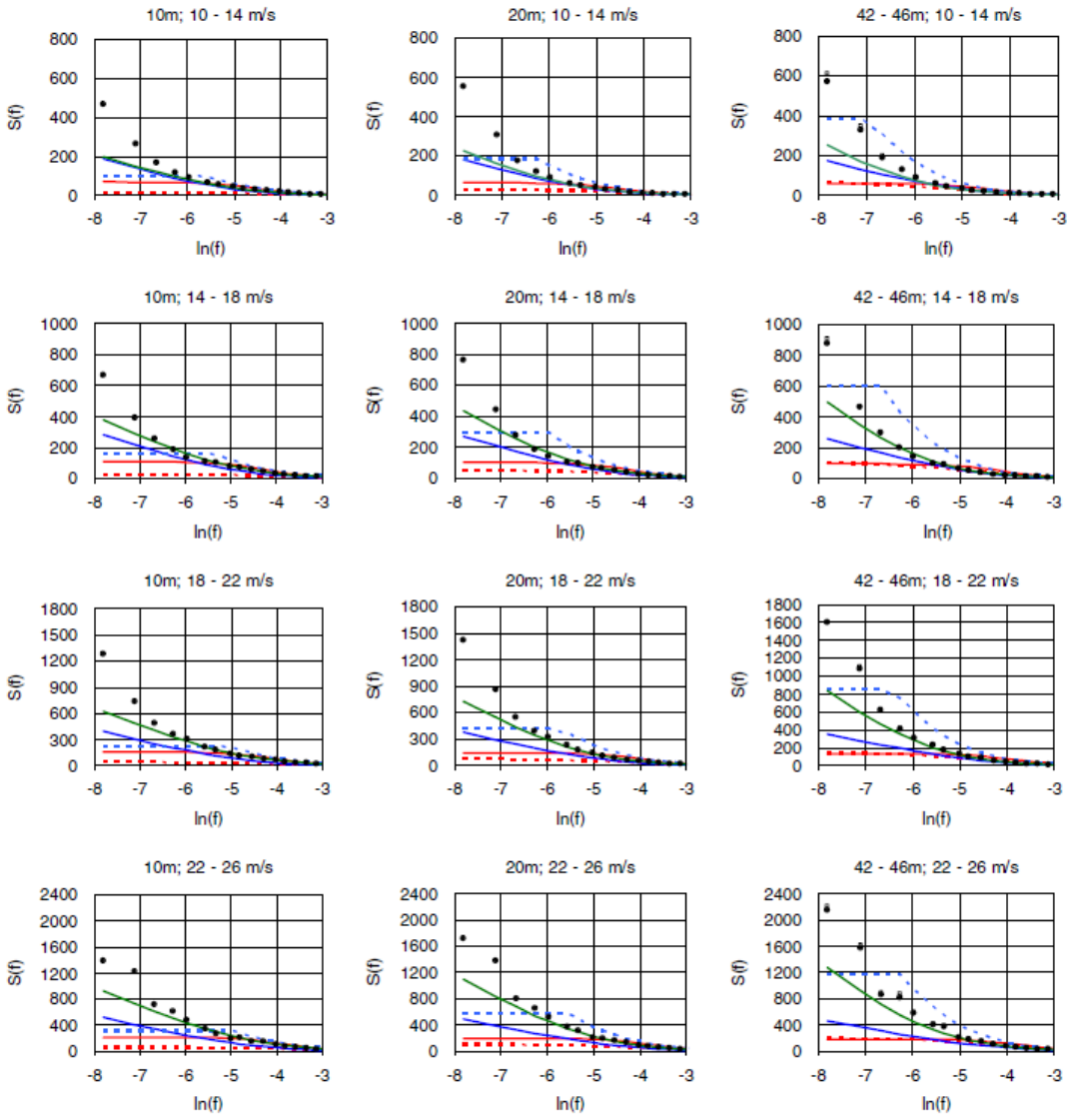

Figure 36: (Andersen and Løvseth, 2006) Spectral energy density S(f) (unit: (m/s)2/Hz) versus ln (f) in the period range 20 s–40 min (ln (0.01 Hz) =-4.6) for various reference wind speeds and heights according to measurements (circles, neutral data at Sletringen) and five models: Harris spectrum (solid red, Eq. (4a)), Kaimal spectrum (dashed red, Eq. (4b)), Wills (solid blue, Eq. (4c)), Ochi (dashed blue, Eq. (4d)) and Frøya spectrum (green, Eq. (4f)). Note that the model values represent the centre of the wind speed ranges.

Definition 5.7: Coherence

The coherence is the normalized cross-spectral density of the wind velocity fluctuations measured in two different positions. It is a frequency domain statistical property that provides information about possible relationships between two zero mean variables obtained from simultaneous two point recordings with an arbitrary separation Δs. The coherence function is defined by:

$$\mathrm{Coh_{ij}}(\omega) = \frac{|S_{ij}|^2}{S_{ii}S_{jj}(f)} \tag{20}$$

where S_{ii} and S_{jj} are one sided power spectral density functions of i and j at frequency f and S_{ij} is the one-sided complex valued cross-power spectral density function between the two processes.

In atmospheric wind, coherence has been used since the 1960s to take into account the spatial correlation of the wind gusts (Davenport, 1961). According to (Kristensen and Jensen, 1979), there are only four different types of non-zero velocity coherence. These four coherences correspond to the combinations uu, vv, ww, and uw. For each of those combinations, the coherence can be expressed in terms of longitudinal, lateral and vertical separation as a function of frequency.Should $Coh_{uv}(f) = 1$ then $u = v$ in that band of frequencies, meaning that in that band of frequencies, v would be perfectly calculable (predictable) from u.

The following observations (based on (Ropelewski et al., 1973), (Kristensen and Jensen, 1979), (Saranyasoontorn et al., 2004) and (Cheynet et al., 2017b)) can be made about coherence of wind in homogeneous terrain:

- Coherence in all three turbulence components decreases with increased separation at all frequencies.
- (Ropelewski et al., 1973) For **longitudinal** separations, the cross-stream decay parameter is a strong function of stability, and the streamwise decay parameter is not, over the range of stabilities analyzed (given by the Richardson number). Both depend strongly on roughness. For **lateral** separations, decay parameters for both wind components should be functions of the stability but not roughness.
  -> If the wind load on the bridge are studied only for wind perpendicular to the bridge, then the coherence along the bridge should not depend on the terrain roughness, only on the stability of the atmosphere.
- For **lateral** separations, as illustrated in Figures 37-39, the across-wind (v) turbulence component is more coherent than the along-wind (u) and vertical (w) components. Comparing the uu- and ww-coherence, it is seen that the uu-coherence is larger than the ww-coherence in the low frequency range but lower at high frequencies. For a large lateral separations dy, the ratio dy/L (where L is a typical length scale of the turbulence) cannot be considered small and the coherence becomes less than unity at zero frequency.
- For **vertical** separations (illustrations available in (Saranyasoontorn et al., 2004)), the vertical turbulence component appears to be the most coherent followed by the acrosswind and along-wind components.
- Estimated cross-coherence between the along-wind and across-wind turbulence components as well as between the across-wind and vertical components (uv and vw) are far less significant than that between the along-wind and vertical turbulence components (uw).

(Cheynet et al., 2017b) studied the wind coherence in complex terrain. It was found that in the studied fjord, the coherence becomes weak at separations larger than 40 m.

Several models exist for coherence of atmospheric wind. (Cheynet et al., 2017b) - it is uncertain whether a spectral wind model developed for an offshore or an onshore environment should be used in the middle of a wide fjord within a coastal area.

The **von Kármán coherence function** (Von Karman, 1948) is based on assumptions of flow homogeneity, isotropy of turbulence and Taylor's frozen turbulence hypothesis. It predicts correctly the *relative* coherence levels of the along-wind, across-wind, and vertical turbulence components. The isotropy assumption however results in zero coherence for all cross-coherences, which is not true. It also fails for vertical separation for the

same reason.

The **Davenport coherence function** (Davenport, 1961) is a simple and commonly used coherence function. It is originally developped for along-wind turbulence component with vertical separation. The assumption that the coherence spectrum approaches unity at zero frequency is inconsistent with observed coherence spectra for the across-wind and vertical turbulence components. Hence, extending the Davenport coherence model hypotheses for use with these turbulence components is not appropriate. The use of a function that is positive for any separation leads to a finite integral over a plane transverse to the wind in conflict with the definition of u as a zero mean fluctuation component.

The **Bowen coherence model** (Bowen et al., 1983) suggests that the coherence depends on the measurement height z and d_y^2, which is not predicted by the Davenport coherence model. To estimate the wind load on a suspension bridge, the measurements should, therefore, be conducted at the deck height. Because the Bowen coherence model was designed at an altitude lower than 20 m, it is uncertain beyond which height such a model ceases to be valid.

The **Krenk coherence model** (Krenk, 1996) respects the mean value consistency by including a suitable derivative, and correlation of the low frequency components is limited by replacing the wave number by a modified wave number with finite value at zero frequency.

The **Solari coherence model** (Solari, 1987) is a more general spatial coherence model that was developed with strong focus on correct evaluation of the actions of wind on constructions such as buildings, towers and chimneys. This model is implemented in the newest TurbSim and enables the user to implement a large variation of the different coherence values measured.

The **Thresher et al. coherence model** (Thresher et al., 1981) is an empirical model which present an additional term that allows for reduction in coherence with increase in separation. It is the coherence model recommended by the IEC standards.

The **Cheynet coherence model** (Cheynet, 2016) suggests a four parameters exponential decay function. The four-parameter coherence function presented in Eq. 21 is more general than the empirical coherence models presented previously.

$$\gamma(d_y, f) = exp\left(-\left[\frac{d_y}{V_x}\sqrt{(c_1 f)^2 + c_2^2}\right]^{c_3}\right) \cdot cos\left(c_4 \frac{d_y f}{V_x}\right) \tag{21}$$

The first parameter c_1 gives the slope of the exponential decay, the second one c_2 allows the co-coherence to be lower than one for a zero frequency. The third one c_3 allows an additional inflection point at low frequencies, and the last one c_4 allows the co-coherence to become negative when the frequency increases. The value of c_4 is expected to be very close to 2π if Taylor's frozen turbulence hypothesis is applicable. For a perfectly frozen turbulent field, the decay coefficient c_1 should be equal to 0. Other coherence models can be recovered from this formulation by setting some of the four parameters to either 0 or 1.

The **Mann uniform shear coherence model** (Mann, 1998) is a more complex model that is based on a spectral velocity tensor. It is the one that is recommended by the standard. In (Saranyasoontorn et al., 2004), the Mann model appears to agree reasonably well with the estimated coherence spectra from data for all three turbulence components although it underestimates the along-wind coherence for small lateral separations. In particular, the Mann model predicts low frequency coherence better than other models studied, and the model does especially well compared to the von Kármán model for across-wind and vertical coherence predictions. The Mann model generally overpredicted the cross-coherence between the along-wind and vertical turbulence components.

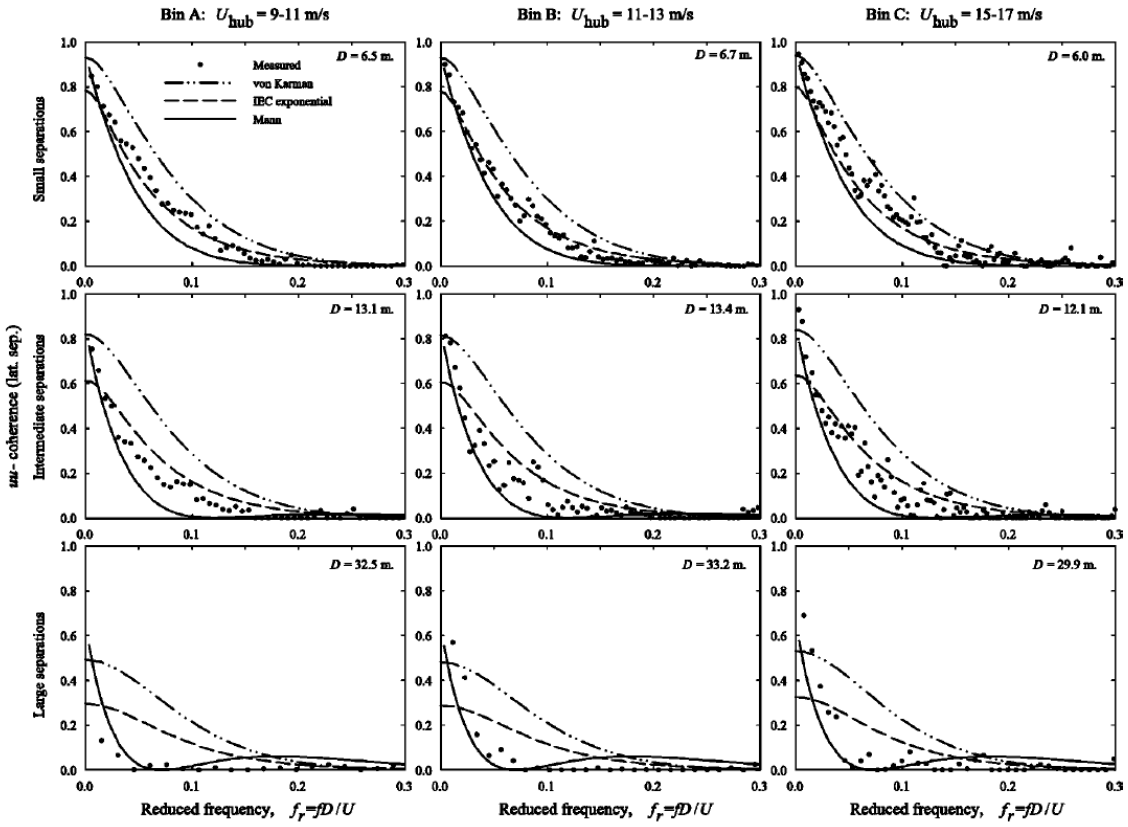

Figure 37: (Saranyasoontorn et al., 2004) Comparison of the estimated uu-coherence spectra for lateral separations with the IEC modified exponential (a=8.8, b=0.12, L_c=56 m), the von Kármán (L=56 m), and the Mann (s=3.9, l=14 m) models

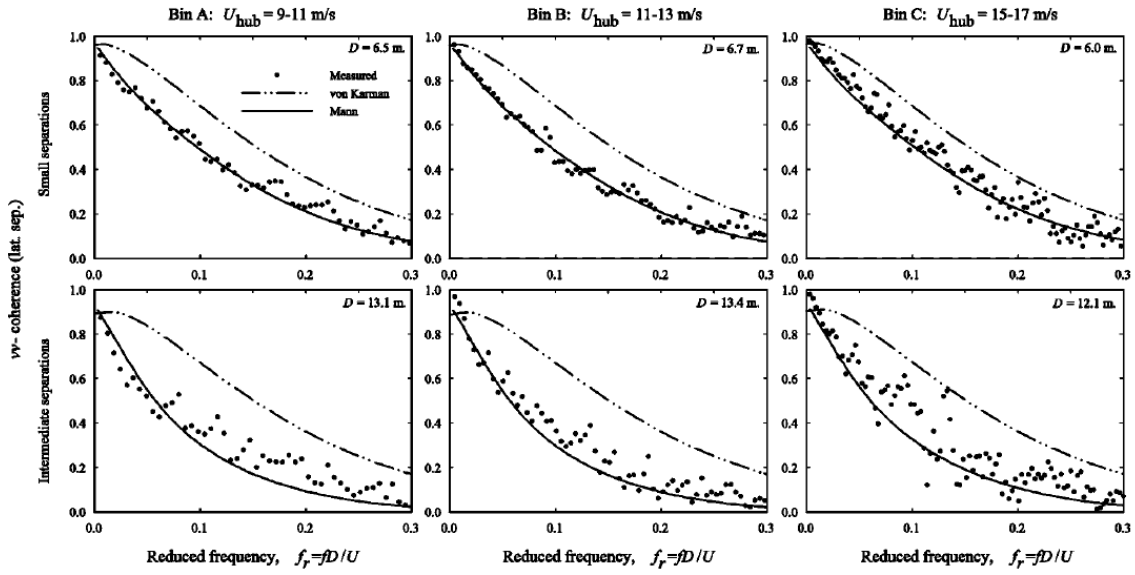

Figure 38: (Saranyasoontorn et al., 2004) Comparison of the estimated vv-coherence spectra for lateral separations with the von Kármán (L=56 m) and the Mann (s=3.9, l=14 m) models

Table 15: Coherence - Standards recommendations.

Standard	Model
Eurocode EN1991-1-4	not mentioned
Håndbok N400 Bruprosjektering	Davenport
NORSOK N003	Frøya
IEC 61400-1	Mann / Exponential coherence model ($c4 = 0$)
DNV-RP-C205	Mentions several models

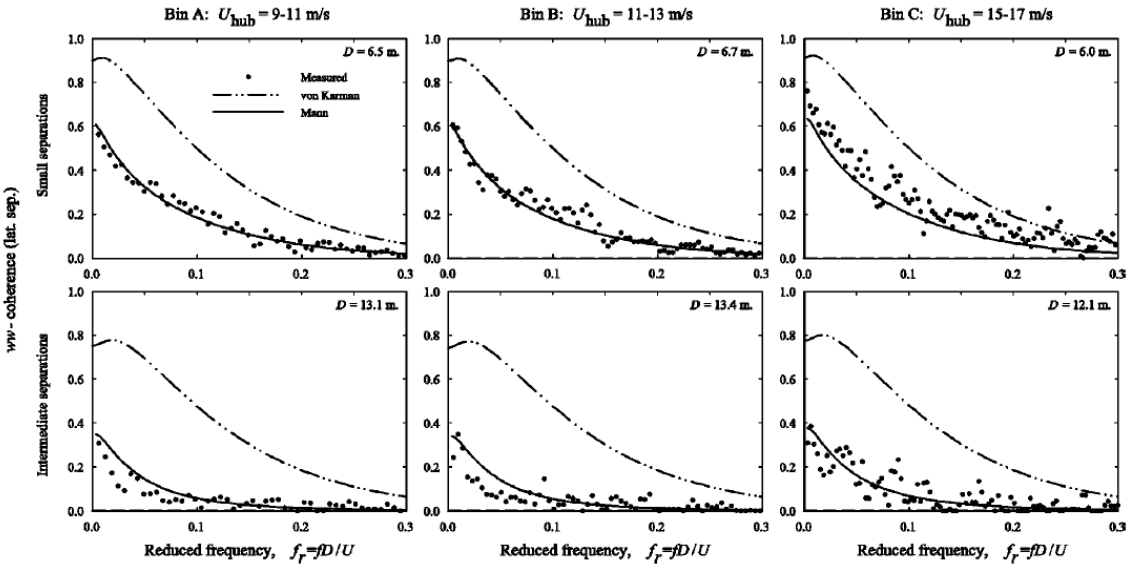

Figure 39: (Saranyasoontorn et al., 2004) Comparison of the estimated ww-coherence spectra for lateral separations with the von Kármán (L=56 m) and the Mann (s=3.9, l=14 m) models

5.2.3 Stationary wind field reconstruction

The turbulent wind field has been described in previous subsections with regards to measurements, simulations and standards. In order to utilize this information in numerical models or in experimental test, the input wind needs to be generated. One option is to use CFD, but the computational cost is high, and here we will limit the discussion to existing tools that can generate numerical wind field within a reasonable time.

TurbSim and WindSim TurbSim and WindSim are very similar in how they generate the wind field. TurbSim is a stochastic, full-field, turbulent-wind simulator developed at the National Renewable Energy Laboratory (NREL) (Jonkman, 2009). It is an open source code written in Fortran programming language. There are two versions of TurbSim that should be considered; v.1.06.00 which is an official release and the Alpha version (June 2016). The alpha version has not been officially released and lacks proper documentation, but contains some additional features. WindSim is developed by Aas-Jakobsen, and both programs are originally developed for use on wind turbines.

Tables 16 and 17 lists the different mean wind profiles and wind spectra that are included in the two programs. This is not an extensive list of the mean vertical wind profiles and turbulent wind spectra available in the programs, but it is limited to the ones that are relevant for the project. Spectra and profiles that are site dependent, such as Statfjord (WindSim) and low level jet (TurbSim) are not included in the table to limit the amount of

input data.

Table 16: Mean vertical wind profiles available in TurbSim and WindSim

Program	TurbSim	TurbSim	WindSim
Version	v 1.06.00	v2 (alpha)	v 3.5
Mean wind profiles			
Exponential shear profile	x	x	x
Logarithmic shear profile	x	x	
User defined		x	

Table 17: Turbulent wind spectra available in TurbSim and WindSim

Program	TurbSim	TurbSim	WindSim
Version	v 1.06.00	v2 (alpha)	v 3.5
Turbulent wind spectra			
von Kármán wind spectrum	x	x	
Eurocode NS-EN 1191			x
Kaimal wind spectrum	x	x	x
Harris (NORSOK N-003)			x
Panofsky (NORSOK N-003) (crosswind)			x
User defined		x	

In TurbSim there is also an option to include atmospheric stability in the generated wind field. However, this is not included in the discussion here as it is common to model the wind field with a neutral atmospheric stability.

Coherence is modelled using a function in both turbulence programs. A list of the relevant coherence functions are given in Table 18. In TurbSim v. 1.06.00 the coherence is included only in the main flow direction, and not in the transverse and vertical direction.

Mann turbulence wind generator Another option is to use the Mann turbulence wind generator developed at DTU. This turbulence generator can only be used together with the Mann turbulence model. Different wind spectra can be modelled by changing the input variables, but these values can only be found after a fitting of the model.

The advantage of using this turbulence model is that all three velocity components are correlated since they are based on the velocity tensor

Table 18: Coherence functions available in TurbSim and WindSim

Program	TurbSim	TurbSim	WindSim
Version	v 1.06.00	v2 (alpha)	v 3.5
Coherence functions			
Davenport		x	x
NS3491-4:2002			x
Panofsky coherence function			x
IEC 61400-1:2007	x	x	x
API coherence model (Froya)		x	
general spatial coherence model		x	

5.3 Wind in Norwegian fjords

5.3.1 Local effects

Norwegian fjords can be considered as gaps in the topography. The wind in fjords is therefore dominated by the pressure gradient along the fjord, which has two origins: the synoptic pressure and the temperature gradient between both ends of the fjord.

In Southern Norway, the inland air is generally relatively cold and dense compared to the temperate marine air on the coast. As a result, the dense and heavy cold inland air tends to flow towards the coast, as illustrated in Figure 40.

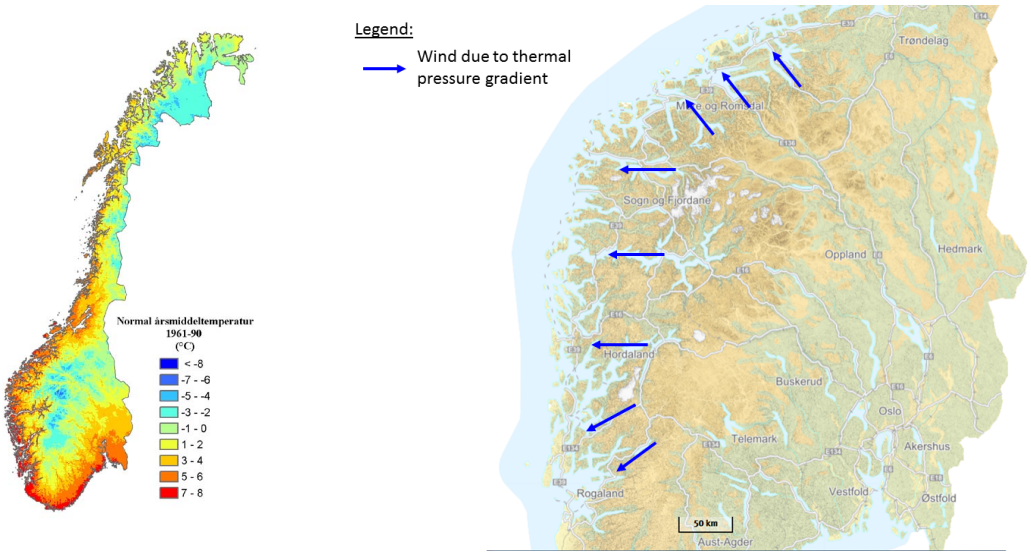

(a) Mean temperatures in Norway over the period 1961-90

(b) Wind due to thermal gradients

Figure 40: Mean temperatures in Norway and resulting induced wind in fjords.

The synoptic pressure gradient is given by the positioning of high and low pressures systems over the North Atlantic.

South-West synoptic flow is observed in Southern Norway when a low pressure system is centered over the North Sea. In fjords, the air will therefore tend to flow directly from high to low pressures, i.e. from South-East towards North-West. Figure 41, which illustrates that situation, shows that the synoptic and thermal pressure gradients both drive the wind in towards the fjords' outlet in the Møre og Romsdal region. In the Sogn og Fjordane, Horaland and Rogaland regions, the synoptic wind is directed opposite from the synoptic and thermal pressure gradients, thus creating a strong reverse flow on the upper boundary of the fjord and limiting the wind velocity in the fjord.

South synoptic flow is observed in Southern Norway when a low pressure system is centered over the North Sea. In fjords, the air will therefore tend to flow directly from high to low pressures, i.e. from East towards West. Figure 42, which illustrates that situation, shows that the synoptic and thermal pressure gradients both drive the wind in towards the fjords' outlet in the Sogn og Fjordane and Horaland regions. In the Møre og Romsdal region, the synoptic wind has a relatively small angle relative to the synoptic and thermal pressure gradients, thus creating a driving flow on the upper boundary of the fjord and which can help driving the wind flow in the fjord. In the Rogaland region, the synoptic wind is directed opposite from the synoptic and thermal pressure

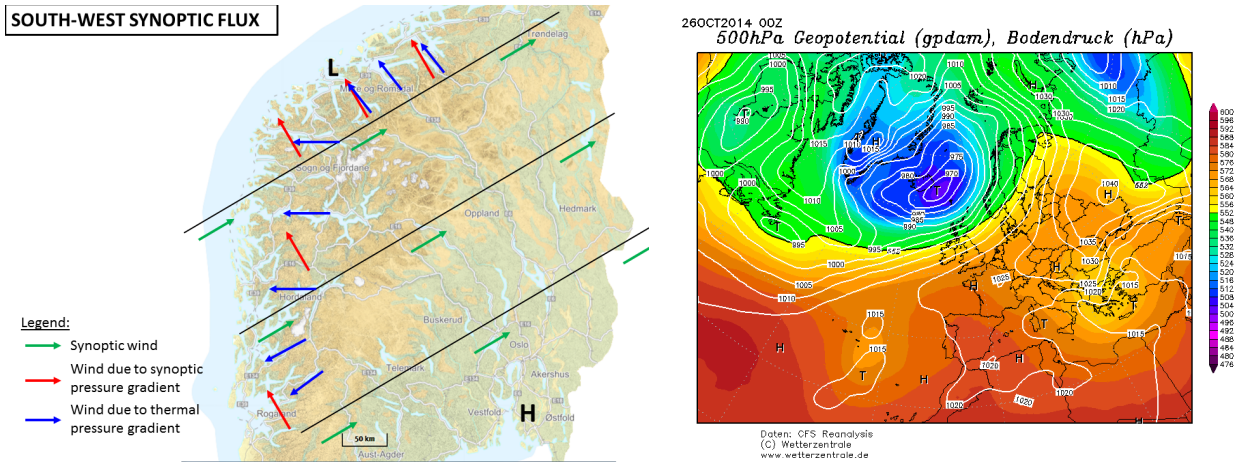

(a) SW synoptic flow (b) SW synoptic flow

Figure 41: South-West synoptic wind.

gradients, thus creating a strong reverse flow on the upper boundary of the fjord and limiting the wind velocity in the fjord.

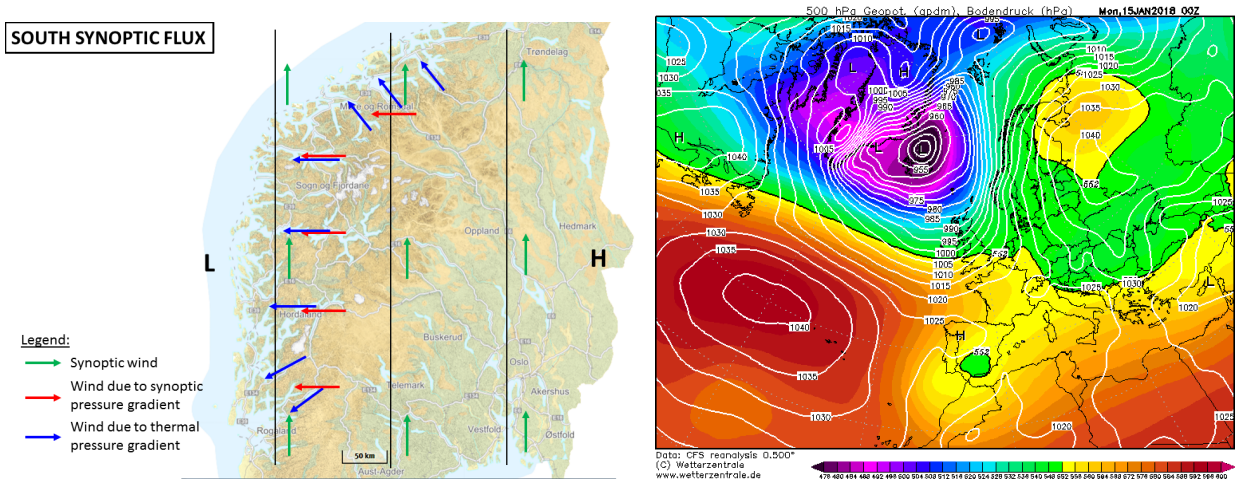

(a) S synoptic flow (b) S synoptic flow

Figure 42: South synoptic wind.

South-East synoptic flow is observed in Southern Norway when a high pressure system is centered over Scandinavia and the low pressure systems are located at lower latitudes. In fjords, the air will therefore tend to flow directly from high to low pressures, i.e. from North-East towards South-West. Figure 43, which illustrates that situation, shows that the synoptic and thermal pressure gradients both drive the wind in towards the fjords' outlet in the Rogaland region. In the Sogn og Fjordane and Horaland regions, the synoptic wind has a relatively small angle relative to the synoptic and thermal pressure gradients, thus creating a driving flow on the upper boundary of the fjord and which can help driving the wind flow in the fjord. In the Møre og Romsdal region, there is no synoptic pressure gradient along the fjord. The wind in the fjords will therefore be driven by the thermal pressure gradients.

For other synoptic flow directions, the different wind driving forces in the fjords do not act in the same direction, not creating marked gap flow effects.

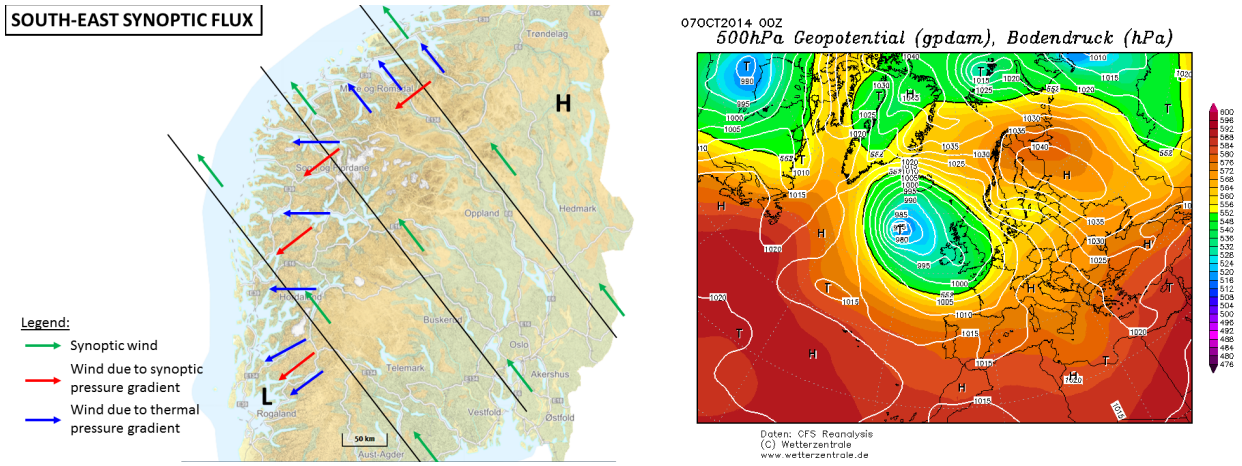

(a) SE synoptic flow

(b) SE synoptic flow

Figure 43: South-East synoptic wind.

When the synoptic wind is weak (Figure 44), mountain or sea breezes can develop in coastal areas, as described in Section 5.1.2.

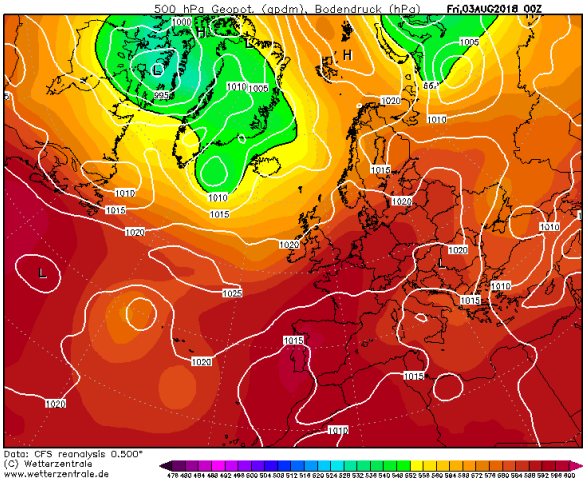

Figure 44: Weak synoptic wind.

5.3.2 Atmospheric models

In Norway, it is the Norwegian Meteorological Institute (met.no) that forecasts weather, monitors the climate and conducts research. The Norwegian Meteorological Institute is part of the HIRLAM consortium. Since 2013, it is the HARMONIE/AROMA model which is used as a regional model for weather forecasting in Norway.

The complex topography in southern Norway calls for the need to develop high-resolution datasets able to realistically capture the local variability and quantification of weather parameters. Several datasets are made available from the operational numerical weather prediction (NWP) model HARMONIE AROME on a 2.5x2.5 km2 grid. In addition numerous model-based climate datasets are available from different project coordinating regional downscaling of global climate model experiments, forced by re-analysis data or transient climate change simulations.

For example, within a project for Avinor (Midtbø et al., 2008), the Norwegian Meteorological Institute has evaluated the wind turbulence level at several Norwegian airports. The turbulence simulations at the airports were performed with the SIMRA model at a 100m resolution. SIMRA is a model based upon Reynolds equations with a standard (K, epsilon) turbulence closure and boundary conditions (Eidsvik and Utnes, 1997). It has the capability of predicting flows with separation, attachment, hydraulic transitions and internal wave breaking. The SIMRA model has a dynamic estimation of turbulent kinetic energy and dissipation, and predicts turbulent kinetic energy (TKE). The square root of TKE has the dimension of velocity and is used as an indicator of turbulence intensity. For each point of time, the SIMRA model is run with constant boundaries until a stationary solution is achieved. Downscaling was applied several time in order to obtain a boundary conditions for the SIMRA domain, as illustrated in Figure 45. In their report (Ødegaard et al., 2009), the Norwegian Meteorological Institute concluded that "The wind forecast in complex terrain benefits from higher resolution, in particular when wind direction is taken into the verification score, but also wind speed can be improved."

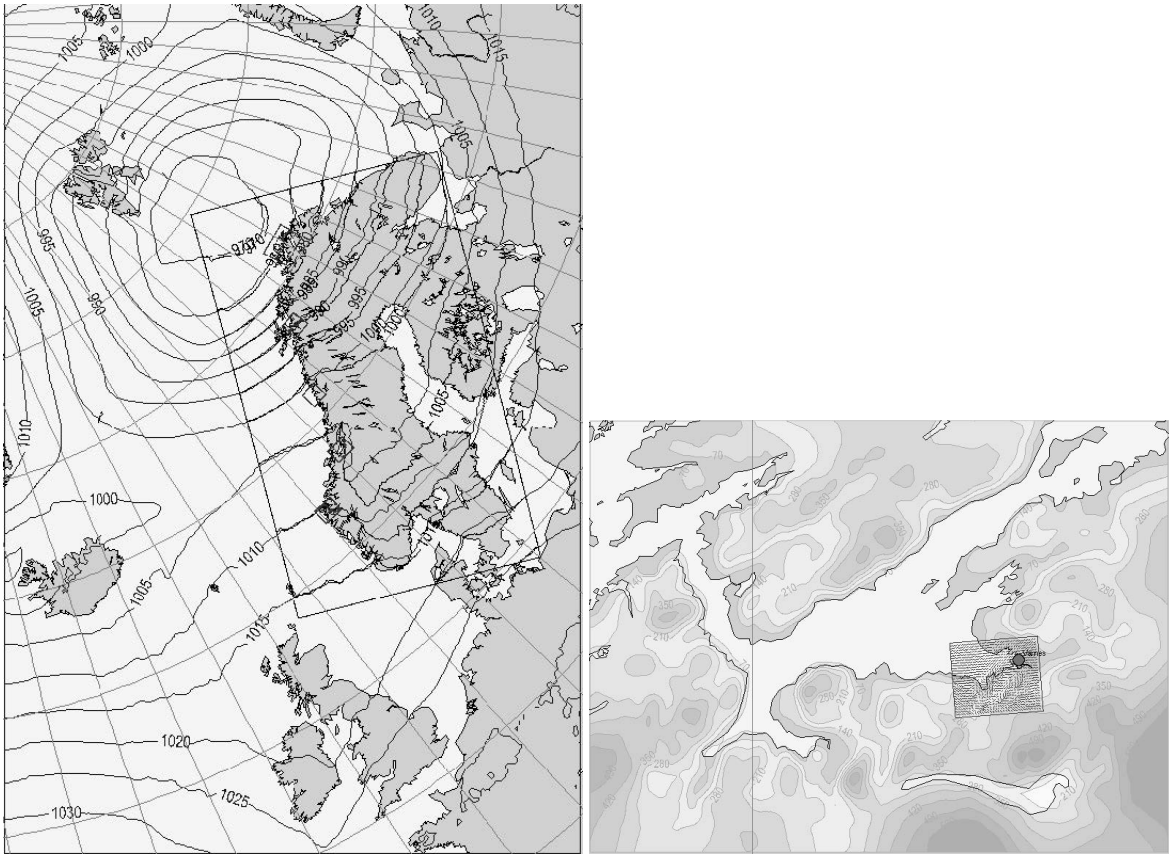

(a) Model domains for (from outer to inner rectangles) Hirlam 10-km, UM 4-km and UM 1-km. The smallest UM 1-km areas cover the studied airports.

(b) Model domain for UM 1-km for Værnes airport and SIMRA domain around Værnes

Figure 45: Model domains used in the downscaling process.

The Norwegian Meteorological Institute has performed a regional downscaling of the ERA40 reanalysis to produce detailed, atmospheric fields using the HIRLAM model on 10-11 km resolution. The primary objective has been to provide reliable high-resolution wind and wave fields for Norwegian waters. The result of this reanalysis of wind and waves for the North Sea, the Norwegian Sea and the Barents Sea is referred to as NORA10 (Reistad et al., 2011). The period covered is from September 1957 until today. Surface winds are available every hour.

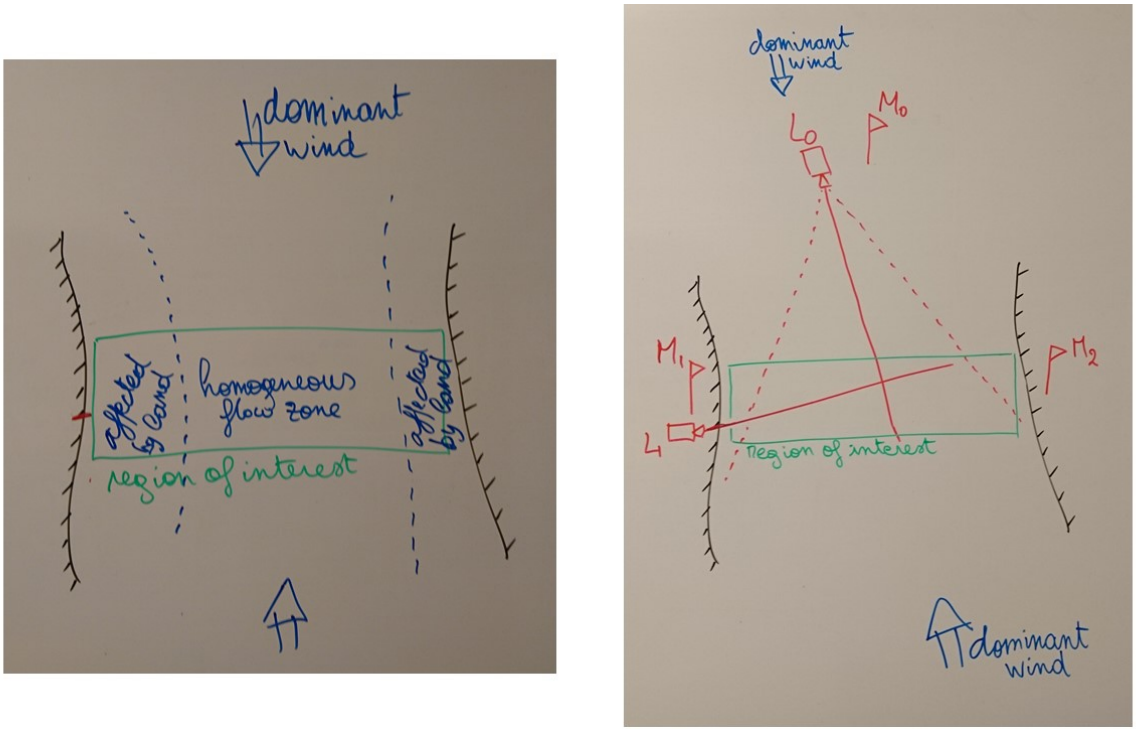

Figure 46: Schematic suggested measurement campaign.

5.3.3 Measurements of uniform wind

The wind characteristics defined in the previous section, i.e.:

- the wind profile,
- the turbulence intensity,
- the covariance,
- the integral length scales,
- the auto spectral density,
- the spectral density,
- the coherence,
- the spectral velocity tensor

must be documented at the location of interest for each relevant wind conditions.

Wind in coastal Norway is challenging to characterize since it is often immersed in complex terrain.

In a flat terrain with uniform ground roughness, the wind characteristics are independent of the wind direction. But when the location of interest in immersed in complex terrain with varying upstream ground roughness, the wind characteristics must be documented for each relevant wind direction.

Temperature and precipitation is measured at stations which register local values that in essence can be considered as point-measurement. Thus, the temperature and precipitation values measured in one or several points within a catchment may be unrepresentative for a region, especially for larger areas with complex terrain. [...] Another aspect is that most of the stations are situated in low lying regions. High-elevation regions with complex terrain are therefore associated with larger uncertainty.

This section suggests a generic measurement campaign setup that can be used to document the wind characteristics in a fjord.

Prior to setting up on-site measurements, information regarding dominant wind in the region as well as influence of topography on local wind should be obtained from general understanding of the local weather systems, hindcast and wind simulations. Due to the gap effects which can occur in a fjord (Section 5.3.1), dominant wind directions are likely to be aligned with the fjord orientation (Figure 46).

This information can then be used to position a reference mast (M0) in a location that is representative of the site of interest (e.g. low coastal land on the shore of the fjord or a nearby island). Additional masts (M1 and M2) should also be positioned on both sides of the fjord to characterize the wind in those areas which are strongly affected by the surrounding topography. Those met mast should be in place for a sufficiently long duration in order to collect representative long-term statistics of the local wind. It is generally recommended to install 4 - 5 anemometers at different heights along the masts in order to characterize the vertical wind shear with sufficient accuracy. If it can be reached by the met-mast, sensors should also be placed at the height of interest for the targeted application.

In addition to the met masts, lidars can be used to investigate the flow homogeneity across the region of interest and document the turbulence in the homogeneous area.

In order to assess the possible effects of the fjord topography on the homogeneity of the flow, a long-range lidar (L0) can be positioned with its line of sight parallel to the dominant wind direction and with an azimuth sector covering the region of interest, as described in (Cheynet, 2016). The elevation angle of the lidar should be as low as possible to measure the horizontal flow while pointing at the elevation of interest in the region of interest.

The lidar L0 can also be used in Range Height Indicator mode to document the mean wind profile.

(Cheynet et al., 2017b) - The fluctuations of the coherence and the decrease of the coefficient c2 with r reflects the increasing difficulty to estimate the wind co-coherence at greater scanning distances and larger lateral separations. The variation of the coefficient is also expected to partly reflect the physical change of the flow conditions closer to land.

(Cheynet et al., 2017b) - Since one of the lidar beams in the E-W measurement configuration more or less pointed in the mean wind direction, wind velocity records along the beam provide a unique opportunity to revisit Taylor's hypothesis of frozen turbulence [47], in relation to the estimation of the along-beam coherence.

Cheynet (Cheynet, 2016) performed an assessment of the potential use of Lidars to characterize the wind conditions at the bridge location. The comparison of the time series recorded by the long range lidar, the short range lidar and the corresponding anemometer show very good agreement once the lidar time series have been shifted based on Taylor's frozen turbulence hypothesis.
(Cheynet et al., 2017b) - Since one of the lidar beams in the E-W measurement configuration more or less pointed in the mean wind direction, wind velocity records along the beam provide a unique opportunity to revisit Taylor's hypothesis of frozen turbulence, in relation to the estimation of the along-beam coherence.

(Cheynet et al., 2017b) - the along-beam spatial averaging (ABSA) of the velocity data leads to a truncation of the wind spectrum above 0.22 Hz (cf. Section 3.3). More details about the ABSA are given in Section 2.6.

(Cheynet et al., 2016b) - The WindScanners are observed to slightly overestimate the integral length scales, which could not be explained by the laser beam averaging effect alone. On the other hand, the spatial averaging effect does not seem to have any significant effect on the coherence.

In order to document the turbulence intensity in the homogeneous flow zone, a short-range lidar with high temporal and spatial resolution (L1) can be positioned on one of the side of the fjord, ideally with a line of sight corresponding to the intended fjord crossing trajectory. The two lidars beams should cross at the elevation of interest. L0 can be used to document the along wind coherence of the longitudinal wind. L0 and L1 can be used in combination to document the across wind coherence of the longitudinal wind, and the along wind and across wind coherence of the lateral wind, as described in (Cheynet, 2016).

An extended monitoring time is required in order to cover a representative variety of wind conditions.

5.4 Case studies

Within the E39 project, wind characterization is conducted at several fjord locations in Norway, using various instruments. The wind measurements, performed by Kjeller Vindteknikk (KVT), consists of 50 to 100 m high met mast at ends of each proposed crossing, three additional masts to investigate horizontal coherence, 4 synchronized lidars and CFD simulations in each fjord.

KVT - Measurements masts - overview

Site	Fjord	Mast height	Mast type	Data start
Julbø	Julsundet	50 m	Guyed pipe mast	07.02.2014
Midsund	Julsundet	50 m	Guyed pipe mast	06.02.2014
Nautneset	Julsundet	68 m	Lattice tower	07.07.2016
Halsaneset	Halsafjorden	50 m	Guyed pipe mast	26.02.2014
Åkvik	Halsafjorden	50 m	Guyed lattice mast	06.03.2015
Kvitneset	Sulafjorden	96 m	Guyed lattice mast	24.11.2016
Trælboneset	Sulafjorden	78 m	Guyed lattice mast	Spring 2017
Langeneset	Sulafjorden	98 m	Lattice tower	Spring 2017
Kårsteinen	Sulafjorden	62 m	Lattice tower	Spring 2017
Rjåneset	Vardalsfjorden	72 m	Guyed lattice mast	Spring 2017
Synnøytangen	Bjørnafjorden	50 m	Guyed pipe mast	23.02.2015
Svarvehelleholmen	Bjørnafjorden	50 m	Guyed pipe mast	18.03.2015
Ospøya 1	Bjørnafjorden	50 m	Guyed pipe mast	03.12.2015
Ospøya 2	Bjørnafjorden	50 m	Guyed pipe mast	17.12.2015
Landrøypynten	Langenuen	50 m	Guyed pipe mast	06.03.2015
Nesøya	Langenuen	50 m	Guyed pipe mast	24.02.2015

Data coverage: 98- 99%

Figure 47: KVT Met mast overview.

Due to the complex coastal topography, it is a challenge to locate the met masts at representative locations. Sites are chosen to remove as much as possible influence of the terrain, but it is not always possible. In some cases, part of the measurements are highly influenced by surrounding topography and/or vegetation and should not be used. Twice a year, KVT delivers written reports which include long term statistics, extreme value analysis as well as analysis of 1- and 2-point spectra based on the latest measurements. The available data cover a period which is too short for a long-term climate description, but other weather stations (for which recorded data are available since 1979) are used in combination with CFD simulations to achieve that purpose.

The wind measurements, recorded at 10 Hz and over 10 min periods, have been made available by MET for the Møre og Romsdal region at `https://thredds.met.no/thredds/catalog/obs/mast-svv-e39/Aggregated_MAST_observations/catalog.html`.

This chapter summarizes the main finding of different wind characterization initiatives based on the material available to the authors of this report. The locations covered in this Section are: Bjørnafjord, Lysefjord and Sulafjord. Other relevant locations that are considered for the issue of this report are: Halsafjord, Sognefjord, Hardangerfjord, Sotra bridge and Hålogaland bridge.

5.4.1 Bjørnafjord

Based on the met mast measurements and simulations performed and analyzed by Kjeller Vindteknikk (Harstveit et al., 2016), the wind design basis was published in (SVV, 2017).

A very short measurement campaign is also reported by (Cheynet et al., 2017b) from May 2016 and June 2016 in Bjørnafjorden. These were measurements using synchronized long-range doppler wind lidars mid-fjord. Two scanning configurations were used, as presented in Figure 48. During the measurement period, the wind direction was predominantly from north-northwest, with wind velocities up to 18 m/s at an altitude of 25 m above the mean sea level.

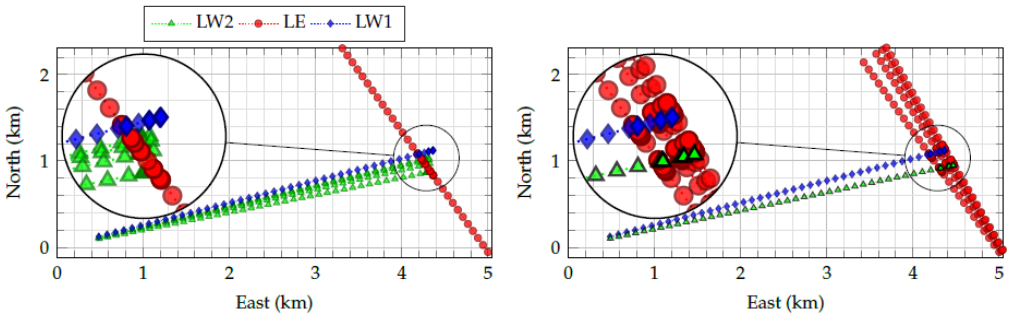

Figure 48: (**left**) North-South (N-S) scanning configuration; (**right**) East-West (E-W) scanning configuration.

Mean wind speed Figure 49 illustrates the mean wind speed wind rose recorded during the year 2000 to 2017 at 10 m height in Bjørnafjord.

Figure 50 gives the extreme wind speed at each met-mast for return periods of 2 to 100 years. Table 19 are the resulting extreme wind speeds reported in the Met Ocean (SVV, 2017).

The Metocean report (SVV, 2017) recommends the usage of a wind profile based on α exponential profile with $\alpha = 0.127$. The reference wind speed U_{ref} at z_{ref} = 10 m is provided for different return periods in Table 19 and should be used in combination with a reduction coefficient provided for each wind sector. The mean wind speed distribution across the fjord should either be considered as constant or linearly varying from $0.6 \cdot U_{ref}$ at one end to U_{ref} at the other end.

Figure 51 illustrate the distribution of the extreme wind in the fjord, which clearly shows an horizontal shear profile.

Table 19: 1 hour mean wind in 10m height (SVV, 2017)

Return period [years]	Wind speed, U [m/s]
1	21.5
10	26.0
100	29.5
10 000	36.0

(Cheynet et al., 2017b) investigated the flow uniformity by analyzing the along-beam mean wind velocity and its standard deviation along the two lidars beam directions. It is observed that the wind flow is rather uniform along the LW2 lidar beam while large variations on the standard deviation are observed on the first two kilometers of the LE beam, reflecting the strong turbulence intensity on the southern end of the fjord.

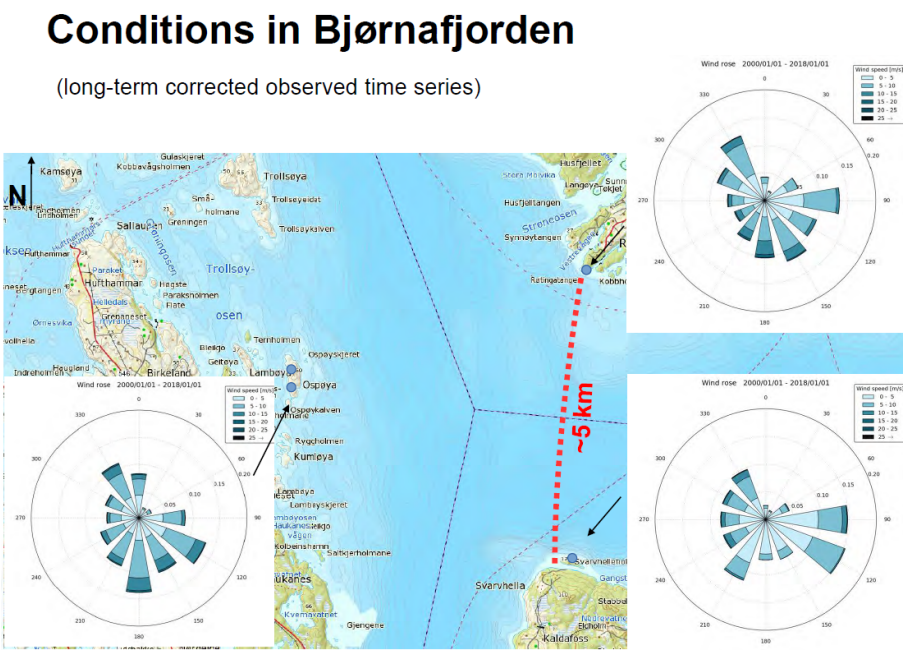

Figure 49: Mean wind speed wind rose recorded during the year 2000 to 2017 at 10 m height in Bjørnafjord.

Turbulence intensity Met-mast measurements also shows very high turbulence intensity on the southern side of the fjord for wind coming from the south, as shown by Figure 52. The recommended along wind turbulence intensity I_u are provided in Table 20. The lateral and vertical turbulence component I_v and I_w found from the measurements are respectively $0.85I_u$ and $0.55I_u$ (SVV, 2017).

Table 20: Turbulence intensity (SVV, 2017)

Height above sea [m]	Turbulence intensity for sectors 0-150 and 210-360	Turbulence intensity for sector 150-210
10	14%	Linearly decreasing from 30% at southern tower to 17% in the north
50	14%	Linearly decreasing from 30% at southern tower to 17% in the north
200	12%	15%

(Cheynet et al., 2017b) - For wind velocities above 8 m/s, the average values of I_u and I_v estimated using the N-S scanning configuration are 0.056 and 0.042, respectively. For the the E-W scanning configuration, I_u and I_v are in average equal to 0.043 and 0.030, respectively. The turbulence intensity estimates become steady for a mean wind velocity around 6 m/s. The ratio I_u/I_v is, therefore, equal to 0.75 for the E-W scanning configuration and 0.70 for the N-S scanning configuration.

(Cheynet et al., 2017b) - For u $\geq$ 12 m/s, the turbulence intensity seems to be rather constant, whereas the Frøya expression (Andersen and Løvseth, 2010) leads to an increase of the turbulence intensity with the mean wind velocity. This suggests that the roughness of the sea in the Bjørnafjord is not clearly increasing with the mean wind velocity, as typically observed in an offshore environment.

Extreme wind calculations

Extreme value analysis of annual maxima using Gumbel-Lieblein methodology

Return levels of 10-minute wind at top-sensor

	2 år	10 år	50 år	100 år
Synnøytangen	25.3	29.2	32.2	33.4
Svarvhelleholmen	24.0	29.0	32.7	34.1
Ospøya 1-A	25.6	30.3	33.8	35.2
Ospøya 2-B	25.9	30.5	34.0	35.4
Landrøypynten	24.9	28.6	31.5	32.7
Nesøya	23.4	27.0	29.8	30.9

100-year return level of 10-minute wind at top as function of wind direction

	N	NØ	Ø	SØ	S	SW	W	NW	ALL
Synnøytangen	19.2	14.9	21.4	26.0	30.4	29.6	31.3	31.4	33.4
Svarvhelleholmen	21.0	21.1	30.0	17.9	16.7	31.5	31.8	32.4	34.1
Ospøya 1 – A	32.4	19.4	24.9	27.7	30.0	28.6	31.7	34.3	35.2
Ospøya 2 – B	34.3	23.2	25.4	29.6	29.8	30.9	33.1	31.4	35.4
Landrøypynten	21.7	13.5	17.8	32.0	29.2	25.2	29.4	29.9	32.7
Nesøya	19.5	15.0	16.5	29.3	29.2	23.3	26.2	28.1	30.9

KJELLER VINDTEKNIKK

Also available directional 100 m gusts

Figure 50: Return periods in Bjørnafjord.

Wind spectra According to (SVV, 2017), the frequency distribution of the turbulence components and the normalized co-spectrum shall be taken from N400.

(Cheynet et al., 2017b) - In Figure 9, the measured spectral peak and the one estimated using the NORSOK spectrum are well aligned. The spectral peak of the N400 spectrum is located at a slightly higher wave-number than the measured one. For k $\leq 2\text{x}10^{-3}$ m^{-1}, the NORSOK spectrum gives higher spectral values than observed from the recorded data. Although the flow from north-northwest recorded in the Bjørnafjord comes from the ocean, it is likely affected by the islands upstream of the monitored domain as well as the shoreline of the fjord. For frequencies above 0.22 Hz and u = 14 m/s, i.e., wave-numbers above 0.10, the right panel of Figure 9 shows that the PSD of the along-beam wind velocity component is considerably attenuated by the ABSA, viz. The high-frequency turbulent components are under-represented in the lidar data. Figure 10 shows the Su spectrum, estimated without normalization by σ_u^2. Consequently, the wind spectra need to be split into several velocity bins, since a different mean wind velocity now has a significant effect on the magnitude of the PSD estimate. In Figure 10, the N400 spectra is estimated with z0 = 0.0001 m, which is 30 times lower than proposed in the Handbook N400. Nevertheless, it leads to a fairly good agreement between with the measured wind spectra, especially for u $\geq$ 15 m/s. The NORSOK spectrum is found to systematically overestimate the PSD of the along-wind velocity component, which is likely due to the fact that this spectrum is site-specific.

The observed wind spectra was compared to the one provided by Norwegian Petroleum Industry Standard and the Norwegian Handbook for bridge design, and a good overall agreement was observed for wave-numbers below 0.02 m-1. Larger wave numbers was not considered due to limitations of the lidars.

Coherence measurements Coherence measurement across the span of a fjord is difficult. (Cheynet et al., 2017b) measured for two months with lidars, and the results are presented in Table 21. The coherence is fitted to Davenport coherence model. The decay values measured by others are much lower, and the Handbook N400 (Vegvesen, 2015) also recommends a lower value. A high value indicates a lower coherence.

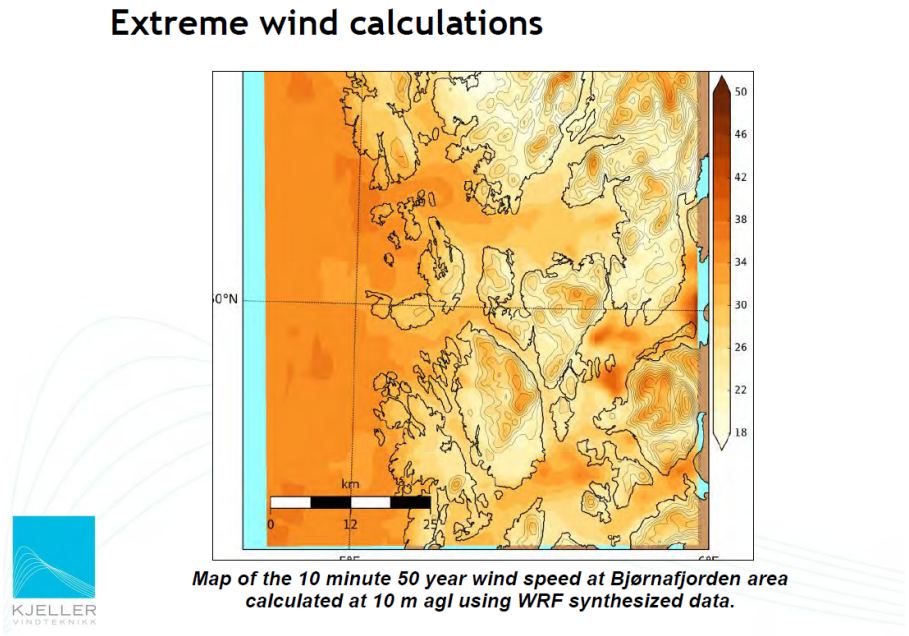

Figure 51: Extreme wind simulation in Bjørnafjord.

Table 21: Decay coefficients obtained by full-scale reference as listed in (Cheynet et al., 2017b)

Reference	Bridge	C_u^y	$\bar{u}(m/s)$	$z(m)$	I_u	d_y
Jensen and Hjort-Hansen	Sotra	10.7	13.0	60	0.11	5-16
Sacré and Delaunay	Saint Nazaire	11 ± 1	13.5 ± 1.5	73	0.06	5-35
Toriumi et al.	Ohnaruto	12.5	23	74	0.04	11-233
Cheynet et al (Cheynet et al., 2017b)	Bjørnafjord	21.3	6-14	25	0.04	18 - 177

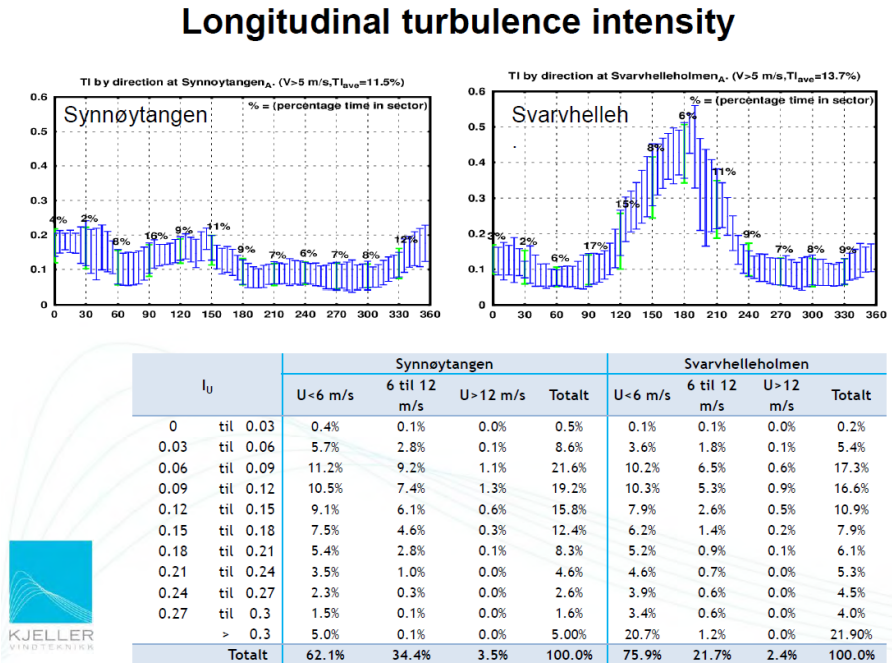

I_U	Synnøytangen				Svarvhelleholmen			
	U<6 m/s	6 til 12 m/s	U>12 m/s	Totalt	U<6 m/s	6 til 12 m/s	U>12 m/s	Totalt
0 til 0.03	0.4%	0.1%	0.0%	0.5%	0.1%	0.1%	0.0%	0.2%
0.03 til 0.06	5.7%	2.8%	0.1%	8.6%	3.6%	1.8%	0.1%	5.4%
0.06 til 0.09	11.2%	9.2%	1.1%	21.6%	10.2%	6.5%	0.6%	17.3%
0.09 til 0.12	10.5%	7.4%	1.3%	19.2%	10.3%	5.3%	0.9%	16.6%
0.12 til 0.15	9.1%	6.1%	0.6%	15.8%	7.9%	2.6%	0.5%	10.9%
0.15 til 0.18	7.5%	4.6%	0.3%	12.4%	6.2%	1.4%	0.2%	7.9%
0.18 til 0.21	5.4%	2.8%	0.1%	8.3%	5.2%	0.9%	0.1%	6.1%
0.21 til 0.24	3.5%	1.0%	0.0%	4.6%	4.6%	0.7%	0.0%	5.3%
0.24 til 0.27	2.3%	0.3%	0.0%	2.6%	3.9%	0.6%	0.0%	4.5%
0.27 til 0.3	1.5%	0.1%	0.0%	1.6%	3.4%	0.6%	0.0%	4.0%
> 0.3	5.0%	0.1%	0.0%	5.00%	20.7%	1.2%	0.0%	21.90%
Totalt	62.1%	34.4%	3.5%	100.0%	75.9%	21.7%	2.4%	100.0%

Figure 52: Turbulence intensity in Bjørnafjord.

Vertical Coherence of the Along-Wind Component The vertical coherence measured at each met mast are shown in Table 22. The values are a bit higher than given in the Handbook (Vegvesen, 2015), which indicates a lower vertical coherence.

Table 22: Vertical coherence based on data from Bjørnafjorden og Langenuen (Harstveit and Ágústsson, 2017)

		Sensor A - B			Sensor A-C		
Station	p	Cuu	Cvv	Cww	Cuu	Cvv	Cww
Synnøytangen	0.5	14.6	12.3	4.8	20.0	22.0	12.9
Svarvhelleholmen	0.5	12.3	9.1	4.3	15.9	21.2	10.5
Ospøya *	0.5	11.5*	8.2*	3.7*	x	x	x
Handbook N400 (Vegvesen, 2015)		10	6.5	3.0	10	6.5	3.0

* Ospøya C - sensor located at 33 m

Horizontal Coherence The horizontal coherence was measured based on the two met masts at Ospøya. The coherence was present in easterly wind between the two met masts, while wind from west was showing a higher variance. The coherence value for the easterly wind is 8, which a bit lower than given in the handbook (Vegvesen, 2015). Thus, the measured coherence in easterly wind is higher than recommended in the handbook.

Longitudinal Coherence of the Along-Wind Component (Cheynet et al., 2017b) - For a perfectly frozen turbulent flow moving toward the lidar, the wind data, which are simultaneously recorded at different range gates, are distinctly out of phase because the flow recorded in a given range gate is a “delayed version” of the flow recorded upstream. The negative values in the co-coherence function in the left panel of Figure 11 reflect such an out-of-phase appearance of the wind gusts, not accounted for by the Davenport coherence model. The 4-parameter coherence function (Equation 21) is, therefore, fitted to the measurement data. The estimated value

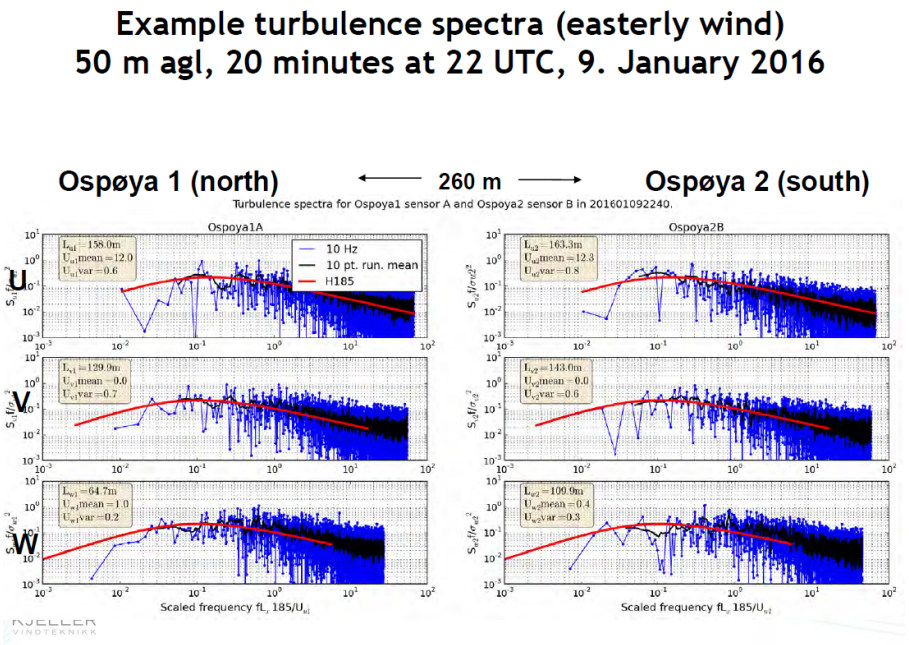

Figure 53: Spectra at Ospøya in Bjørnafjord.

of c4 is very close to 2π, which is the expected value, provided Taylor's hypothesis is applicable, according to ESDU 86010 [30]. For a perfectly frozen turbulent field, the decay coefficient Cx u in the Davenport model or c1 in Equation 21, should be equal to 0.

Lateral Coherence of the Longitudinal Wind Fluctuations Figure 55 shows the average coherence estimated for six different lateral separations obtained by (Cheynet et al., 2017b) in a NNW wind flux. The measured exponential decay parameter is larger than the one given in the Handbook N400 as well as the values found in the literature for a flow measured above the sea with a low turbulence intensity (Table 21).

Although the coherence decreases for increasing lateral separations, the reduction is rather limited for separations beyond ca. 40 m. The limited "sensitivity" of the coherence function to lateral separations larger than 40 m may be related to the fact that, in general, the coherence becomes weak at such separations.

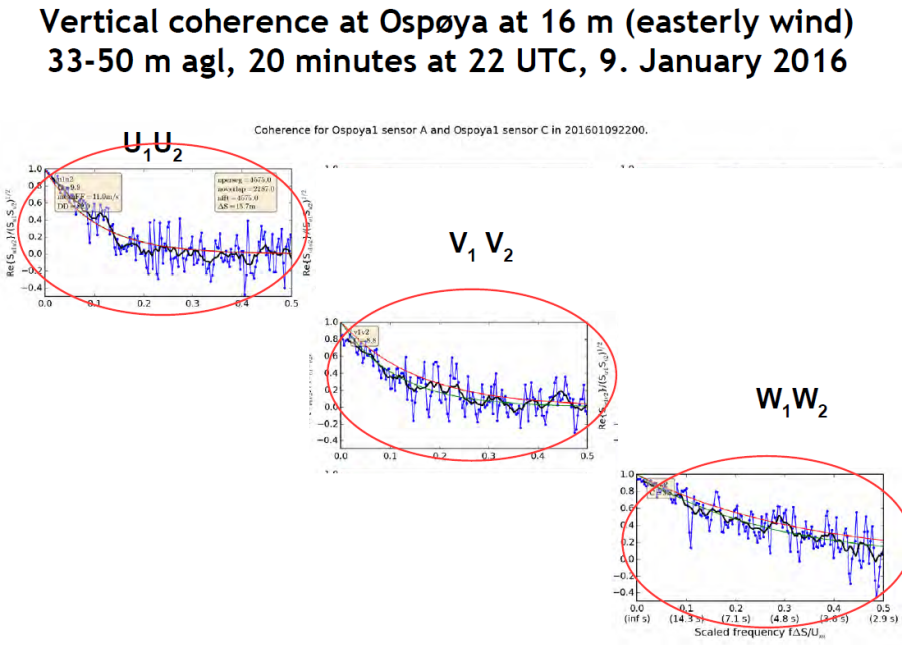

Figure 54: Vertical coherence at Ospøya in Bjørnafjord.

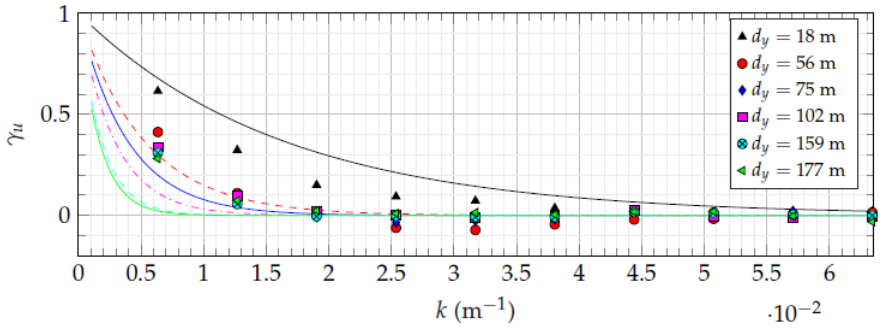

Figure 55: Measured (scatter plot) lateral wind coherence of the along-wind component recorded using the data from LW2 and LE from 18 May 2016 to 21 June 2016 (E-W configuration) fitted with Equation 21 (smooth lines) (Cheynet et al., 2017b).

Table 23: Summary Bjørnafjord

Category	Parameter	in Report	References
SOURCES			
Measurements	Met mast:	Fig. 3(a)	(Harstveit and Ágústsson, 2017)
	Lidars	Fig. 3(b)	(Cheynet et al., 2017b)
Simulations	Extreme wind	Fig. 51	KVT workshop
IN HOMOGENEOUS AREA			
Flow homogeneity	Lidar (LOS)		(Cheynet et al., 2017b)
Long-term statistics	Hindcast		
	Wind roses	Fig. 49	KVT workshop
	Turbulence intensity	Tab. 20	(SVV, 2017)
	Dominant wind directions		
	Return periods	Tab. 19	(SVV, 2017)
		Fig. 50	KVT workshop
Short-term statistics	Integral length scales		
	Wind spectrum	Fig. 53	KVT workshop
			(Cheynet et al., 2017b)
	Horizontal coherence		(Cheynet et al., 2017b)
			(Harstveit and Ágústsson, 2017)
	Vertical coherence	Tab. 22	(Harstveit and Ágústsson, 2017)
		Fig. 54	KVT workshop
AT OTHER LOCATIONS			
Long-term statistics	Hindcast		
	Wind roses	Fig. 49	KVT workshop
	Turbulence intensity	Fig. 52	KVT workshop
	Dominant wind directions		
	Return periods		
Short-term statistics	Integral length scales		
	Wind spectrum		
	Horizontal coherence		
	Vertical coherence		

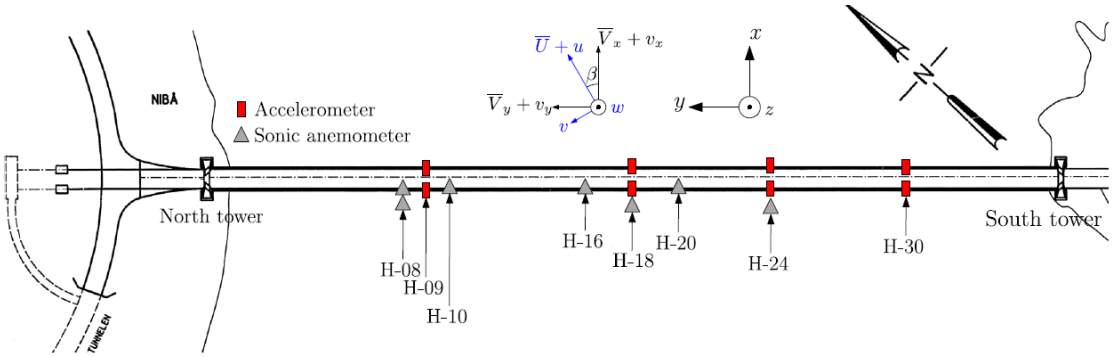

Figure 56: Long-term wind monitoring system at Lysefjorden. The anemomenters are marked as triangles.

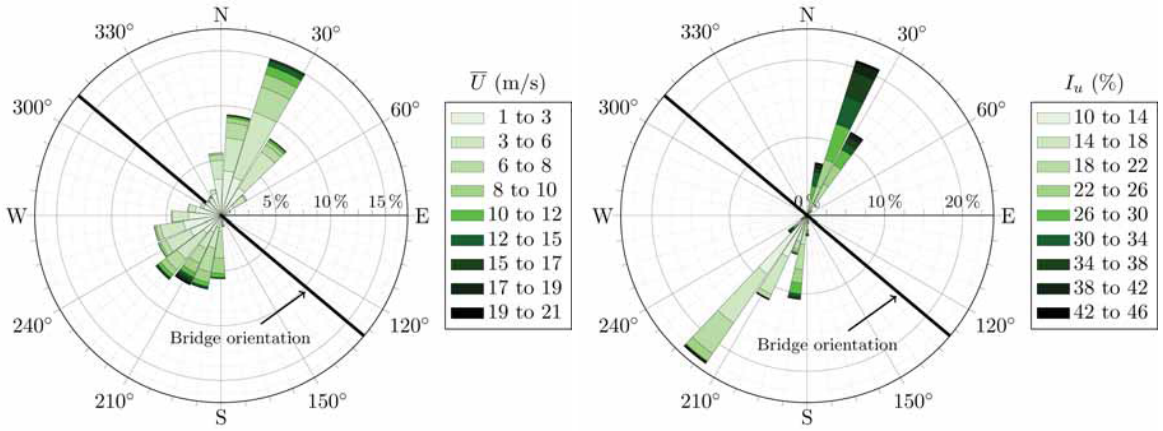

(a) Mean wind speed

(b) Turbulence intensity

Figure 57: Wind roses made of 5.2×104 samples of 10 min duration recorded during the year 2015 at the Lysefjord bridge (Cheynet, 2016).

5.4.2 Lysefjord

The wind condition at Lysefjord has been extensively studied by means of measurement campaigns performed on a suspension bridge located at its inlet (Figure 4). The topography defines two main wind directions from S-SW and N-NE. The S-SW wind comes from across Høgsfjord and may be influenced by a Venturi effect as it approaches the bridge. The N-NE wind may descent from mountains nearby or follow the fjord over a longer path, and may be disrupted by a small island (Bergsholmen) located at 1 km North-East of the bridge, with an altitude of 54 m, which coincides with the elevation of the central part of the bridge.

Based on the long-term wind monitoring, Cheynet (Cheynet, 2016) summarized the wind conditions at the bridge site in a statistical way by using the wind records from the anemometers during the year 2015. As presented on Figure 57, the dominant wind directions, imposed by the fjord topography, were N-NE and S-SW, with a majority of wind records below 10 m/s. In general, a larger TI is recorded for the flow from N-NE, even for large wind velocities.

As for flat and homogeneous terrain and neutral atmospheric stability, it is observed at Lysefjord bridge that the turbulence intensity is high at low wind velocities and that it decreases when the mean wind speed increases. The turbulence intensity remains more or less constant for wind speeds above 10 m/s.

Table 24 displays the average value of the ratios I_v/I_u and I_w/I_u for the year 2015, for a mean wind velocity above 10 m/s. The unusual values of the ratio I_w/I_u for the N-NE exposure and the ratio I_v/I_u for the S-SW

Table 24: Ratios I_v/I_u and I_w/I_u recorded on the Lysefjord Bridge site during the year 2015 for U > 10 m/s, based on wind data recorded by the anemometers on hangers 16, 18 and 20.

Exposure	I_v/I_u	I_w/I_u
N-NE	0.86	0.41
S-SW	1.09	0.58
Solari and Piccardo (2001)	0.71 - 0.88	0.45 - 0.6

Table 25: Coefficients found by fitting Eq. 2.16 to the measured wind coherence displayed in Figure (Cheynet, 2016).

Velocity range (m/s)	c_1	c_2	c_3	c_4
$8 \leq \overline{V}_x < 10$	4.14	0.03	1.09	6.34
$10 \leq \overline{V}_x < 11$	4.35	0.04	1.05	6.32
$11 \leq \overline{V}_x < 13$	4.24	0.03	1.13	5.13
$13 \leq \overline{V}_x < 14$	3.86	0.02	1.14	4.36

exposure may be due to the influence of the topography or the bridge deck on the recorded turbulent wind field, or the fact that the wind data are recorded at an altitude of 60 m above the sea level instead of the standard altitude of 10 m.

Figure 58(a) illustrates the distribution of the integral length scales for the two dominant wind directions, showing that the wind conditions for wind from S-SW and from N-NE are sensibly different. For a S-SW wind direction, larger vertical length scales are generally observed. The integral length scales calculated for every sample of 10 min duration between the 25/10/2014 and 28/10/2014 (S-SW wind) are displayed in Figure 58(b). The integral length scales seem to follow a non-linear trend with a dispersion that increases with the mean wind velocity.

Because flow properties studied along the bridge deck do not necessarily corresponds to cross-flow separations, the cross-flow turbulence length scales are also presented based on the wind component V_x instead of U. The averaged value for the along-span turbulence length scale is 89 m for the v_x-component, 137 m for the v_y-component and 36 m for the w-component.

The von Kármán spectrum was found to be better suited than the Kaimal spectrum or the Simiu & Scanlan spectrum to describe the measured wind spectrum, illustrated in Figure 59. The measured wind spectra are calculated as the average of individual spectra for 75 wind samples of 10 min duration, recorded between the 25/10/2014 and 28/10/2014, with a mean velocity bounded between 8 m/s and 10 m/s.

(Cheynet et al., 2016a) - Fig7 Averaged wind spectra recorded on 07/10/2014 for a N-NE wind (solid lines) and corresponding von K´arm´an spectra (dashed lines).

(Cheynet et al., 2016a) - Fig8 Averaged wind spectra recorded on 26/10/2014 for a S-SW wind (solid lines) and corresponding von K´arm´an spectra (dashed lines).

From the 25/10/2014 to 28/10/2014, the coherence for the wind component normal to the Bridge deck is computed for multiple lateral separations and mean wind velocities. The four-parameter function is fitted to the measured coherence and the fitted decay coefficients are displayed in Table 25. Relatively stable coefficients are obtained for the different mean wind velocities recorded.

In May 2014, two short-range WindScanners were deployed on the West bridge walkway. The scan is carried out in the horizontal plane only. Wind velocity along a 120 m long horizontal line 40 m in front of the bridge deck was surveyed in particular. The scanning sequences were dedicated to the investigation of the characteristics of

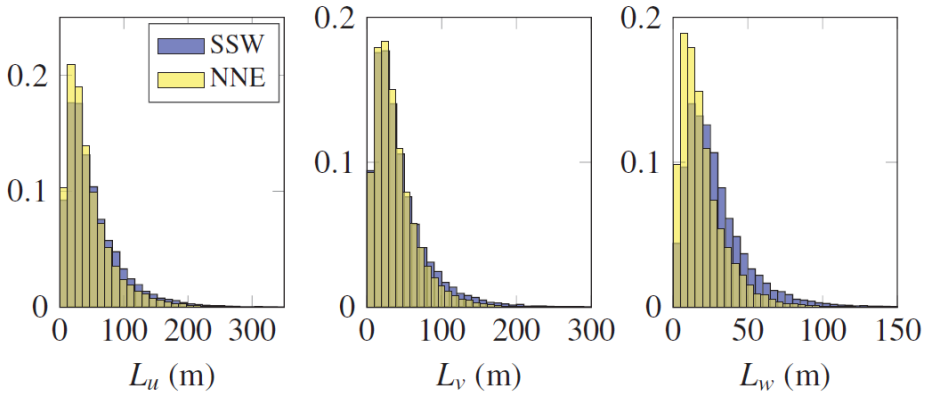

(a) Distribution of the integral length scales recorded in 2015 at the Lysefjord Bridge for the different wind velocity components.

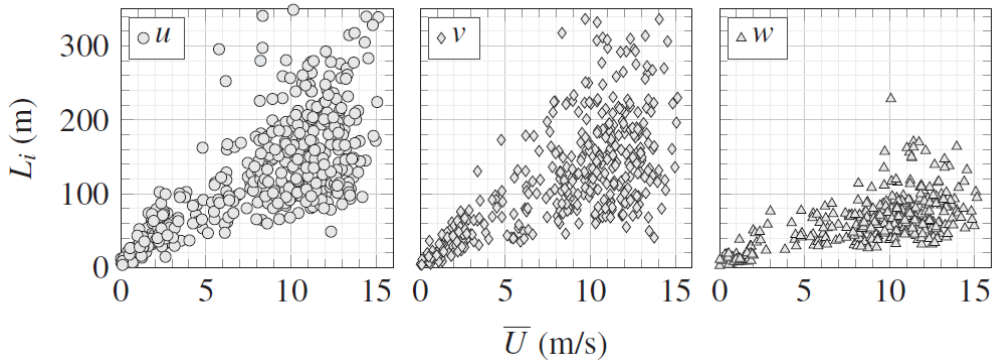

(b) Integral length scales Li, i = u, v,w, as a function of the mean wind velocity at the Lysefjord Bridge site, for winds from S-SW, from 25/10/2014 to 28/10/2014, based on wind records obtained on hangers 16, 18 and 20.

Figure 58: Integral length scales at the Lysefjord Bridge site (Cheynet, 2016).

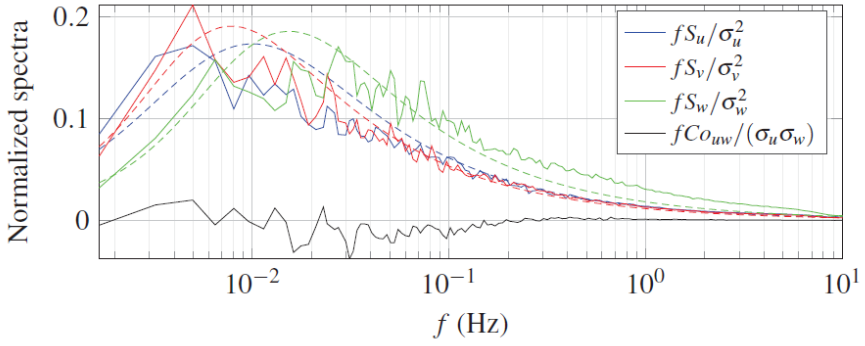

Figure 59: Averaged wind spectra measured for the S-SW exposure at the Lysefjord Bridge site for 8 m/s <U < 10 m/s from 25/10/2014 to 28/10/2014, based on wind records obtained on hangers 16, 18 and 20. The fitted von Kármán spectrum for the different wind components is displayed as dashed lines (Cheynet, 2016).

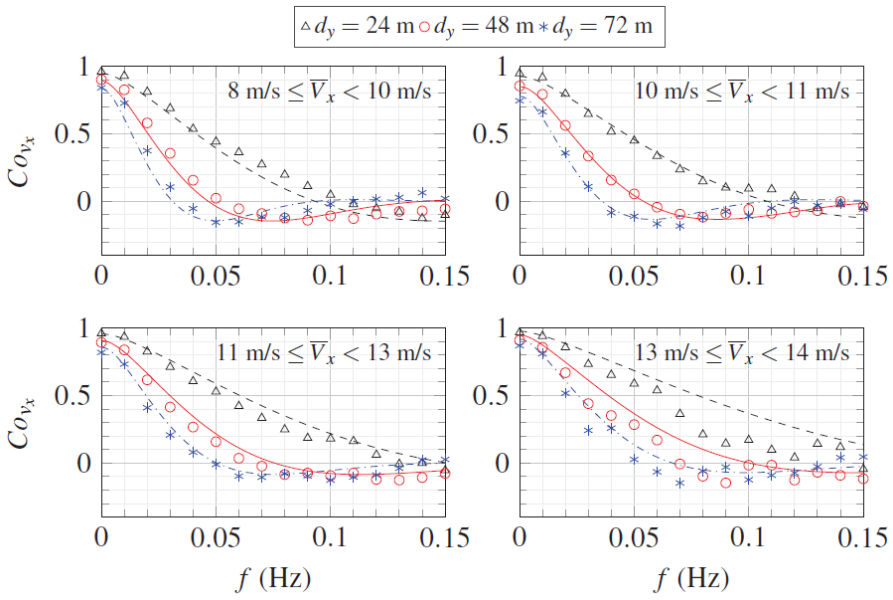

Figure 60: Co-coherence measured (scatter plot) and fitted (dashed lines) for the S-SW exposure at the Lysefjord Bridge site from 25/10/2014 to 28/10/2014. (Cheynet, 2016).

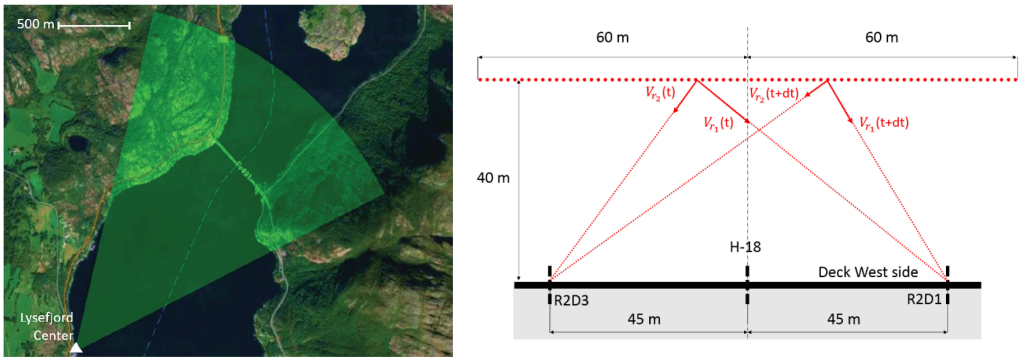

Figure 61: Short-term wind monitoring system at Lysefjorden using lidars

the inflow, as well as to identifying the footprints of the bridge structure in the flow.

Between April and June 2014, a single long-range wind Doppler lidar was deployed 1.75 km South-West of the Lysefjord Bridge. The PPI mode was applied at three elevations, covering the heights of 30.2 m, 60.7 m and 103.6 m at the bridge location. The azimuth sector from 13? to 63? (see Fig. 3) was monitored in steps of 1? per 0.2 second, giving a resolution of 31 m along the bridge. The radial resolution in this mode was 25 m and a maximum scanning distance 2440 m from the lidar. The RHI scans were run at three azimuth angles, targeting the center of the bridge and the areas in the proximity of the pylons. The elevations were varied from 0? to 6? in steps of 0.6?, giving a vertical resolution of 18 m at the bridge site. In May, during a one week period, the LOS measurements with a radial resolution of 25 m were carried out, pointing at the central part of the bridge span.

Based on the short-term wind monitoring system, Cheynet (Cheynet, 2016) performed an assessment of the potential use of Lidars to characterize the wind conditions at the bridge location. Data recorded on 22/05/2014 were analyzed both a flow from N-NE (observed in the morning) and from S-SW (observed in the afternoon and evening).

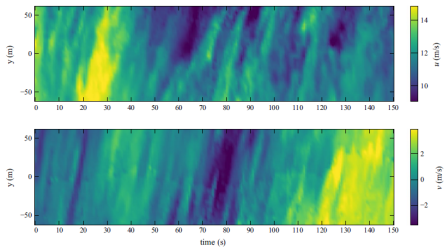

Figure 62: Along-wind (top) and across-wind components (bottom) recorded by the WindScanners from 16:20 on 22 May 2014 (Cheynet, 2016).

Table 26: Coherence coefficients measured on 26/10/2014 and 07/10/2014 for lateral separation along the span (Cheynet et al., 2016a).

Exposure	Component	Decay coefficients			
		c_1	c_2	c_3	c_4
N-NE	v_x	5.0	0.07	1.1	3.3
	w	4.7	0.08	1.2	2.0
S-SW	v_x	6.5	0.02	0.9	6.7
	w	7.9	0.1	1.1	5.4

The high spatial and temporal resolution of the dual lidar system allows the observation of the largest gusts that appear systematically along the entire monitored domain and are skewed with respect to the bridge deck orientation (Figure 62).

The monitored flow is assumed homogeneous if the mean value and standard deviation of wind velocity show limited variations along the bridge deck.

(Cheynet et al., 2016a) - In the following, selected measurement results from May 22, 2014 are presented. For reference, the mean horizontal wind velocity and the associated along-wind turbulence intensities are given in Fig. 4, in which the thick black line indicates the bridge alignment. The two prevailing wind directions, imposed by the fjord topography (from S-SW and NE) are evident. As expected, the turbulence intensity decreases with an increase in wind speed, but also depends on the wind direction, varying throughout the day.

Cheynet et al (Cheynet et al., 2016a) also measured the coherence along the span of a suspension bridge in Lysefjorden. A fitted the measured coherence to a four parameter exponential decay function 21.

The values listed in Table 26 are limited to 10-min data from two days. The mean wind speeds were 17.7 m/s (N-NE) and 13.9 m/s (S-SW), and both are high wind speed conditions for the site, but with different directions. N-NE is wind from North-NorthEast, which is the fjord outlet and S-SW is South-southwest and the fjord with its steep hills rough terrain.

The coherence levels at these two specific storms are compared to the Davenport coherence function with coefficients as given in the Statens vegevesen handbook (Vegvesen, 2015) in Figure 64. The measured coherence levels in the vertical direction is much compared to the handbook, while in the lateral direction it is a better fit. However, there is a distinct difference in the wind in the N-NE storm compared to the S-SW storm. The N-NE has a higher coherence than both the handbook recommendations and the coherence from N-NE.

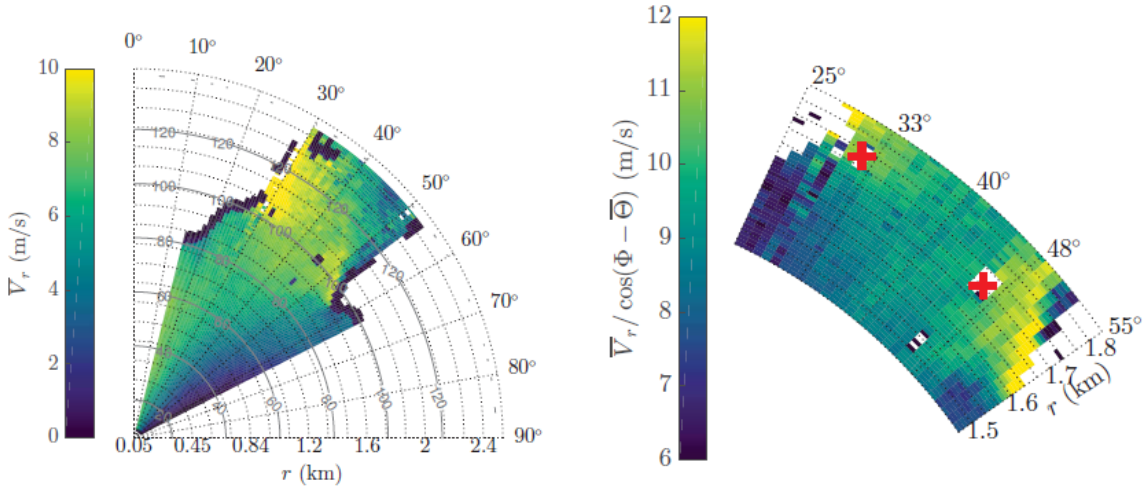

(a) S-SW, recorded on 22/05/2014 between 16:50:22 and 17:25:44. The towers are shown as thick crosses.

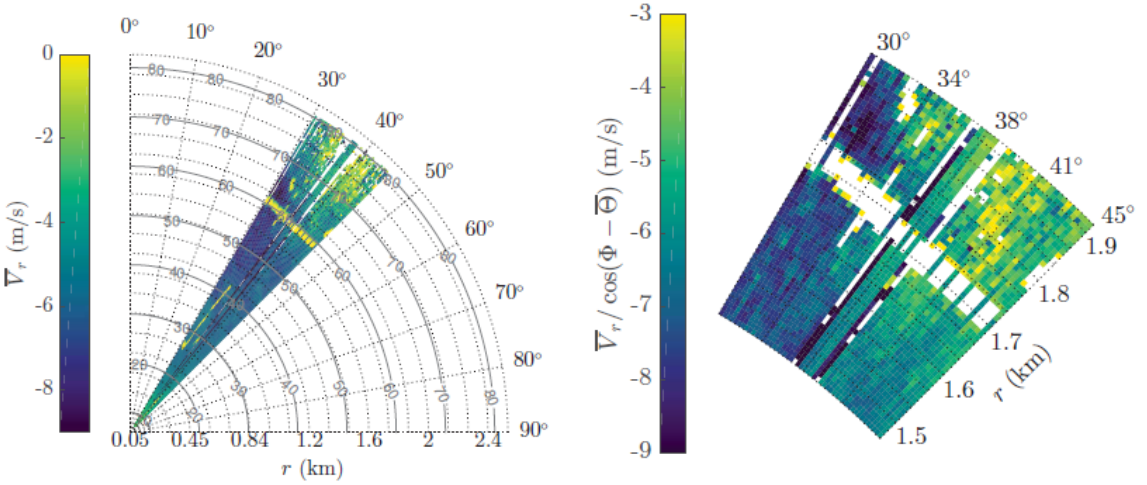

(b) N-NE, recorded on 22/05/2014 between 08:30:03 and 9:13:16. The deck is visible as a white strip for r = 1.7 km.

Figure 63: Mean along-beam wind velocity derived from a PPI scan (Cheynet, 2016).

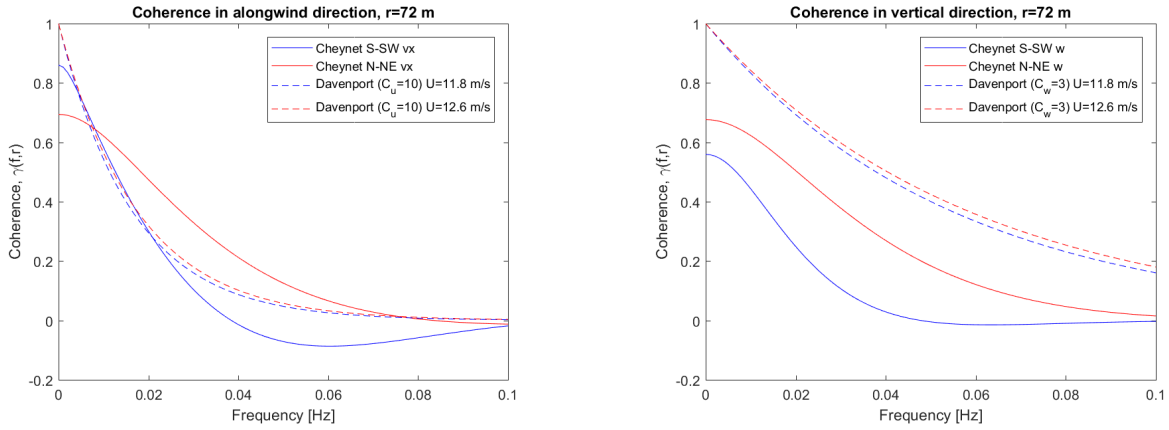

Figure 64: Comparison of the coherence values from Cheynet et al (Cheynet et al., 2016a) and the Davenport coherence function in the Handbook N400 from Statens vegevesen(Vegvesen, 2015)

Table 27: Summary Lysefjord

Category	Parameter	in Report	References
SOURCES			
Measurements	Anemometers	Fig. 56	
	Short-range lidars	Fig. 61	()
	Long-range lidars	Fig. 61	()
Simulations			
IN HOMOGENEOUS AREA			
Flow homogeneity	Long-range lidar	Fig. 63	(Cheynet, 2016)
Long-term statistics	Hindcast		
	Wind roses	Fig. 57	(Cheynet, 2016)
	Turbulence intensity	Fig. 57, Tab. 24	(Cheynet, 2016)
	Dominant wind directions		
	Return periods		
Short-term statistics	Integral length scales	Fig. 58	(Cheynet, 2016)
	Wind spectrum	Fig. 59	(Cheynet, 2016)
	Horizontal coherence	Fig. 60, Tab. 25	(Cheynet, 2016)
		Tab. 26	(Cheynet et al., 2016a)
	Vertical coherence		
AT OTHER LOCATIONS			
Long-term statistics	Hindcast		
	Wind roses		
	Turbulence intensity		
	Dominant wind directions		
	Return periods		
Short-term statistics	Integral length scales		
	Wind spectrum		
	Horizontal coherence		
	Vertical coherence		

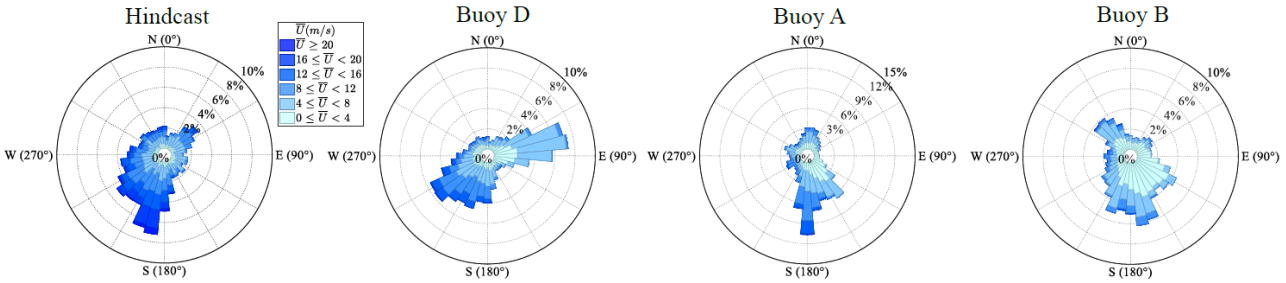

Figure 65: Mean wind speed wind rose recorded from October 2016 to December 2017.

5.4.3 Sulafjord

(Wang et al., 2018b) - Due to the complex topography in the fjord, it is difficult to transfer the wind measurements from the buoys (4.1 m above the sea level) to the bridge deck elevation and above. The wind measurements recorded 4.1 m above the sea level have been transferred to the elevation of 10 m to be comparable with the hindcast data, assuming the log wind profile. The roughness length which is chosen as 0.0002 m, considering less severe waves in the fjord than offshore.

Comparison of the time series for mean wind velocity and direction for the period October 2016 to December 2017, it is obvious that the offshore wind and is well correlated with the wind in the fjord, especially for the strong wind events (Wang et al., 2018b). Figure 65 presents the wind roses for the four sites.

(Wang et al., 2018b) - The offshore wind rose shows more contribution following the coastline orientation, from south-southwest and northeast, and a correspondingly lower western exposure. The wind distribution in the fjord is different from offshore and varies from site to site. Referring to the buoy locations, it seems reasonable that the wind at Buoy D aligns with the coastline of the island Hareidlandet. The Buoy A is mostly exposed to the wind from the south and south-southeast where there is a larger fetch along the fjord, and the wind is sheltered by the islands to the north, west and east. At Buoy B, the northern wind has been diverted to be align with the fjord and the southern wind has a larger spreading and with considerably lower velocities compared to that at Buoy A.

Figure 66: In both storms, the wind shifts from W to N direction. On 16 Dec 2016, the shift in wind direction occurs simultaneously at all locations while a delay of about 10 hours occurs on 17 Nov 17. Could the surface pressure map explain that delay?

In her workshop presentation, Brigitte Furevik mentioned SWAN simulations at Sulafjord in which the wind input was obtained from Kjeller Vindteknikk hindcast with WRT (500 m x 500 m). Figure 67 illustrate the impact of the topography on the local wind at Sulafjord.

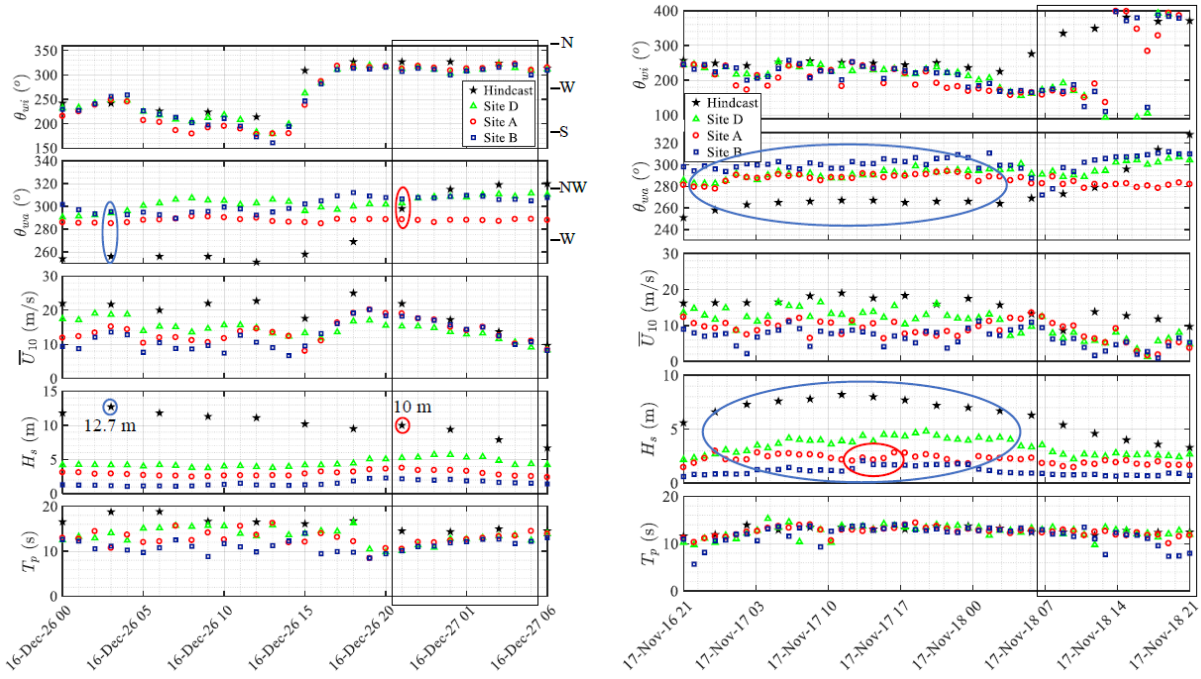

(a) Storm 26 Dec 2016 (b) Storm 17 Nov 2017

Figure 66: Comparison of the wind and wave conditions between the measurement and the hind cast data for two storm events at Sulafjord (Wang et al., 2018b).

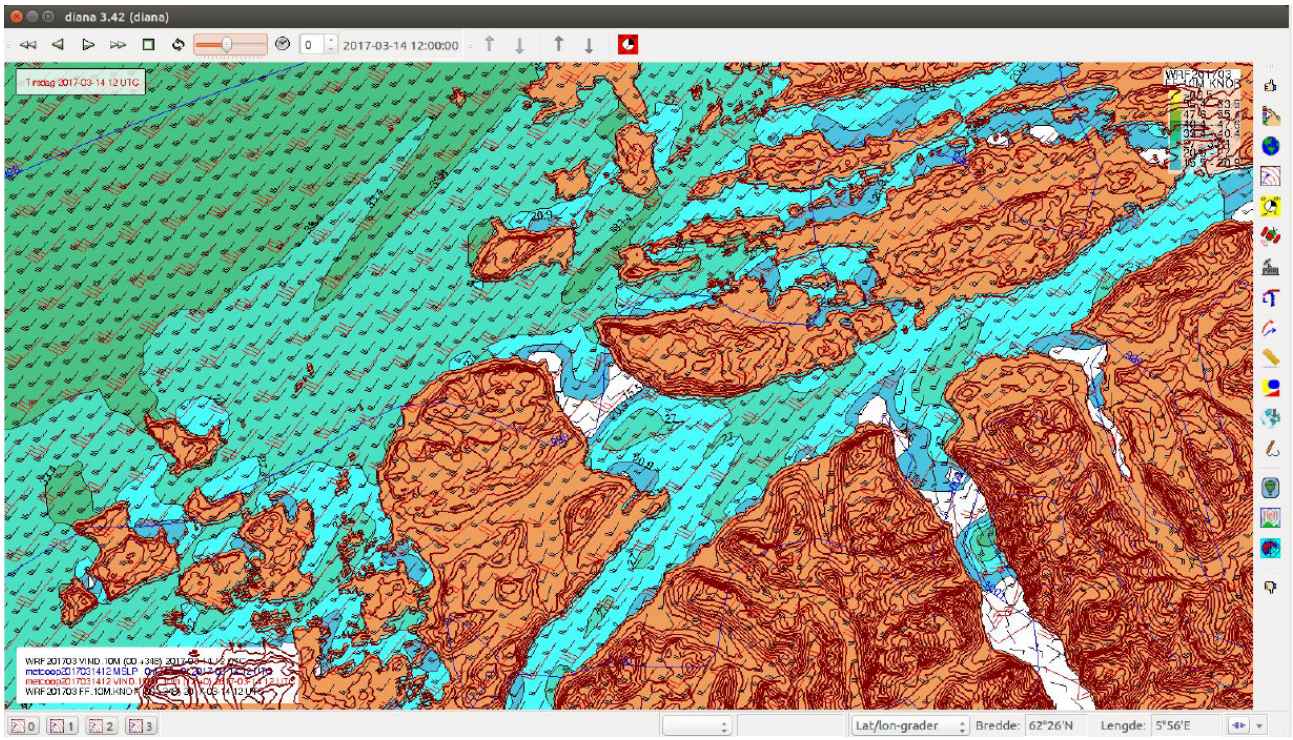

Figure 67: Influence of the topography on the wind at Sulafjord.

Table 28: Summary Sulafjord

Category	Parameter	in Report	References
SOURCES			
Measurements	Buoys	Fig. 5	(Wang et al., 2018b)
Simulations			
IN HOMOGENEOUS AREA			
Flow homogeneity	WRF simulations	Fig. 67	Met workshop
Long-term statistics	Hindcast		
	Wind roses		
	Turbulence intensity		
	Dominant wind directions		
	Return periods		
Short-term statistics	Integral length scales		
	Wind spectrum		
	Horizontal coherence		
	Vertical coherence		
AT OTHER LOCATIONS			
Long-term statistics	Hindcast		
Long-term statistics	Hindcast	Fig. 65	(Wang et al., 2018b)
	Wind roses	Fig. 65	(Wang et al., 2018b)
	Dominant wind directions		
	Return periods		
Short-term statistics	Integral length scales		
	Wind spectrum		
	Horizontal coherence		
	Vertical coherence		

5.5 Identified gaps

5.5.1 Wind description

The traditional way of describing the wind field for structural engineering purposes is limited by the flow assumptions of stationarity and homogeneity.

Long term statistics Long term statistics, which are used for obtaining wind roses and identifying extreme winds corresponding to different return periods for each wind sector, can't be obtained from measurements which are only performed for short periods of time since it is not possible to assess whether the observed conditions represent e.g. 10, 100 or 10 000-years conditions. Engineering projects does not have time to wait for records over a sufficiently long period, and have to rely on simulations. In flat terrain (offshore or onshore), hindcast analysis such as NORA10 can be used to obtain long-term statistics. However, the spatial resolution used in the NORA10 analysis does not provide accurate flow description in complex terrain such as coastal Norway. It is therefore recommended to perform a downscaling of a mesoscale hindcast to a microscale level for each region of interest.

(Johansen, 2016) - A related, but different riddle concerns what will be the normal and extreme weather 100 years ahead. This reflects not only stochastic uncertainty due to natural variations, but also epistemic uncertainty due lack of knowledge related to climate change. [...] This makes robustness and flexibility critical for the maturity of the concepts in a 100-year life cycle perspective.

Non-homogeneity The models presented in Section 5.2 for short-term statistical description of the wind field have been developed under the assumptions of stationarity and homogeneous flow. In Norwegian fjords, due to the steep topography and abrupt roughness changes, the flow cannot be considered as homogeneous and those models might no longer be appropriate. Due to the strong influence of the local topography unique to each site of interest, it is challenging to derive a generalized model to describe wind turbulence. As pointed out by (Wang et al., 2017a), it is therefore required to find an alternative way to describe the wind field in the region of interest. As a generalized approach to characterizing the wind flow, it is suggested perform the following analyze for each wind sector and for each wind speed:

- Extract the mean wind velocity distribution from a corresponding event in the hindcast analysis
- Extract the short term statistics of wind from the wind measurements at an occurrence of a wind event as close as possible to the target wind condition. These short term statistics should be extracted at as many locations as possible, at the height of interest for engineering purposes. If another height must be used, the local mean wind velocity profile predicted in the hindcast should be used for extrapolation at the height of interest.

Due to the non-homogeneity of the surrounding terrain, it can't be assumed that the wind description will be identical from one wind sector to another and the wind characterization process must be performed for each wind sector and all relevant mean wind speeds (Cheynet et al., 2016a).

Low frequency content in wind spectra Since the recording of a wind event must be stationary in order to extract its short term statistics without introducing error, samples of a duration of 2 to 3 hours are required to evaluate the spectrum in the low frequency range. However, since the atmosphere is permanently evolving, it is rare to observe so long stationary periods. According to (DNV, 2007), since it cannot always be relied upon that the stochastic wind speed process remains stationary over time intervals of the order of 2 to 3 hours, the wind spectrum approach cannot necessarily be utilized for wind loads on structures, whose natural frequencies are near the limiting frequency of 1/2400 Hz of the wind spectrum.

Wind spectra for storm conditions Empirical spectra are generally based on measurements performed in non-storm conditions due limited amount of data available above certain wind speeds. (**?**) have shown the variability of the wind spectrum to wind speed. It might therefore not be appropriate to use model spectra for wind speeds above the ones on which they are based.

Wave effect on wind field It is well known that waves results from wind, but little is still known about the impact that waves have on wind turbulence. Waves behave as dynamic roughness. They can have different shapes and travel in various directions relative to the wind. The relations between wave parameters and wind turbulence have been only studied by a few and it is still unclear up to which heights are the wave effects perceived in the wind field. It is recommended to deepen the literature study in this direction and to perform additional studies to document the wave effect on the wind field.

(ApS, 2018)

5.5.2 Turbulence generators

Non-homogeneity In their current implementation, non-uniform wind statistics (horizontal wind shear, non-uniform turbulence intensity, vertical dependence of the wind spectra) cannot be given as input in turbulence generators. It is recommended to implement a turbulence generator that can take as input non-uniform wind statistics as an interpolated function between control points.

Grid In their current implementation, the grids used in turbulence generators are composed of points that are uniformly distributed in space in an orthogonal fashion. The time dimension of the box is also proportional to the natural frequency of the structure. When studying large structures with long natural period, the resulting grid becomes very large resulting in heavy computational needs. It is recommended to implement an option for non-uniform grids in turbulence generators in order to reduce the amount of points in locations where they are not relevant as well as a possibility to map the points to the structure, allowing then to have points that follow the curvature of the structure of interest.

6 Current modelling in coastal area

6.1 Relevant physical current phenomena in coastal area

Models of the ocean circulation try to reproduce the large scale, three-dimensional flow field within an ocean basin. The equations are based on the Navier-Stokes equation, which in general form may be written:

$$\boldsymbol{a} = \boldsymbol{b} + \boldsymbol{c} + \boldsymbol{g} + \boldsymbol{f_{fric}} + \boldsymbol{f_{tide}} \tag{22}$$

where

$\boldsymbol{a}$ = acceleration
$\boldsymbol{b}$ = pressure
$\boldsymbol{c}$ = Coriolis
$\boldsymbol{g}$ = gravity
$\boldsymbol{f_{fric}}$ = friction (wind stress, topography, stratification)
$\boldsymbol{f_{tide}}$ = tides

The Navier-Stokes equation states that the ocean currents are a result of the combined effect of pressure gradients, the Coriolis force, gravity and frictional and tidal forces.

Introducing the assumption of hydrostatic balance, the vertical term of the Navier-Stokes equation reduces to

$$g = -\frac{1}{\rho}\frac{\partial p}{\partial z}, \quad \text{or} \quad p = p_0 - \bar{\rho} g z \tag{23}$$

where p = pressure, p_0 = pressure at the surface and $\bar{\rho}$ = density (averaged)

Then, in the horizontal, the ocean current is a result of three driving forces:

1. Pressure gradients, $\boldsymbol{b} = -\frac{1}{\rho}\nabla p$
2. Wind induced, frictional surface stress, $\boldsymbol{f_{fric}} = \boldsymbol{f_{wind}} = \frac{\partial}{\partial z}(-\tau/\rho_s)$,
   where τ = wind stress and ρ_s = surface density
3. Tidal forces, $\boldsymbol{f_{tide}}$

And there are three *steering* agents:

1. Coriolis force, $\boldsymbol{c} = -f\boldsymbol{k}x\boldsymbol{v}$
   where f = Coriolis parameter ($f = 2\Omega \sin\theta$, where Ω = angular speed of the Earth's rotation (=$0.7292 \cdot 10^{-4} s^{-1}$) and θ = latitude) and $\boldsymbol{v}$ = current velocity
2. Frictional forces (against topography)
3. Stratification (density differences hamper free circulation)

This implies that current velocity may be written as

$$\boldsymbol{U_{total}} = \boldsymbol{U_{press}} + \boldsymbol{U_{wind}} + \boldsymbol{U_{tide}} + \boldsymbol{\Delta U_{Coriolis}} + \boldsymbol{\Delta U_{friction}} + \boldsymbol{\Delta U_{\Delta\rho}} \tag{24}$$

It is only the three driving forces (pressure gradients, wind and tides) that can create, sustain and speed up ocean currents. The three steering agents (Coriolis, friction and stratification) deflect and slow down the currents.

6.1.1 Wind induced currents

A wind blowing over the ocean transfers energy to the sea surface. Part of this energy is used for mixing, the rest builds waves and currents. As a rule of thumb, the wind induced surface current is approximate 2% of the wind at open sea. A persistent fresh breeze (10 m/s) should then generate a fully developed wind current of 20 cm/s. This might be reasonable when it comes to homogeneous, open seas with ”unlimited” fetch. However, in the Norwegian coastal area and fjords the direct wind current can be both stronger (due to stratification) and weaker (due to restricted fetch).

In less stratified waters, as the open sea, most of the energy is used to mixing and less to acceleration. The surface layer then homogenizes and grows in thickness. However, a strong stratification reduces the mixing and a larger part of the energy is used to accelerate the surface water.

The actual wind induced current speed also depends on the kind of stratification that exists. For a two-layer system where two homogeneous slabs are separated by a strong pycnocline (typical estuary or fjord type), the wind mixing will entrain water from the lower layer to the upper layer, gradually *weakening* the pycnocline (Fig. 68, left). When the pycnocline becomes weaker, more of the wind energy is used for mixing than for current acceleration. Under special conditions, when the initial gradient Richardson numbers ($Ri_g \lessapprox 4/3$), a tail wind causes the slab velocity of the upper mixed layer to decrease.

For a more linear density profile, the condition is opposite. The entrainment now creates a well-mixed upper layer separated from the lower layer by a well-defined pycnocline. Further mixing and deepening of the upper layer, now causes a *strengthening* of the pycnocline (Fig. 68, right). When the pycnocline becomes stronger, more of the wind energy is used for acceleration, less for mixing.

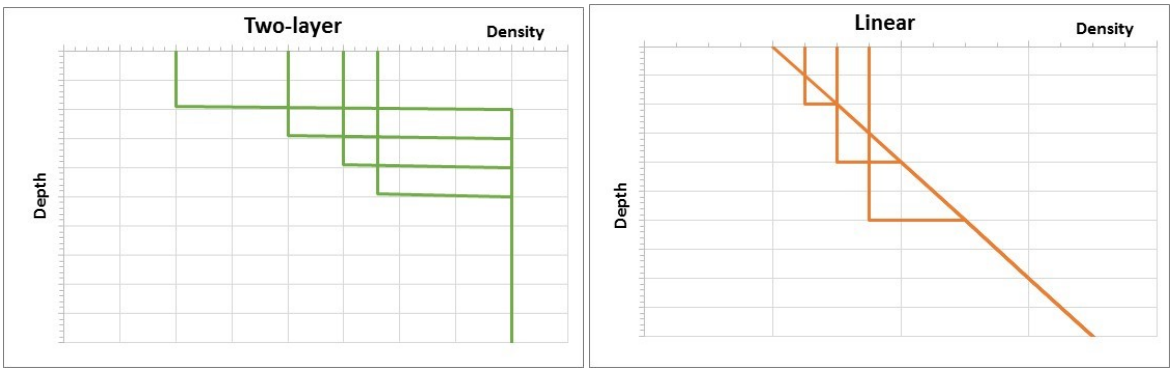

Figure 68: Persistent winds deepen the well mixed upper layer. For a two-layer system (left) the pycnocline weakens during the windy period, increasing the entrainment across it. For a linear stratification (left) the pycnocline strengthens, decreasing the entrainment process.

The direct wind induced current speed thus depends not only on wind strength, fetch and duration but also to a considerable extent on the actual stratification and how the pycnocline changes during the wind induced entrainment process.

The wind induced current develops when the wind stress pulls on the sea surface. The initial, idealized wind current profile will then be linearly decreasing from its maximum value at the surface to its minimum at the pycnocline. After a while the wind mixing of the upper layer homogenize also the wind current (Fig. 69).

The winds may also give rise to another, indirect type of wind current, called stow-up currents. These are consequential, resulting currents that may break out when stowed up water in bays and fjords, caused by persistent winds, let go. Since these currents are pressure-driven they are discussed in more detail in next chapter.

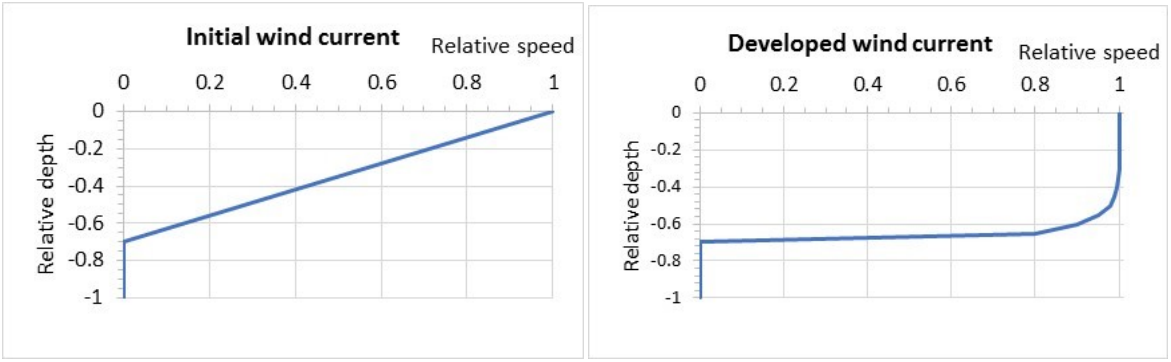

Figure 69: The initial wind current speed profile is linear. Wind mixing makes it more constant through the upper well mixed layer.

6.1.2 Pressure driven currents

In the same way as high and low barometric pressures create winds in the atmosphere, hydrostatic pressure gradients in the ocean will create currents, initially directed from areas with high pressure to areas with low.

There are numerous currents of pressure driven origin. The global thermohaline circulation, the estuarine circulation in fjords, the Norwegian Coastal Current and the Gulf Stream are all examples of pressure driven currents. They are stochastic and often less predictable.

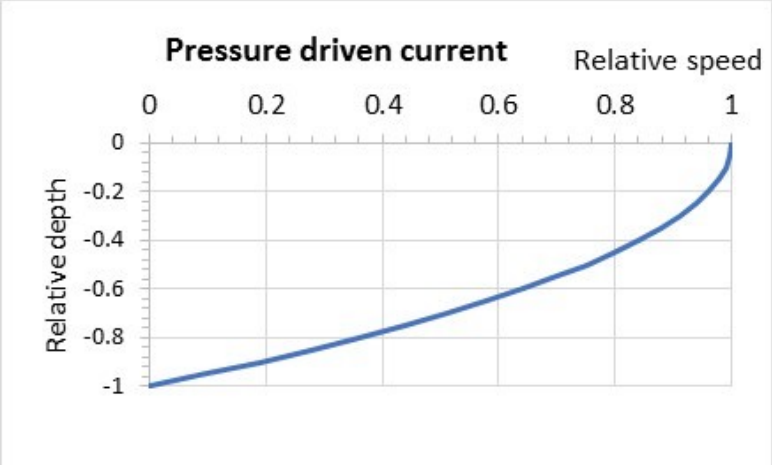

Figure 70: The pressure driven current profile is hyperbolic (idealized).

6.1.3 Stow-up currents

A special attention should be drawn to the previously mentioned stow-up currents. They may be initiated when a strong and persistent wind blows inward into a fjord and builds up a higher water level at the inner part of the fjord. If the wind strength suddenly drops or changes direction, the stow up loosens and a strong outward return-current occurs in the upper layer. The strongest currents in many Norwegian fjords are due to such stow-up currents. They may be generated internally in the fjord system but may also be due to external events. One of the strongest stow-up currents that may influence most of the Western and Southern Norway (and even part of the North Sea with large and strong eddies) may occur after a long period of strong winds from southwest in Skagerrak stowing up water in to the Oslofjord. If the wind suddenly ceases, an outburst in the Norwegian

Coastal Current may break out. The outbursts can be strong ($\approx$ 1 m/s), but they are short-lived (typical 12-18 hours) and occasional (typical once or twice a month).

During outbursts in the Norwegian Coastal Current, the stronger currents often branch into the fjord systems on its way around the coast. Due to its density, the fjord inflows are usually located below the outflowing surface current. For instance, an outburst in the Norwegian Coastal Current (Figure 71), estimated to 280 000 m^3/s, was recorded by current meters one - two days later as an inflow at 10-20 m depth at three different locations in the Boknafjord system. The outbreaks in the Norwegian Coastal Current contribute significantly to the general water exchange in the Norwegian fjords.

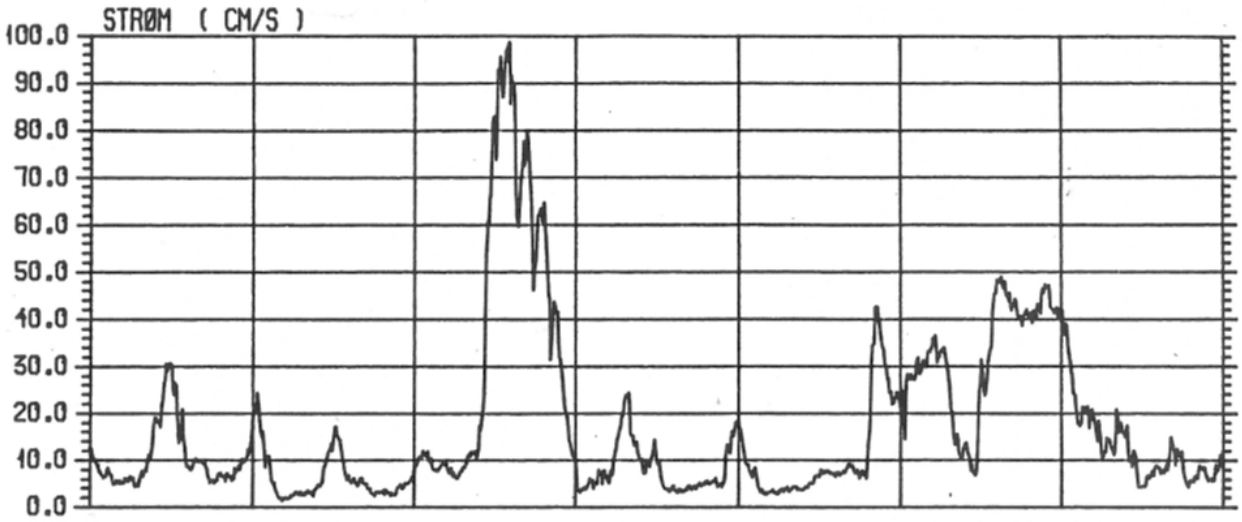

Figure 71: One-week timeseries of an outburst in the Norwegian Coastal Current recorded at 5 m depth off Randaberg (Håsteinfjorden) in August 1986.

6.1.4 Estuarine circulation

The Norwegian fjords are characterized by one or more river outlets. Creating an outward pressure gradient, the freshwater spreads out on the fjord surface. On its way, the freshwater mixes with the underlying saline water. This process (entrainment) creates a gradually more saline outward brackish surface flow.

To compensate the loss of salt and mass, an inward (pressure driven) current is created below the outward surface current. This current is called compensation current and is generally significant weaker than the outward current above it.

This general picture is 'disturbed' by the Coriolis force, caused by the Earth's rotation (see Ch. x.x), pulling all movement in the northern hemisphere toward the right. In a fjord, the outward current is dragged towards its right-hand shore, while the inward compensation current is dragged towards the opposite side (which is the right-hand shore for this current). If the fjord is wide enough, the inward compensation current may break up to the surface. This may lead to a horizontal shear currents with the strongest surface currents on the outward right-hand side and the slowest currents (or opposite directed) on the other side.

6.1.5 Tidal currents

As the name suggests, tidal currents are generated by tides. Tides are long and slow waves created by the gravitational pull of celestial bodies (especially the moon and the sun) on the earth's surface. The gravitational

force is proportional to the mass of the celestial body (M) and the mass of the earth (m) and inverse proportional to the distance, r, squared; $\boldsymbol{f_{tide}} \propto M \cdot m/r^2$. Since the moon is so much closer to the earth than the sun, the moon's pull has more influence on the tides than the sun.

Each of the tidal constituents follow the (harmonic) wave expression $\eta(t) = A \cdot \cos(\omega t + \phi)$, where

η is the tidal elevation at a specific time
A is the amplitude of the constituent
ω is the speed of the constituent (the rate of change in phase), and
ϕ is the phase of the constituent

The various celestial bodies and their accompanying tidal frequencies give rise not only to diurnal and semi-diurnal constituents, but also terdiurnal, long periodical as well as shallow water constituents. The constituents with most impact (ranged by their potential amplitudes within each category) are:

Table 29: Most important constituents.

	Symbol	Name	Period (hours)
Semi-diurnal	M_2	Principal lunar	12.42
	S_2	Principal solar	12.00
	N_2	Larger lunar elliptic	12.66
	K_2	Luni-solar semi-diurnal	11.97
Diurnal	K_1	Luni-solar diurnal	23.93
	O_1	Principal lunar diurnal	25.82
	P_1	Principal solar diurnal	24.07
	Q_1	Larger lunar elliptic	26.87
Long periodic	Mf	Lunar fortnightly	327.90
	Mm	Lunar monthly	661.30

Tidal currents are mainly depth-constant except close to the bottom where frictional forces are present.

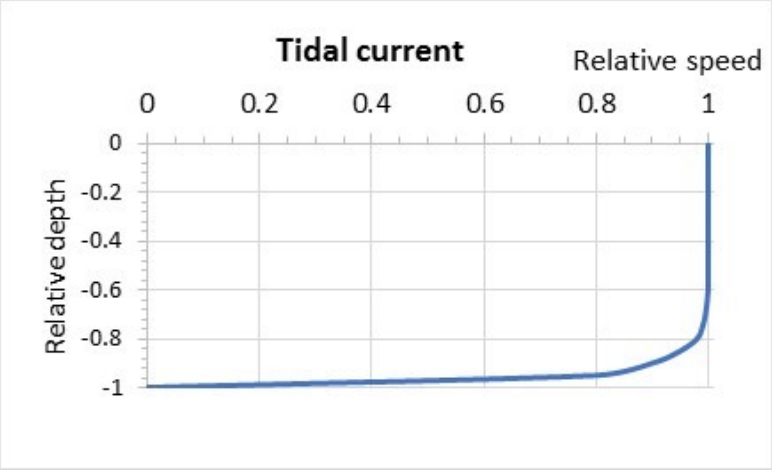

Figure 72: The tidal current profile is almost constant with depth (except for the bottom layer).

There are two types of tidal flows. On the open sea the tide appears as a Kelvin wave having its maximum current at high tide and low tide. In fjords the tide behaves as a standing wave having its maximum at mean sea level. Along the coast the tidal current is a transition between these two types of flow.

Tidal inflow and outflow of fjords with large surface area and a narrow and shallow inlet give strong tidal currents. Such inlets are called tidal sounds and the strongest current velocities in Norway are found in these sounds. The top five are (probably):

- Saltstraumen near Bodø– alleged to be up to 10 m/s under special conditions
- Moskenesstraumen (Malstraumen) in the outer part of Lofoten – estimated up to 5 m/s
- Sørstraumen in Kvænangen – up to 4 m/s
- Straumen at Inderøy – up to 3.5 m/s
- Rystraumen at Tromsø– up to 3 m/s

It is straight forward exercise to make an estimate of the current speed in a tidal sound by using the so-called tidal prism approach:

The tidal flux in and out of the sound:

$$Q = A_{surf} \cdot \Delta h/\Delta t = U \cdot A_{sill} \Leftrightarrow U = \frac{A_{surf}}{A_{sill}} \cdot \Delta h/\Delta t \tag{25}$$

where A_{surf} = surface area of the inside fjord
A_{sill} = cross-sectional area of the inlet sound (sill)
Δh = tidal height (between high water and low water)
Δt = tidal period (6 h 12.5 min)
U = mean tidal current speed in the inlet sound

For Saltstraumen we have the following estimates for mean spring tidal height (MHWS – MLWS):

A_{surf} = 250 km^2
A_{sill} = 3 350 m^2
Δh = 1,48 m incl. tidal choking effect (ref. sehavniva.no for Rognan)
$\Rightarrow$ Mean tidal current for at mean spring: 4.9 m/s
$\Rightarrow$ Maximum tidal current for tidal spring: 4.9 m/s $\cdot$ ½ π = 7.8 m/s (16 knots)

6.1.6 Friction and stratification

Frictional forces and stratification are probably more self-explanatory agents. The thermohaline circulation is driven by global density gradients created by surface heating/cooling and freshwater runoff, and as such a part of the stratification term, $\Delta U_{\Delta\rho}$. The large-scale thermohaline circulation is generally ignored in local studies.

6.1.7 The Coriolis force

More mysticism is probably related to the Coriolis force. The effect of Coriolis is to pull all movement in the northern hemisphere toward the right (and toward the left in the southern hemisphere).

For an intuitive explanation of the Coriolis force, consider an object moving northward in the northern hemisphere. The object follows the surface of the Earth, and viewed from the outer space, it looks like the object does not move toward due north but has an eastward motion along with the surface of the Earth. This deflection to the right is called the Coriolis effect. In this sense, the Coriolis force is not a real force, it is an ”as if” force. It looks as if the moving object is deflected toward the right (northern hemisphere), but actually it is only the Earth that performs its cyclonic rotation.

Table 30: Relation between some fjords and maximum current to be influenced by Coriolis.

Location	Latitude (°N)	Typical width (m)	Coriolis parameter, f (10^{-4} s^{-1})	Max current speed for deflection (cm/s)
Bjørnafjorden	60,0	7 300	1.26	92
Sulafjorden	62,4	4 000	1.29	52
Altafjorden	70,0	5 500	1.37	75

In narrow fjords the Coriolis effect may be ignored, but the wider the fjord is, the more important the Coriolis effect will be. When the width of the fjord exceeds the Rossby radius of deformation, a significant deflection of the flow may be expected. The Rossby radius, L_r, is given by $L_r = U/f$

where U = current speed and f = Coriolis parameter ($f = 2\Omega \sin\theta$, where Ω = angular speed of the Earth's rotation (= 0.7292· 10^{-4} s^{-1}) and θ = latitude)

The correlation between latitude, width of fjord, Coriolis parameter and maximum current speed for Coriolis to be important are given for some selected locations in the table below.

From Table 30, we may read that in Bjørnafjorden all currents below 92 cm/s are supposed to be significantly deflected due to the Coriolis effect. In Sulafjorden this limit is at 52 cm/s.

6.2 Current measurements and analyses

6.2.1 Measurements

The classical way to do current measurements has been to deploy a current meter with a rotor or anemometer for speed measurements and a vane for recording the current direction. Following the meteorological convention for wind measurements, the oceanographic current measurement is usually an averaged value over 10 minutes. For atmospheric wind both scalar and vector averaging are used depending on the application and nature of the wind. For ocean currents vector averaging is common, due to the generally smaller variance of the current direction. To obtain the vector-averaged speed and direction, the orthogonal components are summed and vector averaged at the end of the averaging period. When turbulence data are required, the measurement interval is much shorter.

The rotor current meters are still in use, but hydroacoustic techniques are gradually taking over. The acoustic instruments are based on the Doppler shift technology. They could be single point current meters or profilers - both vertical and horizontal. The newer current recorders usually have several user-defined applications for customizing the measurements to special requirements. Some acoustic current meters may be configured to measure for a particular period (say 1 minute), then to stay passive for another period (e.g. 9 min). A similar effect occurs with the option to choose between "spread mode" where the acoustic signals are evenly transmitted over a predetermined interval, and "burst mode" where the sampling period is concentrated to a shorter part of the same interval. The advantage is to reduce battery consumption, but comparative concepts like '10 minutes averaged values' will not necessarily have the same meaning.

Standardization or guideline for recommended practice with respect to ocean current measurements will probably soon be a matter of necessity.

For the Ferry-free E39 project at Møre, the current measurements given in Table 31 are in operation or planned for at the time being.

Table 31: Current measurements for E39 in Møre.

Station	Location	Position		Aprox. water	Measurement	
		Latitude	Longitude	depth (m)	started	finished
A	Sulafjorden	62° 25,60'	06° 02,61'	370	13. Oct 2016	ongoing
B	Sulafjorden	62° 24,23'	06° 04,77'	310	13. Oct 2016	ongoing
C	Sulafjorden	62° 23,52'	06° 03,01'	365	27. Apr 2017	ongoing
D	Breisundet	62° 26,71'	05° 55,80'	300	14. Oct 2016	ongoing
E	Storfjorden/Hjørundfjorden	-	-	-	not started	-
F	Vartdalsfjorden	62° 13,20'	05° 53,91'	265	xx. Oct 2017	ongoing
G	Halsafjorden	63° 05,15'	08° 09,45'	430	18. Oct 2016	ongoing
G1	Halsafjorden	63° 05,21'	08° 08,56'	140	05. Apr 2017	ongoing
G2	Halsafjorden	63° 05,37'	08° 09,96'	180	04. Apr 2017	ongoing

6.2.2 Analyses

Depending on the objective of the data acquisition of ocean currents, the data could be analyzed for specific purposes, as 'duration of events' and 'directional correlation'. However, two analyses are more commonly in us than others and should be reviewed in more detail, and that is 'harmonic analysis' and 'extreme value analysis'.

Harmonic analyses

The ocean tides - as well as their consequence, the tidal currents - are deterministic and persistent, and the sum of individual oscillatory components caused by the various tidal constituents. The practical – or experimental – approach of harmonic analysis is to collect tidal data (height or currents) and to fit the data to a sum of harmonic waves describing the most common tidal constituents (see Table 29.)

The mathematical technique is known as Fourier transform, and the study is called 'harmonic analysis'. When the amplitude and phase of the individual tidal components are determined, the tidal curve (both height and current) can be determined for any time. The tide is deterministic.

Software programs for harmonic analyses are commercial available with a variety of number of constituents included. They may also include some of the shallow water constituents which arise from distortion of main constituent tidal oscillations in shallow water. They could of course be skipped for deep water analyses.

When running harmonic analysis, it is important to be aware of and deal with two aspects:

1. The maximum number of constituents possible to include in the harmonic analysis, depends on the length of the recorded time series. Example: The major constituents covering both tidal spring and nip conditions – M_2, S_2, N_2, K_1 and O_1 – require a timeseries of 662 hr (or 28 days).
2. The inclusion of some of the constituents may require the inclusion of other constituents. Example: The analysis of Q_1, depends on the analysis of O_1 which in turn depends on K_1.

Extreme value analysis

To calculate extreme values of currents, statistical extrapolation of the measured data is usually performed. This is done by fitting the measured time series to a known statistical distribution, and then extrapolating this distribution to find expected extreme values for return periods such as 10, 50 and 100 years.

Several variables in nature are composed of both deterministic and stochastic processes. In 6.1 we split the total current into a sum of sub-currents according to the forces generating them. Since the tidal current is deterministic, it will be methodically incorrect to analyse the tidal current from statistical distribution and extrapolation. We therefore remove the tidal current contribution from the time series (based on harmonic analyses).

The residual two driving terms, U_{wind} and U_{press}, contain currents generated by e.g. high pressure / low pressure, upwelling, river run-off, wind and other meteorological conditions. These residual current elements – gathered as U_{res} – are caused by stochastic processes and meet the conditions for statistical extrapolation.

How likely is it that different current extremes occur at the same time? For instance, what is the combined probability that an extreme residual current created by strong winds and low pressure occurs at the same time as a spring tide current, creating a storm surge? To be on the safe side, the two extreme values are often summed up. But since spring flood and storm surge are two independent events, this gives a strongly conservative estimate.

The mathematical solution for the combined probability of a joint event determined from two independent variables can be described as follows:

A statistical variable, z, is defined as the sum of two independent statistical variables x and y. The probability distribution for x is denoted g, and the probability distribution for y is denoted h.

g and h are given by $g(x) = dG/dx$ and $h(y) = dH/dy$, where G and H are the distribution functions of the two variables x and y. The probability, P, for exceeding a particular z-value, $z = a$, is then given by

$$\begin{aligned} P(a) &= \int_{-\infty}^{\infty} \int_{a-x}^{\infty} g(x)\, h(y)\, dx\, dy = \int_{-\infty}^{\infty} g(x) \int_{a-x}^{\infty} \frac{dH}{dy}\, dy\, dx \\ &= \int_{X_{\min}}^{X_{\max}} \left[1 - H(a-x)\right]\, g(x)\, dx \\ &\approx \sum_{X_{\min}}^{X_{\max}} \left[1 - H(a-x)\right]\, g(x)\, \Delta x \end{aligned} \tag{26}$$

Let H describe the residual current distribution U_{res}, and g be the probability distribution for U_{tide} given by the probability of exceeding a particular tidal current speed. H could then be represented by the Weibull distribution for residual water given by

$$H(a-x) = 1 - \exp\left[-\left(\frac{a-x-\epsilon}{\theta}\right)^{\gamma}\right] \tag{27}$$

where

γ = shape parameter
θ = scale parameters
ϵ = location parameters

which again provides:

$$P(a) \approx \sum_{X_{\min}}^{X_{\max}} \exp\left[-\left(\frac{a-x-\epsilon}{\theta}\right)^{\gamma}\right]\, g(x)\, \Delta x \tag{28}$$

Thus, the combined probability, P, for exceeding a particular z-value, $z = a$, is given by the product of the Weibull distribution for residual current and the probability distribution, $g(x)$, of the tidal current.

6.2.3 Shear flow correlation

Vertical shear flow occurs when the current at two adjacent measurement depths in the same position and at the same time has opposite direction.

Horizontal shear flow occurs when the current direction on one side of the fjord is opposite to the current direction at the same depth and at the same time on the other side of the fjord.

Both incidents may have unwanted load effects and should be quantified, e.g. as joint (relative) frequency tables of current directions. In addition, the strength of the current shear (ΔU) should be quantified, e.g. as histograms.

6.3 Numeric ocean models -A short description of 5 models

Ocean models, or general circulation models, are numerical models with a focus on the properties of oceans and their circulation. The models solve the same set of primitive equations for motion of a fluid element on a rotating sphere, and differs mainly in numerical methods for solving the equations and in coordinate system used. Most models, if not all, are written in Fortran F90. All the models can be run in parallel on many processors on super computers. All models have opportunity to include sea ice, biology and assimilation of measurements, and those extra options will have differences between them as the ocean models do.

Ocean models play a large role in aiding our understanding of the ocean's influence on weather and climate. There are many ocean models in use today, and five of them are briefly described here. Some other commonly used models are listed at the end of the document. The first three models described, ROMS, NEMO and FVCOM, are open source models, with freely available source code. The last two models, SINMOD and MIKE3 are not freely available. MIKE3 is a commercial model with licences for purchase, and SINMOD is a research and development model for SINTEF.

6.3.1 ROMS

"Regional Ocean Modelling System" (ROMS, http://myroms.org) is a three-dimensional current model developed by Rutgers University, University of California Los Angeles and contributors worldwide (Shchepetkin and McWilliams, 2005). Sigma coordinates in the vertical and orthogonal curvilinear coordinates on a staggered Arakawa C-grid in the horizontal is used. Both Cartesian and spherical coordinates can be used. ROMS has been widely used globally for the last $\sim$15 years. There are lots of possibilities in the specification of the model, so the users can choose methods for horizontal and vertical mixing of momentum, turbulence, horizontal advection, lower boundary layer, stability and more.

The terrain-following sigma coordinates enables the model to have the same number of vertical layers both in shallow seas and in the deep ocean, but the trade off is that the topography can not be too steep (like in Norwegian fjords). The result is a smoothed version of the bathymetry in such areas to avoid unphysical currents along the sloping coordinate lines. The model is well suited for large scale simulations. A lot of the data in the former European MyOcean project and the associated web portal was produced with the ROMS model. It is also used in COAWST: **C**oupled **O**cean **A**tmosphere **W**ave **S**ediment **T**ransport Modeling System (Warner et al., 2010).

6.3.2 NEMO

Nucleus for European Modelling of the Ocean (NEMO) is a state-of-the-art modelling framework of ocean related engines that is developed as a collaboration between six European institutes (CMCC (The Euro-Mediterranean Center on Climate Change, Italy), CNRS (The National Center for Scientific Research, France), INGV (National

Institute of Geophysics and Volcanology), Mercator Ocean (France), Met Office (UK) and NERC (Natural Environment Research Council, UK). NEMO is an ocean modelling framework which is composed of ”engines” nested in an ”environment”. The ”engines” provide numerical solutions of ocean, sea-ice, tracers and biochemistry equations and their related physics. The ”environment” consists in reference configurations, pre- and post-processing tools, interface to the other components of the Earth system, user interface, computer dependent functions and documentation of the system.

NEMO allows several ocean related components of the Earth system to work together or separately (i.e ”standalone mode”). It also allows a two-way nesting via the AGRIF software. It is interfaced with the other components of the Earth system (atmosphere, land surfaces, ...) via the OASIS coupler.

OPA is the physical ocean component of NEMO containing the dynamics and thermodynamics. OPA is primitive equation model adapted to regional and global ocean circulation problems down to kilometric scale. Prognostic variables are the three-dimensional velocity field, a linear or non-linear sea surface height, the temperature and the salinity.

In the horizontal direction, the model uses a curvilinear orthogonal grid and in the vertical direction, a full or partial step z-coordinate, or s-coordinate, or a mixture of the two (z* vertical coordinates is also available). The distribution of variables is a three-dimensional Arakawa C-type grid. Various physical choices are available to describe ocean physics.

The range of applications includes oceanographic research, operational oceanography, seasonal forecast and (paleo) climate studies. Used by a large community of users since 2008. The global simulations available at www.marine.copernicus.eu are performed with NEMO.

6.3.3 FVCOM

FVCOM (Finite Volume Community Ocean Model) is developed at The Marine Ecosystem Dynamics Modeling Laboratory at University of Massachusetts-Dartmouth (USA). The model is an unstructured grid, Finite-Volume, primitive equation Community Ocean Model that is well suited for simulating the circulation and ecosystem dynamics from global to estuarine scales, particularly for regions characterized by irregular complex coastlines, islands, inlets, creeks, and inter-tidal zones. The horizontal grid is composed of triangles rather than squares, which ensures a geometric flexibility for a closer fitting to the coastal boundary. The vertical levels are terrain-following (sigma). FVCOM solves the governing equations on Cartesian or spherical coordinates in integral form by computing fluxes between non-overlapping horizontal triangular control volumes.

The model has been set up for small (bay) to global scale. In the global setup, a hybrid coordinate system in the vertical is used with z-coordinates closest to the surface and the bottom, and sigma-coordinates in between. The current version of FVCOM is fully coupled ice-ocean-wave-sediment-ecosystem model system.

It handles grid cells that are wet/dry depending on water level (tides), and this makes it particularly useful where such processes are important, like some estuaries, river outlets and areas of large tidal difference. FVCOM is more costly in terms of CPU time than many other models.

6.3.4 SINMOD

The SINMOD model system is an ocean model with modules for including the ecosystem up to zooplankton (Slagstad and McClimans, 2005). The model has been in continuous development and use at SINTEF since 1987. Horizontally the model uses a structured grid, and z-coordinates in the vertical. Originally developed for the Barents Sea, SINMOD has been used mostly for the Nordic Seas/Arctic Ocean, but can easily be set up anywhere with coupling to a global model (i.e. www.marine.copernicus.eu). SINMOD uses an Arakawa C-type grid like all the other models.

SINMOD has sea ice, sedimentation, and ecosystem integrated, and functionality for including waves (SWAN model) is under development. SINMOD is often used to provide input data to other models developed at SINTEF, like DREAM (particle model) and OSCAR (oil spill).

The model is well suited for regional to local studies, as a global setup is not available.

6.3.5 MIKE3

MIKE 3 is a component of the MIKE by DHI software. It is a three-dimensional hydrodynamic model based on a flexible mesh approach and it has been developed for applications within oceanographic, coastal and estuarine environments. The model is based on the numerical solution of the 3D incompressible Reynolds Averaged Navier–Stokes equations (RANS) invoking the assumption of Boussinesq and hydrostatic pressure approximation. The model is module based, so one buys the modules one need. There is a choice of grids available; single, multiple and flexible mesh. All versions can run on Windows, and the latter can also run on Linux (and hence on a High Performance Computing system).

Mike3 is a commercial model and support is available. There is a wide range of modules available.

HYCOM (Hybrid Coordinate Ocean Model), developed at University of Miami, USA.

POM (the Princeton Ocean Model), developed at Princeton University, New Jersey, USA.

MPI-OM (The Max-Planck-Institute Global Ocean/Sea-Ice Model, Hamburg, Germany).

6.4 Standards and guidelines

As per 7th of June 2018 the MetOcean design basis (SVV, 2017) for currents deals with extreme values and horizontal shear currents. The extreme values are based on modelling results for a period of 2 years and 8 months. The period is short relative to return periods of 100 year (and longer), thus a 20 % increase of these values is suggested as a sensitivity test for the longer return periods.

For inhomogeneous currents - where the current speed and/or direction varies across the fjord – several explicit cases are given, and asked to ”be considered”. The specifications seem to be general and not related to specific measured or modelled data of real current conditions in Bjørnafjorden, as for example: *”The current is constant in or out of the fjord in the south half of the bridge, and constant in the opposite direction in the northern half. The velocity shall be taken as* $^2/_3 \times V_0$*”*, where V_0 is the given extreme value. Since the extreme values are based on modelled current velocities in 2 sections each of 8 positions across the fjord, it would be possible to relate the specific criteria to simultaneous current velocities across the fjord, and thus obtain more realistic conditions of the actual shear currents. This aspect is of course also valid when measured current data are available.

6.5 Internal waves

A submerged tube bridge (and other underwater constructions) may be exposed to internal waves if the water is stratified. Internal waves propagate horizontally like surface waves but at a slower speed due the density difference across the pycnocline being much smaller than at the surface between air and sea. Due to the same reason, the amplitude of an internal wave may be much greater than at the surface. Internal oscillation amplitudes of some tens of meters have been reported. A strong stratification and strong vertical shear flow promote the possible existence of an internal wave.

Governing parameters for internal waves are:

- Depth of pycnocline, h

- Thickness of pycnocline, δ
- Density difference across pycnocline, $\Delta\rho$
- Density gradient, $\dfrac{\partial\rho}{\partial z}$
- Brunt-Väisälä frequency, $N_0\sqrt{\dfrac{-g}{\rho_0}\dfrac{\partial\rho}{\partial z}}$, where g = gravity and ρ_0 = reference density
- Overall Richardson number, $Ri_u = \dfrac{g\frac{\Delta\rho}{\rho_0}h}{(\Delta u)^2}$, where Δu = velocity difference across pycnocline

6.6 Gaps and recommendation

Current measurements

There has been a considerable progress when it comes to ocean current measurements over the last decades. When the acoustic current profiling technique was introduced in the 1980s, a new era of current data acquisition arose. Instead of counting the number of revolutions of a rotor and recording the position of a vane, the field oceanographer had to decide on various setup codes as

- burst mode vs. spread mode
- number of pings
- depth cell size
- number of cells
- blanking distance

and other tracking and system configurations. This has in turn lead to some challenges when it comes to the convention of how to measure ocean currents: as a vectorial average over 10 minutes. It may be difficulty comparing one current velocity with another if they are measured differently.

It is hardly desirable and probably neither necessary nor possible to set up standards for a recommended configuration, the applications and variations are probably too large. But the desire for the highest possible accuracy and quality should be guiding the choices to be made. It is therefore recommended that simple and common guidelines should be established to ensure a common basis for best practice of how ocean current measurements should be performed.

Extreme value analyses

Tidal currents are periodic processes where extreme values have an upper limit depending on the earth's position relative to the moon and the sun. When the amplitude and phase of the individual tidal components are determined (by harmonic analysis), the tidal current (both speed and direction) can be determined for any time. The tidal current is deterministic. To analyse tidal currents from statistical distribution and extrapolation is methodically incorrect.

When the tidal current distribution is removed from the time series, the residual current remains. To calculate extreme values of currents, statistical extrapolation of the residual current data is used. This is done by fitting a given distribution (as Weibull, Gumbel or others) to the measured data, and then extrapolating this distribution to find expected extreme values for return periods as 10, 50 and 100 years. The data used should be independent and (ideally) represent one event with a given duration. An often-used method is to select the highest value over

a given period - typical one, two or three days - and define these maxima as the new data basis. The duration of the event is then uniquely decided, and there are good reasons to believe that the data are independent.

The accuracy of an extreme value analyses highly depends on how good the chosen distribution fits the data. In those cases where the fit to data is not good (in particular for the highest speed values), a truncated distribution should be applied to try to improve the fit. The truncation cut-off value should be determined individually for each data set.

When the extreme residual currents are determined, the result must be combined with the tidal current values. So, what is the combined probability that an extreme residual current created by strong winds and low pressure occurs at the same time as a spring tide current, creating a storm surge? To be on the safe side, the two extreme values are often summed up. However, since the values are independent, this gives a strongly conservative estimate. It can be shown that the combined probability, P, for exceeding a particular z-value, $z = a$, is given by

$$P(a) \approx \sum_{X_{\min}}^{X_{\max}} \left[1 - H(a - x)\right]\, g(x)\, \Delta x, \tag{29}$$

where H describes the residual current distribution (e.g. the Weibull-distribution), and g is the probability distribution for the tidal current given by the probability of exceeding a particular tidal current speed.

It is recommended that some guidelines are established along these lines to ensure a common basis for best practice of how extreme ocean current value analyses are to be performed.

References

(2007). *Recommended Practice DNV-RP-C20 ENVIRONMENTAL CONDITIONS AND ENVIRONMENTAL LOADS*. DET NORSKE VERITAS.

Ahrens, C. D. (2011). *Essentials of meteorology: an invitation to the atmosphere*. Cengage Learning.

Andersen, O. J. and Løvseth, J. (1995). Gale force maritime wind. the frøya data base. part 1: sites and instrumentation. review of the data base. *Journal of Wind Engineering and Industrial Aerodynamics*, 57(1):97–109.

Andersen, O. J. and Løvseth, J. (2006). The frøya database and maritime boundary layer wind description. *Marine Structures*, 19(2-3):173–192.

Andersen, O. J. and Løvseth, J. (2010). Stability modifications of the frøya wind spectrum. *Journal of Wind Engineering and Industrial Aerodynamics*, 98(4-5):236–242.

Antonia, R. and Luxton, R. (1971). The response of a turbulent boundary layer to a step change in surface roughness part 1. smooth to rough. *Journal of Fluid Mechanics*, 48(4):721–761.

Antonia, R. and Luxton, R. (1972). The response of a turbulent boundary layer to a step change in surface roughness. part 2. rough-to-smooth. *Journal of Fluid Mechanics*, 53(4):737–757.

ApS, S. O. H. (2018). Wind model-tests floating bridge step 1 small scale testing. Technical Report SBJ-32-C4-SOH-20-RE-001 RevA, National Public Roads Administration.

Astrup, P. and Larsen, S. E. (1999). *WAsP engineering flow model for wind over land and sea*. Risø National Laboratory Roskilde.

Bendat, J. S. and Piersol, A. G. (2011). *Random data: analysis and measurement procedures*, volume 729. John Wiley & Sons.

Booij, N., Ris, R., and Holthuijsen, L. (1999). A third-generation wave model for coastal regions: 1. model description and validation. *Journal of Geophysical Research, Section Oceans*, 104((C4)):7649–7666.

Bowen, A., Flay, R., and Panofsky, H. (1983). Vertical coherence and phase delay between wind components in strong winds below 20 m. *Boundary-Layer Meteorology*, 26(4):313–324.

Chen, J., Hui, M. C., and Xu, Y. (2007). A comparative study of stationary and non-stationary wind models using field measurements. *Boundary-layer meteorology*, 122(1):105–121.

Chen, T., Zhang, Q., Wu, Y., Ji, C., Yang, J., and Liu, G. (2018). Development of a wave-current model through coupling of FVCOM and SWAN. *Ocean Engineering*, 164:443 – 454.

Cheng, Z., Gao, Z., and Moan, T. (2018a). Wave load effect analysis of a floating bridge in a fjord considering inhomogeneous wave conditions. *Engineering Structures*, 163:197–214.

Cheng, Z., Svangstu, E., Gao, Z., and Moan, T. (2018b). Field measurements of inhomogeneous wave conditions in Bjørnafjorden;. *Journal of Waterway, Port, Coastal, and Ocean Engineering*.

Cheynet, E. (2016). Wind-induced vibrations of a suspension bridge: A case study in full-scale.

Cheynet, E., Jakobsen, J. B., and Obhrai, C. (2017a). Spectral characteristics of surface-layer turbulence in the north sea. *Energy Procedia*, 137:414–427.

Cheynet, E., Jakobsen, J. B., and Snæbjörnsson, J. (2016a). Buffeting response of a suspension bridge in complex terrain. *Engineering Structures*, 128:474–487.

Cheynet, E., Jakobsen, J. B., Snæbjörnsson, J., Mann, J., Courtney, M., Lea, G., and Svardal, B. (2017b). Measurements of surface-layer turbulence in a wide norwegian fjord using synchronized long-range doppler wind lidars. *Remote Sensing*, 9(10):977.

Cheynet, E., Jakobsen, J. B., Snæbjörnsson, J., Mikkelsen, T., Sjöholm, M., Mann, J., Hansen, P., Angelou, N., and Svardal, B. (2016b). Application of short-range dual-doppler lidars to evaluate the coherence of turbulence. *Experiments in Fluids*, 57(12):184.

Cheynet, E., Jakobsen, J. B., Svardal, B., Reuder, J., and Kumer, V. (2016c). Wind coherence measurement by a single pulsed doppler wind lidar. *Energy Procedia*, 94:462–477.

Davenport, A. G. (1961). The spectrum of horizontal gustiness near the ground in high winds. *Quarterly Journal of the Royal Meteorological Society*, 87(372):194–211.

Ødegaard, V., , and Nordeng, T. E. (2009). The benefit of going to higher resolution. Technical Report MET-report-15-2009, Norwegian Meteorological Institute.

Eidnes, G., Stefanakos, C., Knutsen, Ø., and Vold, S. (2014). Bridge across Bjørnafjorden. metocean conditions. Technical report, SINTEF.

Eidsvik, K. and Utnes, T. (1997). Flow separation and hydraulic transitions over hills modelled by the reynolds equations. *Journal of wind engineering and industrial aerodynamics*, 67:403–413.

Fonseca, R. B., Gonçalves, M., and Guedes Soares, C. (2017). Comparing the performance of spectral wave models for coastal areas. *Journal of Coastal Research*, pages 331–346.

Furevik, B., Aarnes, O., and Christakos, K. (2018). Simulation and observations of wave conditions in norwegian fjords. In *KPN LFCS WORKSHOP*.

Gonçalves, M., Rusu, E., and Guedes Soares, C. (2015). Evaluation of two spectral wave models in coastal areas. *Journal of Coastal Research*, pages 326–339.

Harris, R. (1990). Some further thoughts on the spectrum of gustiness in strong winds. *Journal of Wind Engineering and Industrial Aerodynamics*, 33(3):461–477.

Harstveit, K. and Ágústsson, H. (2017). E39, brukrysninger hordaland, ospøya - koherensanalyse. Technical report, Kjeller Vindteknikk.

Harstveit, K., Bredesen, R. E., and Agustsson, H. (2016). Bjørnafjorden, hordaland, kartlegging av vindforhold. Technical report, Kjeller Vindteknikk.

Holmes, J. D. (2015). *Wind loading of structures*. CRC press.

Holthuijsen, L. H. (2007). *Waves in Oceanic and Coastal Waters*. Cambridge University Press.

Hoque, M. A., Perrie, W., and Solomon, S. M. (2017). Evaluation of two spectral wave models for wave hindcasting in the Mackenzie Delta. *Applied Ocean Research*, 62:169 – 180.

Johansen, I. L. (2016). Technology qualification of extreme fjord crossings. In *ASME 2016 35th International Conference on Ocean, Offshore and Arctic Engineering*, pages V003T02A070–V003T02A070. American Society of Mechanical Engineers.

Jonkman, B. J. (2009). Turbsim user's guide: Version 1.50. Technical report, National Renewable Energy Lab.(NREL), Golden, CO (United States).

Kaimal, J. C., Wyngaard, J., Izumi, Y., and Coté, O. (1972). Spectral characteristics of surface-layer turbulence. *Quarterly Journal of the Royal Meteorological Society*, 98(417):563–589.

Komen, G. J., Cavaleri, L., Donelan, M., Hasselmann, K., Hasselmann, S., and Janssen, P. A. E. M. (1994). *Dynamics and Modelling of Ocean Waves*. Cambridge University Press, Cambridge, UK.

Koziel, A. (2017). Assessing wave conditions in a Norwegian fjord. Master's thesis, University of Stavanger, Norway.

Krenk, S. (1996). Wind field coherence and dynamic wind forces. In *IUTAM symposium on advances in nonlinear stochastic mechanics*, pages 269–278. Springer.

Kristensen, L. and Jensen, N. (1979). Lateral coherence in isotropic turbulence and in the natural wind. *Boundary-Layer Meteorology*, 17(3):353–373.

Lie, H., Fu, S., Fylling, I., Fredriksen, A., Bonnemaire, B., and Kjersem, G. (2016). Numerical modelling of floating and submerged bridges subjected to wave, current and wind. In *35th International Conference on Ocean, Offshore and Arctic Engineering, OMAE'2016*, Busan, South Korea.

Lombardo, F. T., Smith, D. A., Schroeder, J. L., and Mehta, K. C. (2014). Thunderstorm characteristics of importance to wind engineering. *Journal of Wind Engineering and Industrial Aerodynamics*, 125:121–132.

Lothe, A. (2016). E39 Bjørnafjord crossing, design wave data, assignment no: 514672, doc. no. 1, ver. 1. Technical report, Norconsult.

Lothe, A. and Brørs, B. (2010). Mulighetsstudie for kryssing av Sognefjorden Opedal - Lavik. Estimat på bølger og strøm. Technical report, SINTEF.

Madsen, P. A., Murray, R., and Sørensen, O. R. (1991). A new form of the boussinesq equations with improved linear dispersion characteristics. *Coastal Engineering*, 15(4):371–388.

Mann, J. (1998). Wind field simulation. *Probabilistic engineering mechanics*, 13(4):269–282.

Massey, T. C., Anderson, M. E., Smith, J. M., Gomez, J., and Jones, R. (2011). STWAVE: Steady-state spectral wave model user's manual for stwave, version 6.0. Technical report, U.S. Army Corps of Engineers, Engineer Research and Development Center, Coastal and Hydraulics Laboratory.

Midtbø, K. H., Bremnes, J. B., Homleid, M., and Ødegaard, V. (2008). Verification of wind forecasts for the airports hammerfest, honningsvåg, sandnessjøen, Ørsta, værnes, sandane and narvik. Technical Report MET-report-02-2008, Norwegian Meteorological Institute.

Morfiadakis, E., Glinou, G., and Koulouvari, M. (1996). The suitability of the von karman spectrum for the structure of turbulence in a complex terrain wind farm. *Journal of wind engineering and industrial aerodynamics*, 62(2-3):237–257.

Nwogu, O. (1993). Alternative form of Boussinesq equations for nearshore wave propagation. *Journal of Waterway, Port, Coastal, and Ocean Engineering*, 119(6):618–638.

Ochi, M., Shin, V., et al. (1988). Wind turbulent spectra for design consideration of offshore structures. In *Offshore Technology Conference*. Offshore Technology Conference.

Reisner, J. M. and Smolarkiewicz, P. K. (1994). Thermally forced low froude number flow past three-dimensional obstacles. *Journal of the atmospheric sciences*, 51(1):117–133.

Reistad, M., Breivik, Ø., Haakenstad, H., Aarnes, O. J., Furevik, B. R., and Bidlot, J.-R. (2011). A high-resolution hindcast of wind and waves for the north sea, the norwegian sea, and the barents sea. *Journal of Geophysical Research: Oceans*, 116(C5).

Richardson, L. F. (1922). *Weather prediction by numerical methods*. Cambridge: Cambridge University Press.

Ropelewski, C. F., Tennekes, H., and Panofsky, H. (1973). Horizontal coherence of wind fluctuations. *Boundary-Layer Meteorology*, 5(3):353–363.

Rusu, E., Gonçalves, M., and Guedes Soares, C. (2011). Evaluation of the wave transformation in an open bay with two spectral models. *Ocean Engineering*, 38(16):1763–1781.

Saranyasoontorn, K., Manuel, L., and Veers, P. S. (2004). A comparison of standard coherence models for inflow turbulence with estimates from field measurements. *Journal of Solar Energy Engineering*, 126(4):1069–1082.

Shchepetkin, A. F. and McWilliams, J. C. (2005). The regional oceanic modeling system (ROMS): A split-explicit, free-surface, topography-following-coordinate oceanic model. *Ocean Modelling*, 9(4):347–404.

Simiu, E. and Scanlan, R. H. (1996). Wind effects on structures: fundamentals and applications to design.

Slagstad, D. and McClimans, T. A. (2005). Modeling the ecosystem dynamics of the Barents sea including the marginal ice zone: I. Physical and chemical oceanography. *Journal of Marine Systems*, 58(1):1–18.

Smith, J. M. (2006). Modeling nearshore waves for hurricane Katrina. In *Ninth International Workshop on Wave Hindcasting and Forecasting*, Victoria Canada.

Solari, G. (1987). Turbulence modeling for gust loading. *Journal of Structural Engineering*, 113(7):1550–1569.

Solari, G. and Piccardo, G. (2001). Probabilistic 3-d turbulence modeling for gust buffeting of structures. *Probabilistic Engineering Mechanics*, 16(1):73–86.

Sørensen, O., Kofoed-Hansen, H., Rugbjerg, M., and Sørensen, L. (2004). A third generation spectral wave model using an unstructured finite volume technique. In *Proceedings of the 29th International Conference of Coastal Engineering*, pages 894–906, Lisbon, Portugal.

Stefanakos, C., Knutsen, Ø., Eidnes, G., and McClimans, T. (2015). Bridge across Bjørnafjorden. simulation of waves, currents and hydrography. Technical report, SINTEF.

Strauss, D., Mirferendesk, H., and Tomlinson, R. (2007). Comparison of two wave models for Gold Coast, Australia. *Journal of Coastal Research*, Special Issue 50:312–316.

Strømmen, E. (2010). *Theory of bridge aerodynamics*. Springer Science & Business Media.

Svangstu, E. (2016). Technical note, wave conditions for phase 3. Technical report, Norwegian Public Road Administration.

SVV (2017). Design basis metocean. Technical Report SBJ-01-C3-SVV-01-BA-001 RevC, National Public Roads Administration.

The WAMDI Group (1988). The WAM model-A third generation ocean wave prediction model. *Journal of Physical Oceanography*, 18(12):1775–1810.

Thresher, R., Holley, W., Smith, C., Jafarey, N., and Lin, S. (1981). Modeling the response of wind turbines to atmospheric turbulence. Technical report, Oregon State Univ., Corvallis (USA). Dept. of Mechanical Engineering.

Tolman, H. (1991). A third-generation model for wind waves on slowly varying, unsteady, and inhomogeneous depths and currents. *Journal of Physical Oceanography*, 21:782–797.

Toriumi, R., Katsuchi, H., and Furuya, N. (2000). A study on spatial correlation of natural wind. *Journal of Wind Engineering and Industrial Aerodynamics*, 87(2-3):203–216.

Van der Hoven, I. (1957). Power spectrum of horizontal wind speed in the frequency range from 0.0007 to 900 cycles per hour. *Journal of meteorology*, 14(2):160–164.

Vegvesen, S. (2015). Håndbok n400 bruprosjektering.

Von Karman, T. (1948). Progress in the statistical theory of turbulence. *Proceedings of the National Academy of Sciences of the United States of America*, 34(11):530.

Wang, H., Li, A., Niu, J., Zong, Z., and Li, J. (2013). Long-term monitoring of wind characteristics at sutong bridge site. *Journal of Wind Engineering and Industrial Aerodynamics*, 115:39–47.

Wang, J., Cheynet, E., Jakobsen, J. B., and Snæbjörnsson, J. (2017a). Time-domain analysis of wind-induced response of a suspension bridge in comparison with the full-scale measurements. In *ASME 2017 36th International Conference on Ocean, Offshore and Arctic Engineering*, pages V03BT02A032–V03BT02A032. American Society of Mechanical Engineers.

Wang, J., Li, L., Jakobsen, J., and Haver, S. (2018a). Metocean conditions in a Norwegian fjord. In *37th International Conference on Ocean, Offshore and Arctic Engineering, OMAE'2018*, Madrid, Spain.

Wang, J., Li, L., Jakobsen, J. B., and Haver, S. K. (2018b). Metocean conditions in a norwegian fjord. In *ASME 2018 37th International Conference on Ocean, Offshore and Arctic Engineering*. American Society of Mechanical Engineers.

Wang, W., Bihs, H., Kamath, A., and Arntsen, Ø. (2017b). Large scale CFD modelling of wave propagation in Sulafjord for the E39 project. In *9th National Conference on Computational Mechanics, MekIT 2017*, Trondheim, Norway.

Warner, J. C., Armstrong, B., He, R., and Zambon, J. B. (2010). Development of a Coupled Ocean–Atmosphere–Wave–Sediment Transport (COAWST) modeling system. *Ocean Modelling*, 35(3):230 – 244.

Technology for a better society

www.sintef.no